Antenna-Coupled mm-Wave Electro-Optic Modulators
and
Linearized Electro-Optic Modulators

Thesis by

Finbar T. Sheehy

In Partial Fulfillment of the Requirements
for the Degree of
Doctor of Philosophy

California Institute of Technology
Pasadena, California
1993
(Submitted May 6, 1993)

To the Memory of

John Alphonsus Sheehy (1934 – 1990)

my father,
who believed in me
though I did not,
supported me when I did,
and laughed with me
at our "failures."

Ave, atque Vale.

Acknowledgements

I thank Professor William B. Bridges, my thesis advisor. During my time at Caltech he has provided me with much useful advice and many fascinating insights, in areas by no means limited to the work presented here. I have come to realize how fortunate I am to have had an advisor with a genuine interest in my personal as well as professional development, a man available to me as teacher, mentor and friend. I very much appreciate his guidance and support.

I would also like to thank James H. Schaffner, at Hughes Research Laboratories, who collaborated with us on this project, building devices, providing technical information, and taking part in many invaluable technical discussions. I thank Professor David B. Rutledge for his technical advice, which has been often sought and freely given.

I have enjoyed working with everyone involved in Professor Bridges' group. Reynold Johnson provided friendly and practical technical help, always with a sense of humor and fun. Laura Rodriguez and Connie Rodriguez, Dr. Bridges' secretaries, have cheerfully navigated the clerical complexities of Caltech for me. Professor Bridges' other research students, Yongfang Zhang, Lee Burrows, and Arthur Sheiman, provided much support, encouragement and ideas. Arthur deserves special mention for his expertise in keeping my car on the road for so long.

I am grateful to AT&T, for the Bell Laboratories Ph.D. Fellowship program, which provided me with most of my financial support during this project, and to Schlumberger, whose fellowship program supported me for my first year at Caltech. Financial support of the project was provided primarily by Rome Laboratories, who also provided my summer support. In addition, the project received support from the Caltech President's Fund.

I have enjoyed the support of many friends, inside and outside Caltech, who have encouraged me during my time here. That my experience of graduate school has been so much fun is largely due to them, and I thank them all, especially Barry Ryan.

Finally, to all the members of my family, I owe a debt of gratitude. To my parents, Kay and Alfie, whose love, support and encouragement were things I always took for granted. To my grandmother, Rita Powell, who devoted so much time and love to me as I grew up. To my sister, Catherine, and brother, Hugh, who are my friends. I am proud to share this achievement with them.

Abstract

We have demonstrated antenna-coupled electro-optic modulators at frequencies up to 98 GHz. The antenna-coupled design allows the modulator to overcome the velocity-mismatch problem which limits the maximum operating frequency of more conventional designs. Several modulators have been demonstrated, including a prototype narrowband phase modulator (optical wavelength 0.633 μm) at 10 GHz, a narrowband phase modulator (0.633 μm) at 60 GHz, a broadband Mach-Zehnder modulator operated as a phase modulator at 60 GHz, and a broadband Mach-Zehnder amplitude modulator at 94 GHz (optical wavelength 1.3 μm). The performance of the prototype modulator at 10 GHz is not quite as good as that of conventional modulators at this frequency, but is comparable. The performance of the mm-wave modulators cannot be directly compared to conventional modulators, as none exist at these frequencies. However, we have established that the relative performance of the mm-wave modulators is consistent with a simple scaling law.

Linearized $\Delta\beta$ modulators have been demonstrated recently by other workers. These linearized modulators consist of conventional $\Delta\beta$ coupler-modulators cascaded with additional couplers. We have considered the general case of cascade-linearized $\Delta\beta$ modulators, and have shown that it is possible to provide up to four degrees of freedom which can be used to modify the modulator transfer function. We have shown that these degrees of freedom can be identified and separated for design purposes, and have shown how to implement a given design.

Contents

Page

1. Introduction

2. The Physics of Electro-Optic Modulators

7. Design and Implementation of Linearized $\Delta\beta$ Electro-Optic Modulators - A Theoretical Study

8. Comparison of mm-Wave Electro-Optic Transmission Systems

9. Broadband Substrate-Wave-Coupled Electro-Optic Modulator

Appendix A

Radiation Pattern of the Interfacial Antenna

Appendix B

Optimum Power Distribution in Traveling-Wave Electro-Optic Modulators

Appendix C

Fabrication of the Electro-Optic Modulators

Appendix D

Frequency Content of Mixed Phase-Amplitude Modulation

Appendix E

Analysis of the Linearized Modulators

1. Introduction

1.1 The Field

Optical technology is becoming increasingly important for communications and measurement. Researchers have developed a wide variety of devices which allow light to interact with electrical signals (or other optical signals). These include lasers, switches and switching networks, amplifiers, detectors, and various types of modulators. There are many applications, including analog links [1], digital links [2 - 5], and other more specialized applications such as optical wavefront measurements [6].

1.2 The Thesis

This thesis reports on two developments of optical modulators using the electro-optic effect in $LiNbO_3$. In electro-optic materials the refractive index (or, equivalently, the dielectric constant) is a function of the electric field strength, and this effect can be used in a variety of ways to produce optical modulators. The developments reported are high-frequency modulators, with demonstrated operation at up to 98 GHz in the laboratory, and theoretical studies of highly linear modulators and a variety of possible electro-optic links.

1.3 Brief Review of the Technology

While a considerable number of materials display useful electro-optic behavior [7], $LiNbO_3$ has been used extensively in modulators. It has a large electro-optic coefficient, low optical and electrical losses, and it is easy to fabricate optical waveguides in the material [8]. $LiNbO_3$ is used in large amounts to make surface-acoustic-wave devices, and the economics of scale make the *material relatively cheap. Titanium in-diffusion is the most common method of* producing the optical guides, and was demonstrated in 1974 (Schmidt and Kaminow [9]). Other optical waveguide production techniques include proton exchange (Jackel et al. [10]) and ion implantation (Destefanis et al. [11]). The major competitors to $LiNbO_3$ in modulators are semiconductors such as GaAs, InP, and InGaAsP [12], which have support from the huge existing efforts in semiconductor development, and possible compatibility with solid-state laser fabrication methods. To date, however, the optical losses are higher in these modulators than in $LiNbO_3$ and it is not yet clear which material will be favored in the future, or whether other preferred materials will emerge.

Electro-optic modulators, of course, involve interaction between electrical and optical signals. In order to achieve efficient interaction, it is necessary to confine both the optical and electrical signals. The optical signal is confined by the optical waveguide just below the surface of the electro-optic material. In a single-waveguide phase modulator (Figure 1.1) the electrical signal is impressed upon the optical signal by positioning electrodes so as to produce the desired electric field across the optical waveguide, modifying the propagation conditions there. Alternatively, two coupled optical waveguides may be used in a directional-coupler configuration. By controlling the refractive index of the waveguides, it is possible to change the coupling so that an arbitrary amount of the input power is transfered to the coupled port [13]. This electrically-controlled optical switch may be an amplitude modulator if only one of the output ports is used. A more common type of amplitude modulator is the Mach-Zehnder interferometric modulator [14]. Here a 3 dB coupler splits the optical signal into two paths, one of which is effectively a quarter optical

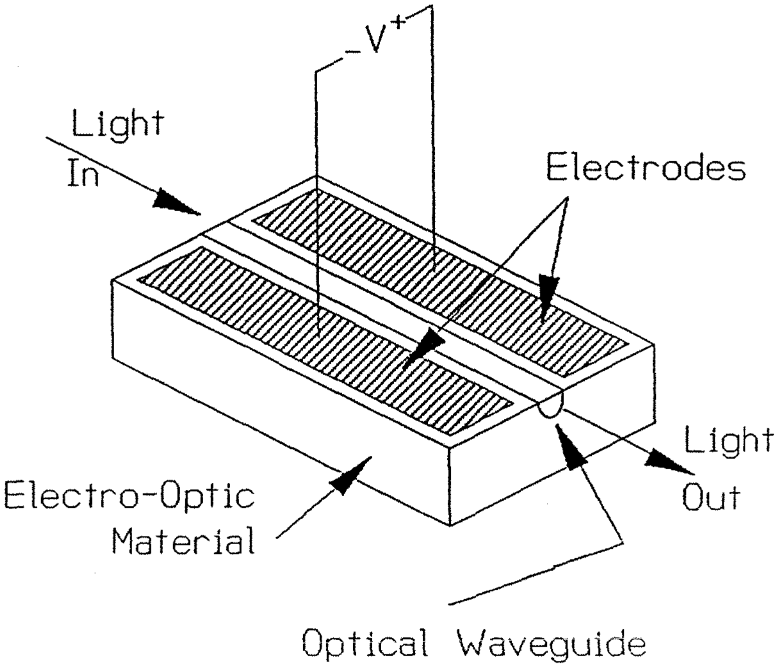

Figure 1.1 Electro-Optic Phase Modulator

Optical waveguide confines optical beam to high-electric-field region between the modulating electrodes.

wavelength longer than the other. The light is phase-modulated in opposite senses in the two paths, then recombined in a second 3 dB coupler (Figure 1.2). This produces an amplitude-modulated output by virtue of the controlled constructive or destructive interference between the outputs of the two paths.

$LiNbO_3$ does have some undesirable attributes. It is anisotropic, but more important, it is dispersive. Its refractive index to microwaves is much higher than to light. The result is that microwave and millimeter-wave signals travel too slowly along the interaction electrode structure to interact properly with the light in the optical waveguide below. This gives rise to a sensitivity-bandwidth tradeoff of 6dB/octave for baseband modulators. In addition, attenuation of the modulating signal in the electrode structure becomes a problem as the signal frequency rises. Finally, it becomes very difficult to make connections to the modulator in the electrical domain at high frequencies, because lead and connector parasitics may be severe [15].

1.4 The Antenna-Coupled Modulator Project

In the antenna-coupled modulator project we examined a new approach to the design of electro-optic modulators on $LiNbO_3$. This approach produces a sensitive modulator which can operate at high (mm-wave) modulation frequencies. The resulting modulator cannot have a baseband response, but rather will show bandpass behavior. For this reason it is not suitable for digital transmission, which requires baseband response, but is suitable for analog applications where bandpass behavior is acceptable. Bandpass modulators for high frequencies have been proposed and demonstrated by others [16,17], but in those cases the modulating signal is coupled to the modulator by coaxial cable,

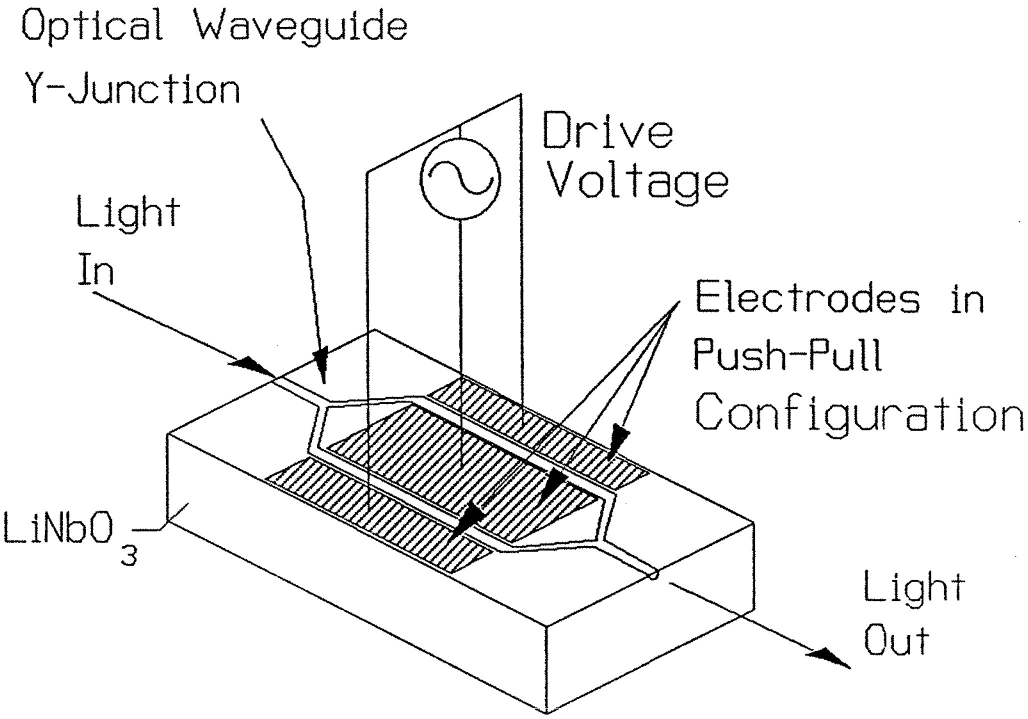

Figure 1.2 Mach-Zehnder Amplitude Modulator

Optical beam is split into two paths. The paths are phase-modulated with opposite polarities and recombined. Optical Y-junctions are much more gradual than this drawing would suggest.

and is subject to large parasitic effects and high conductor losses as before. In our design, the cable parasitics are removed, and conductor losses are less significant.

1.5 The Highly-Linear Modulator Study

In the highly-linear modulator study we looked at ways of modifying a $\Delta\beta$ directional-coupler modulator to improve the linearity of its transfer function (I_{out}/V_{in}). This type of modulator has a sinc^2 transfer function in its unmodified form, and is operated at the inflection-point of the transfer function, where the second-harmonic distortion is zero. Third-order intermodulation is appreciable, however. We have found that it should be possible to construct a modulator which, when properly biased, has virtually no products of second-, third- or fourth- (and possibly fifth- or sixth-) order in its output.

References

[1] C.H. Cox III, G.E. Betts, and L.M. Johnson, "An Analytic and Experimental Comparison of Direct and External Modulation in Analog Fiber-Optic Links," IEEE Trans. Microwave Theory & Tech., Vol. 38, No. 5, May 1990

[2] S.K. Korotky, et al., "4-Gbit/s Transmission Experiment over 117 km of Optical Fiber Using a Ti:LiNbO$_3$ External Modulator," IEEE J. Lightwave Tech., Vol. 3, No. 5, October 1985

[3] S.K. Korotky, A.H. Gnauck, B.L. Kasper, J.C. Campbell, J.J. Veselka, J.R.

Talman, and A.R. McCormick, "8-Gbit/s Transmission Experiment over 68 km of Optical Fiber using a Ti:LiNbO_3 External Modulator," IEEE J. Lightwave Tech., Vol. 5, No. 10, October 1987

[4] E.J. Murphy, J. Ocenasek, C.R. Sandahl, R.J. Lisco, and Y.C. Chen, "Simultaneous Single-Fiber Transmission of Video and Bidirectional Voice/Data Using LiNbO_3 Guided Wave Devices," IEEE J. Lightwave Tech., Vol. 6, No. 6, June 1988

[5] T. Okiyama, H. Nishimoto, I. Yokota, and T. Touge, "Evaluation of 4-Gb/s Optical Fiber Transmission Distance with Direct and External Modulation," IEEE J. Lightwave Tech.,Vol. 6, No. 11, November 1988

[6] R.H. Rediker, T.A. Lind, and B.E. Burke, "Optical Wavefront Measurement and/or Modification using Integrated Optics," IEEE J. Lightwave Tech.,Vol. 6, No. 6, June 1988

[7] I.P. Kaminow, "Optical Waveguide Modulators," IEEE Trans. Microwave Theory & Tech., Vol. 23, No. 1, January 1975

[8] L. Thylen, "Integrated Optics in LiNbO_3: Recent Developments in Devices for Telecommunications," IEEE J. Lightwave Tech., Vol. 6, No. 6, June 1988

[9] R.V. Schmidt and I.P. Kaminow, "Metal Diffused Optical Waveguides in LiNbO_3," Appl. Phys. Lett., Vol. 25, pp. 458-460, 1974

[10] J.L. Jackel, C.E. Rice, and J.J. Veselka, "Proton Exchange for High-Index Waveguides in $LiNbO_3$," Appl. Phys. Lett., Vol. 41, p. 607, 1982

[11] G.L. Destefanis, J.P. Gaillard, E.L. Ligeon, S. Valette, B.W. Farmery, P.D. Townsend, and A. Perez, "The Formation of Waveguides and Modulators in $LiNbO_3$ by Ion Implantation," Jour. Appl. Phys., Vol. 50, p. 7898, 1978

[12] G. Mak, C. Rolland, K.E. Fox and C. Blaauw, "High-Speed Bulk InGaAs-InP Electroabsorbtion Modulators with Bandwidth in Excess of 20 GHz," IEEE Photonics Tech. Lett., Vol. 2, No. 10, October 1990

[13] T.Tamir, Ed., Integrated Optics, Berlin, W. Germany: Springer Verlag, 1985

[14] C.M. Gee, G.D. Thurmond and H.W. Yen, "17-GHz Bandwidth Electro-Optic Modulator," Appl. Phys. Lett., Vol. 43, No. 11, December 1983

[15] ____ , "Traveling-Wave Electrooptic Modulator," Appl. Optics, Vol. 22, No. 13, July 1983

[16] D. Erasme, D.A. Humphries, A.G. Roddie, and M.G.F. Wilson, "Design and Performance of a Phase-Reversal Traveling Wave Modulator," J. Lightwave Tech., Vol. 6, No. 6, pp. 933-936, June 1988

[17] J.H. Schaffner and R.R. Hayes, "Ka-Band Integrated Optic Modulators with Periodic Intermittent Interaction Electrodes," presented at the Integrated

Photonics Research Topical Meeting, Monterey, CA, April 9-12, 1991

2. The Physics of Electro-Optic Modulators

2.1 The Electro-Optic Effect

In general, dielectric materials may not be isotropic. In this case it is not possible to write

$$D = \epsilon\, E, \tag{1}$$

but instead one could write

$$\begin{bmatrix} D_x \\ D_y \\ D_z \end{bmatrix} = \begin{bmatrix} \epsilon_{xx} & \epsilon_{xy} & \epsilon_{xz} \\ \epsilon_{yx} & \epsilon_{yy} & \epsilon_{yz} \\ \epsilon_{zx} & \epsilon_{zy} & \epsilon_{zz} \end{bmatrix} \begin{bmatrix} E_x \\ E_y \\ E_z \end{bmatrix}. \tag{2}$$

This defines a permittivity tensor for the material, given an arbitrary choice of axes {x,y,z}. If the material is reciprocal, then $\epsilon_{xy} = \epsilon_{yx}$ etc., so the tensor contains 6 elements, not 9. It is also possible to choose the axes so that the off-axis elements are zero, and this is the usual way to define the axes. Then

$$\begin{bmatrix} D_x \\ D_y \\ D_z \end{bmatrix} = \begin{bmatrix} \epsilon_{xx} & 0 & 0 \\ 0 & \epsilon_{yy} & 0 \\ 0 & 0 & \epsilon_{zz} \end{bmatrix} \begin{bmatrix} E_x \\ E_y \\ E_z \end{bmatrix}. \tag{3}$$

The electro-optic effect is defined with two additional tensors, which are

$$\Delta\frac{1}{\epsilon} \quad = \quad \begin{bmatrix} \Delta\frac{1}{\epsilon_{xx}} \\ \Delta\frac{1}{\epsilon_{yy}} \\ \Delta\frac{1}{\epsilon_{zz}} \\ \Delta\frac{1}{\epsilon_{yz}} \\ \Delta\frac{1}{\epsilon_{xz}} \\ \Delta\frac{1}{\epsilon_{xy}} \end{bmatrix}, \tag{4}$$

and

$$\mathbf{r} \quad = \quad \begin{bmatrix} r_{11} & r_{12} & r_{13} \\ r_{21} & r_{22} & r_{23} \\ r_{31} & r_{32} & r_{33} \\ r_{41} & r_{42} & r_{43} \\ r_{51} & r_{52} & r_{53} \\ r_{61} & r_{62} & r_{63} \end{bmatrix}. \tag{5}$$

The elements of **r** are defined by

$$\Delta\frac{1}{\epsilon} = \mathbf{r}\,\mathbf{E}\,, \tag{6}$$

where now **E** is the 3 x 1 electric field vector. For Lithium Niobate the **r** tensor takes the following form:

$$\mathbf{r} = \begin{bmatrix} r_{11} & 0 & r_{13} \\ -r_{11} & 0 & r_{13} \\ 0 & 0 & r_{33} \\ 0 & r_{42} & 0 \\ r_{42} & 0 & 0 \\ 0 & -r_{11} & 0 \end{bmatrix} . \qquad (7)$$

Notice that $\Delta \frac{1}{\epsilon_{zz}}$ depends only on the electric field component E_z. If the optical signal propagating in the material is linearly polarized in the z-direction, and if an externally-applied electric field is applied in the z-direction, then the externally-applied field will influence the propagation velocity of the optical signal, without any cross-coupling to another polarization. What this means is that the only part of the above equations which remains relevant is:

$$\frac{1}{\epsilon_{zz}} \Big|_{E = E_z} = \frac{1}{\epsilon_{zz}} \Big|_{E = 0} + r_{33} E_z . \qquad (8)$$

For optical modulators the refractive index is more significant than the dielectric constant, so by taking square roots and approximating with the first term of the binomial expansion,

$$n_z (E_z) = n_{opt} \left(1 - \frac{r_{33}}{2} n_{opt}^2 E_z \right) . \qquad (9)$$

2.2 Electro-Optic Phase Modulation

Now consider how long it takes an optical signal to propagate a distance L through a material of refractive index n_{opt}. The time required is

$$t_o = \frac{L\ n_{opt}}{c}\ . \qquad (10)$$

If the material refractive index changes due to the presence of an externally-applied electric field, the propagation time changes. This change in propagation time is

$$\Delta\ t\ =\ \frac{L}{2\ c}\ r_{33}\ {n_{opt}}^3\ E_z\ . \qquad (11)$$

This, of course, represents a phase-shift in the optical signal. The phase-shift is related to the applied electric field by:

$$\Delta\phi\ =\ \frac{\omega\ L}{2\ c}\ r_{33}\ {n_{opt}}^3\ E_z\ , \qquad (12)$$

where ω is the optical angular frequency ($= 2\ \pi\ f_{opt}$).

2.3 Lumped-Element Electro-Optic Phase Modulators

If the electro-optic modulator is short compared to the wavelength at the highest modulation frequency, then it may be considered as a lumped-element component. In order to confine the optical signal, an optical waveguide is fabricated in the $LiNbO_3$. This may be done by Ti-diffusion, proton exchange, or ion implantation. Electrodes are then fabricated so that when a voltage is applied to the electrodes the appropriate z-oriented modulating electric field will be applied to the optical waveguide region (Figure 2.1). These electrodes have capacitance, which is made greater by the large dielectric constant of $LiNbO_3$. Since the signal source has non-zero output impedance, often 50Ω, the capacitance results in an R-C rolloff at high frequency, limiting the bandwidth.

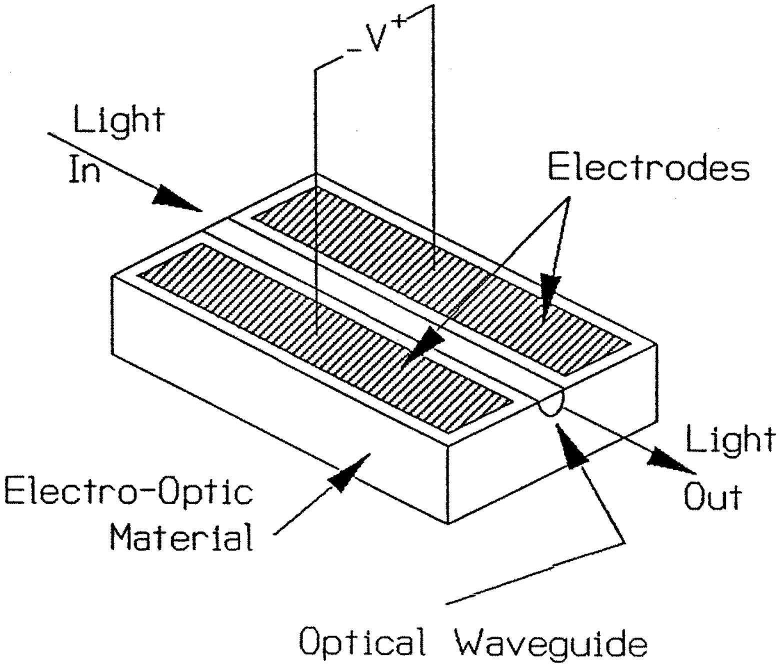

Figure 2.1 Lumped-Element Phase Modulator

Nevertheless, modulators of this sort can have very useful bandwidths [1]. Ultimately, however, the traveling-wave modulator has inherently greater bandwidth.

2.4 The Traveling-Wave Phase Modulator

If the electrodes are viewed as a transmission-line with distributed inductance as well as distributed capacitance, they can be designed to have the same impedance as the signal source (assuming a real signal-source impedance - usually 50Ω). The electrodes are driven at one end by the signal source, and are terminated at the other end by a matched load (Figure 2.2). Now the signal source is presented with a matched load at all frequencies, and there is no R-C rolloff at high frequency. The penalty for this bandwidth increase is a loss of modulator sensitivity. The low-frequency response of the modulator is halved because of the matched load, as compared to the capacitor-type electrodes. In order to get the same phase-modulation as a capacitor-type electrode at low frequency, the traveling-wave type must be driven by a signal-generator capable of supplying 4 times as much power - i.e., the matched termination costs 6 dB in responsivity.

Although the traveling-wave modulator does not suffer from the R-C bandwidth limitation, it does suffer from limitations of its own. These occur at a much higher frequency, where the electrodes are no longer short compared to a wavelength. As we have already noted, $LiNbO_3$ has a much higher refractive index for microwave/millimeter waves than for optical signals, which means that the microwave/millimeter wave modulating signal is propagating more slowly than the optical signal This causes the two to begin to get "out of step,"

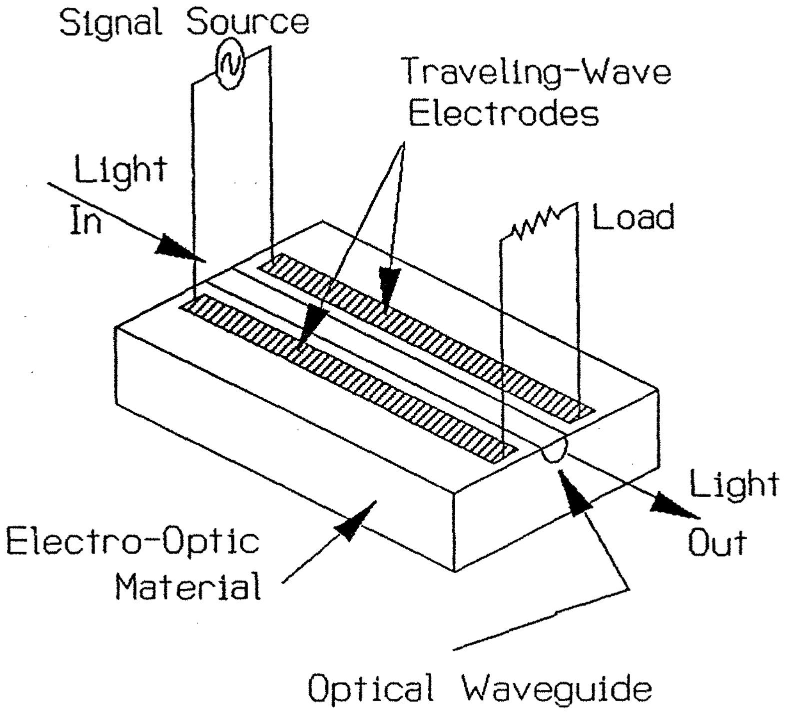

Figure 2.2 Traveling-Wave Phase Modulator

and this imposes bandwidth limitations.

2.5 Frequency Response of the Traveling-Wave Phase Modulator

In expression (12) above, the phase deviation depends on the electric field strength E_z. However, this expression was derived for a DC electric field, and the applied field is now an RF field. Solving the rather ugly nonlinear wave equation that results from having the two signals propagate in the lithium niobate (which is dispersive between them) is not a practical idea. It is much easier to find the "average electric field strength experienced by an optical wavefront as it propagates through the modulator." To do this, assume that the wave's velocity is not affected by the modulation (which is true to a very good approximation).

Suppose that the effective refractive index experienced by the modulating signal as it propagates along the electrode structure is n_m. Then the modulation signal propagates at c/n_m while the optical signal propagates at c/n_{opt}. The time taken for each to travel a distance x is:

$$t_o = \frac{x\, n_{opt}}{c}\,, \tag{13}$$

$$t_m = \frac{x\, n_m}{c}\,, \tag{14}$$

$$t_m - t_o = \frac{x}{c}\,(n_m - n_{opt})\,. \tag{15}$$

This time-difference (15) represents an electrical phase θ, where

$$\theta = \frac{\omega_m \mathrm{x}}{\mathrm{c}} (\mathrm{n}_m - \mathrm{n}_{opt}) \, , \tag{16}$$

where ω_m is the modulating signal angular frequency ($= 2\,\pi\,\mathrm{f}_m$).

The largest mean value of the electric field "experienced" by any optical wavefront is now given by the integral

$$\mathrm{E} = \frac{\mathrm{E}_m}{\mathrm{L}} \int_{-L/2}^{L/2} \cos\!\left(\frac{\omega_m \mathrm{x}}{\mathrm{c}} (\mathrm{n}_m - \mathrm{n}_{opt})\right) \mathrm{dx} \tag{17}$$

$$= \frac{\mathrm{E}_m}{\mathrm{L}} \; \frac{2 \sin\!\left(\frac{\omega_m}{\mathrm{c}} (\mathrm{n}_m - \mathrm{n}_{opt}) \frac{\mathrm{L}}{2}\right)}{\frac{\omega_m}{\mathrm{c}} (\mathrm{n}_m - \mathrm{n}_{opt})} \tag{18}$$

$$= \mathrm{E}_m \,\mathrm{sinc}\left(\frac{\omega_m \mathrm{L}}{2\,\mathrm{c}} (\mathrm{n}_m - \mathrm{n}_{opt})\right) . \tag{19}$$

Substituting this for E_z in expression (12) gives the frequency response of a traveling-wave electro-optic phase modulator:

$$\Delta\phi = \frac{\omega\,\mathrm{L}}{2\,\mathrm{c}} \, \mathrm{r}_{33} \, \mathrm{n}_{opt}{}^3 \, \mathrm{E}_m \,\mathrm{sinc}\left(\frac{\omega_m \mathrm{L}}{2\,\mathrm{c}} (\mathrm{n}_m - \mathrm{n}_{opt})\right) . \tag{20}$$

The response is a sinc-function in frequency (ω_m), but the interaction length L appears in front of the sinc-function as well, and so the response is sinusoidal in L. If the two signals propagate along the structure at the same velocity ($\mathrm{n}_m = \mathrm{n}_{opt}$) then the sinc-function is always 1, the frequency-response is flat and the phase deviation increases linearly with L. In conventional $\mathrm{LiNbO_3}$ modulators, where the modulating signal propagates along electrodes on the surface of the

$LiNbO_3$, the modulating signal experiences an effective refractive index intermediate between that of air (n=1) and that of $LiNbO_3$ (n=5.3). The refractive index experienced by the modulating signal is 3.8 (= $\sqrt{(5.3^2+1^2)/2}$). The light propagates much faster than this in the optical waveguide, where n_{opt} = 2.2 .

2.6 The Mach-Zehnder Amplitude Modulator

Photodetectors are insensitive to phase modulation, but sensitive to amplitude modulation. In order to make use of the phase-modulators described above, one must convert the phase modulation to amplitude modulation. The most common way to do this is to use a Mach-Zehnder interferometer (MZI) - see Figure 2.3.

The MZI works as follows: the input optical beam is split equally between two single-mode waveguides. Each waveguide passes through a phase modulator, then the waveguides come together to recombine the beams. The output waveguide is also single-mode. In operation, the two phase modulators are driven with the same electrical signal, but with opposite polarities. Hence the phase is advanced in one modulator, and retarded in the other by the same amount. When the beams recombine, the output will be a maximum if there is no phase-difference between the paths, a minimum if there is a 180^0 phase-difference, and somewhere in between for other phase-differences. The combined-beam amplitude varies sinusoidally with phase-difference (Figure 2.4). Of course, the optical power does not simply disappear if it does not emerge in the output optical guide. Instead it goes into higher-order modes, which are not guided but scatter into the substrate. This is why the output guide must be

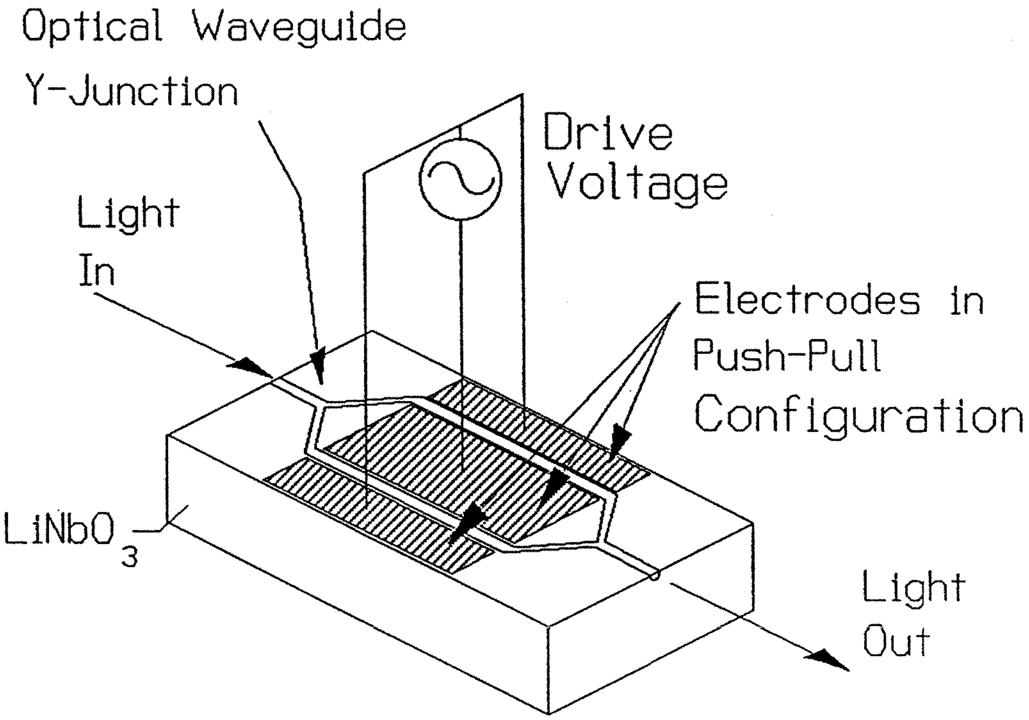

Figure 2.3 Mach-Zehnder Interferometer

(Electro-Optic Amplitude Modulator)

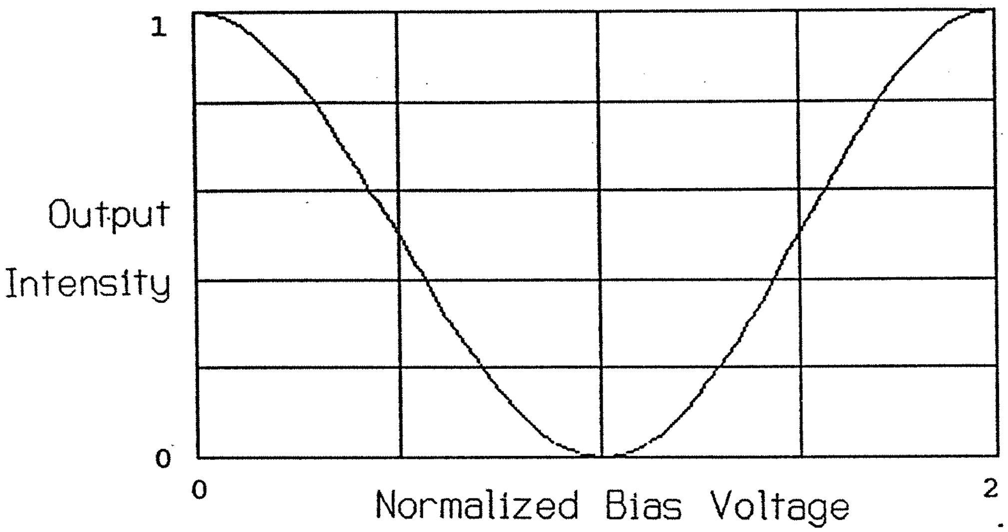

Figure 2.4 Transfer Function of the Mach-Zehnder

single-mode. If it is multimode, then much of the light which should have scattered into the substrate will be converted to other guided modes, and will appear at the output of the modulator. This will reduce the amplitude modulation of the output signal appreciably.

It is possible to drive the phase modulators with electrical signals of different amplitudes. The extreme example of this is to drive only one of the phase modulators, in an unbalanced MZI. This produces combined amplitude and phase modulation, which may be viewed as an amplitude modulator with frequency-chirp. This is not desirable in most cases; one of the potential advantages of external modulators is that they can be chirp-free. However, if the unbalance is small, the chirp is also small, and Korotky et al. [2] have claimed some advantages for communications if the chirp is tailored to the fiber characteristics.

The modulator converts phase modulation to amplitude modulation most linearly when driven with a small signal, with a "bias"-phase difference of 90^o. Because of the symmetry about this operating point, there is no second-harmonic generation due to the sinusoidal nonlinearity, but there is third-harmonic generation. For good linearity, the phase-deviation about the bias-point must always be kept small. On the other hand, for digital operation the phase-difference must be zero or 180^o to turn the modulator full on or full off.

While one might expect that a symmetrically-constructed modulator would have zero phase-difference between the two paths, it is not usually possible to guarantee that the fabrication process is so precise. In addition, $LiNbO_3$ is strongly pyroelectric and piezoelectric, so that small temperature gradients or strains in the crystal will produce electric fields which will alter the optical phases in the two paths via the electro-optic effect. A $LiNbO_3$ modulator must be biased to its operating point, and the bias will need to have active control to maintain the desired 90^o operating point, which will otherwise wander slowly. One way to do this, for example, is to monitor a pilot-tone, and adjust the bias until the second-harmonic of the tone is zero at the output. There is an additional bias problem, as there is a tendency for $LiNbO_3$ modulators to show some bias-drift even when the temperature and physical conditions are carefully controlled. This may be due to surface effects, and is being studied [3].

2.7 The $\Delta\beta$ Coupler Modulator

The $\Delta\beta$ modulator (Figure 2.5) operates on an entirely different principle from the phase-modulator-based Mach-Zehnder. It is an amplitude modulator which depends on coupled-mode theory. Small variations in the propagation velocities in two coupled optical waveguides can produce large variations in the amount of power coupled from one waveguide to the other. In the next few sections I will discuss the theory behind these modulators. Much of what I will present is discussed by Yariv [4], but I have collected and re-ordered the material found there and have changed the form of the results for the purpose of interpretation.

2.8 Theory of Coupled Modes

In this section I will present a formalism for describing coupling between modes. This begins with the Maxwell wave equation in the form

$$\nabla^2 \mathrm{E}(\mathbf{r},\mathrm{t}) = \mu\epsilon_o \frac{\partial^2 \mathrm{E}(\mathbf{r},\mathrm{t})}{\partial \mathrm{t}^2} + \mu \frac{\partial^2}{\partial \mathrm{t}^2} \mathbf{P}(\mathbf{r},\mathrm{t}) \ . \qquad (21)$$

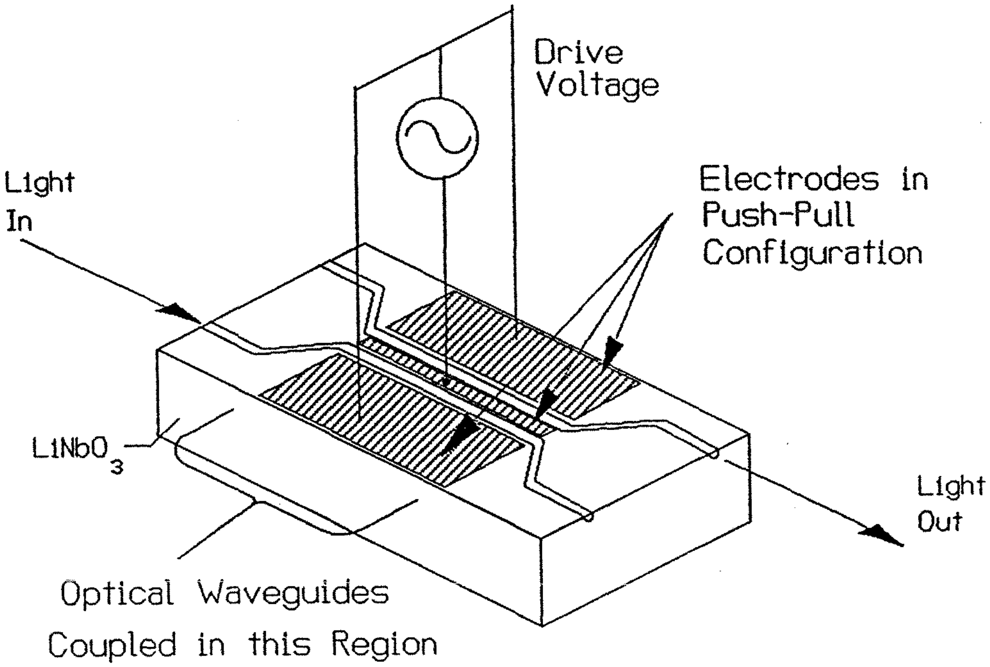

Figure 2.5 The Δβ Coupler-Modulator

The medium polarization $\mathbf{P}(\mathbf{r},t)$ can be written as

$$\mathbf{P}(\mathbf{r},t) = \mathbf{P}_o(\mathbf{r},t) + \mathbf{P}_{pert}(\mathbf{r},t) \,, \tag{22}$$

where

$$\mathbf{P}_o(\mathbf{r},t) = [\, \epsilon(\mathbf{r}) - \epsilon_o \,]\, \mathbf{E}(\mathbf{r},t) \tag{23}$$

is the polarization of an unperturbed waveguide whose dielectric constant is $\epsilon(\mathbf{r})$. The perturbation introduces coupling between modes. When we substitute (22) and (23) into (21) and write out only the y-component we obtain

$$\nabla^2 E_y - \mu\epsilon(\mathbf{r}) \frac{\partial^2 E_y}{\partial t^2} = \mu \frac{\partial^2}{\partial t^2} [\, P_{pert}(\mathbf{r},t) \,]_y \,. \tag{24}$$

Since we are dealing with a system which supports only confined modes, we can write the y-component of the mth such mode as $\mathcal{E}_y{}^{(m)}$, where

$$\left(\frac{\partial^2}{\partial x^2} - \beta_m{}^2 \right) \mathcal{E}_y{}^{(m)}(\mathbf{r}) + \omega^2\mu\epsilon(\mathbf{r})\, \mathcal{E}_y{}^{(m)}(\mathbf{r}) = 0 \,, \tag{25}$$

and we can write E_y as a superposition of such modes:

$$E_y(\mathbf{r},t) = \tfrac{1}{2} \sum_m A_m(z)\, \mathcal{E}_y{}^{(m)}(x)\, e^{j(\omega t - \beta_m z)} + \text{constant.} \tag{26}$$

Note that z is the direction of propagation and x is the transverse direction orthogonal to y.

Substitution of (26) into (24), using the condition (25) and the assumption of "slow" variation so that

$$\left|\frac{d^2A_m}{dz^2}\right| \ll \left|\frac{dA_m}{dz}\right| , \qquad (27)$$

we obtain

$$\sum_m -j\beta_m \frac{dA_m}{dz} \mathcal{E}_y^{(m)} e^{j(\omega t - \beta_m z)} + \text{const.} = \mu \frac{\partial^2}{\partial t^2} [\, P_{pert}(\mathbf{r},t) \,]_y \, . \qquad (28)$$

Now note that the modes $\mathcal{E}_y^{(m)}$ are orthogonal, which means that

$$\int_{-\infty}^{\infty} \mathcal{E}_y^{(s)} \mathcal{E}_y^{(m)} \, dx = \frac{2\,\omega\mu}{\beta_m} \delta_{s,m} \, . \qquad (29)$$

Using this fact, we take the product of (28) with $\mathcal{E}_y^{(s)}(x)$ and integrate from $-\infty$ to ∞, which gives the result

$$\frac{dA_s^{(-)}}{dz} e^{j(\omega t + \beta_s z)} - \frac{dA_s^{(+)}}{dz} e^{j(\omega t - \beta_s z)} - \text{constant}$$

$$= -\frac{j}{2\omega} \frac{\partial^2}{\partial t^2} \int_{-\infty}^{\infty} [P_{pert}(\mathbf{r},t)]_y \, \mathcal{E}_y^{(s)}(x) \, dx \, . \qquad (30)$$

$A_s^{(-)}$ is the coefficient of the wave traveling in the -z direction, and $A_s^{(+)}$ is the coefficient of the wave traveling in the +z direction.

2.9 Directional Coupling

We now have the framework of coupled-mode theory available so that we can consider directional coupling. Consider two dielectric waveguides whose refractive index distributions are given by $n_a(x)$ and $n_b(x)$. The transverse field distributions for each waveguide alone are $\mathcal{E}_y^{(a)}(x)$ and $\mathcal{E}_y^{(b)}(x)$, with propagation constants β_a and β_b. Let the complete coupled structure have index distribution $n_c(x)$, with propagation along the direction z. We can now approximate the field in the coupled structure as the weighted sum of the fields which would exist in either structure alone.

$$E_y = A(z)\ \mathcal{E}_y^{(a)}(x)\ e^{j(\omega t - \beta_a z)} + B(z)\ \mathcal{E}_y^{(b)}(x)\ e^{j(\omega t - \beta_b z)}. \qquad (31)$$

If the two waveguides are not coupled then A(z)=A(0) and B(z)=B(0) for all z. If the waveguides are coupled, then A and B will vary with z. Substituting (31) into (22) and (23), we have

$$P_{pert} = e^{j\omega t}\epsilon_o \left\{\mathcal{E}_y^{(a)} A(z)\left(n_c^2 - n_a^2\right) e^{-j\beta_a z} + \mathcal{E}_y^{(b)} B(z)\left(n_c^2 - n_b^2\right) e^{-j\beta_b z}\right\}. \qquad (32)$$

Now we can apply the result at the end of the section on coupled-mode theory, by substituting for P_{pert} in (30). This produces two coupled differential equations, which are:

$$\frac{dA}{dz} = -j\ \kappa_{ab}\ B\ e^{-j(\beta_b - \beta_a)z} - j\ M_a\ A\ ,$$

$$\frac{dB}{dz} = -j\ \kappa_{ba}\ A\ e^{j(\beta_b - \beta_a)z} - j\ M_b\ B\ , \qquad (33)$$

where

$$\kappa_{ab(ba)} = \frac{\omega\epsilon_o}{4}\int_{-\infty}^{\infty}\left(\mathrm{n}_c^{\,2}(\mathrm{x}) - \mathrm{n}_{b\,(a)}^{\,2}(\mathrm{x})\right)\mathcal{E}_y^{(a)}\,\mathcal{E}_y^{(b)}\,\mathrm{dx}\;, \qquad (34)$$

$$\mathrm{M}_{a(b)} = \frac{\omega\epsilon_o}{4}\int_{-\infty}^{\infty}\left(\mathrm{n}_c^{\,2}(\mathrm{x}) - \mathrm{n}_{a\,(b)}^{\,2}(\mathrm{x})\right)\left(\mathcal{E}_y^{(a(b))}\right)^2\,\mathrm{dx}\;. \qquad (35)$$

The terms M_a and M_b represent a small correction to the propagation constants β_a and β_b due to the presence of the second guide. If we now rewrite the total field as

$$\mathrm{E}_y = \mathrm{A}(\mathrm{z})\,\mathcal{E}_y^{(a)}(\mathrm{x})\,\mathrm{e}^{j(\omega t - \beta_{a,1} z)} + \mathrm{B}(\mathrm{z})\,\mathcal{E}_y^{(b)}(\mathrm{x})\,\mathrm{e}^{j(\omega t - \beta_{b,1} z)}\;, \qquad (36)$$

where

$$\beta_{a,1} = \beta_a + \mathrm{M}_a\;,$$
$$\beta_{b,1} = \beta_b + \mathrm{M}_b\;, \qquad (37)$$

instead of the earlier approximation (31), and assume symmetry between the guides, we get a slightly different set of coupled differential equations (c.f.(33)):

$$\frac{\mathrm{dA}}{\mathrm{dz}} = -\mathrm{j}\;\kappa\;\mathrm{B}\;\mathrm{e}^{-j2\delta z},$$

$$\frac{\mathrm{dB}}{\mathrm{dz}} = -\mathrm{j}\;\kappa\;\mathrm{A}\;\mathrm{e}^{j2\delta z}, \qquad (38)$$

where

$$2\delta = \beta_{b,1} - \beta_{a,1}\;. \qquad (39)$$

Note that conservation of energy requires that

$$\frac{\mathrm{d}}{\mathrm{dz}}\left(|\mathrm{A}|^2 + |\mathrm{B}|^2\right) = 0\;. \qquad (40)$$

The solution of (38) subject to boundary conditions B(0)=B_o, A(0)=0, is

$$A(z) = -j\, B_o\, e^{-j\delta z} \frac{\kappa}{\sqrt{\kappa^2 + \delta^2}} \sin\left(\sqrt{\kappa^2 + \delta^2}\ z\right),$$

$$B(z) = B_o\, e^{j\delta z} \left\{ \cos\left(\sqrt{\kappa^2 + \delta^2}\ z\right) - \frac{j\,\delta}{\sqrt{\kappa^2 + \delta^2}} \sin\left(\sqrt{\kappa^2 + \delta^2}\ z\right)\right\}. \quad (41)$$

I now define $A_1(z)$ and $B_1(z)$ according to:

$$A_1(z) = A(z)\, e^{j\delta z},$$

$$B_1(z) = B(z)\, e^{-j\delta z}. \quad (42)$$

Now, using (42) and (39) in (36) we find that:

$$\text{Coefficient of } \mathcal{E}_y^{(a)}(x)\, e^{j\omega t} = A_1(z)\, e^{-j\left(\frac{\beta_{a,1} + \beta_{b,1}}{2}\right)z},$$

$$\text{Coefficient of } \mathcal{E}_y^{(b)}(x)\, e^{j\omega t} = B_1(z)\, e^{-j\left(\frac{\beta_{a,1} + \beta_{b,1}}{2}\right)z}. \quad (43)$$

These two coefficients have a common phase term $e^{-j\left(\frac{\beta_{a,1} + \beta_{b,1}}{2}\right)z}$ which can be omitted from any analysis which does not require knowledge of the absolute phase-shift between the input and output of the coupler. Most analyses require only the relative phases of the outputs. This information is stored in A_1 and B_1. Hence the output optical fields may be represented by

$$A_1(z) = -j\, B_o \frac{\kappa}{\sqrt{\kappa^2+\delta^2}} \sin\left(\sqrt{\kappa^2+\delta^2}\ z\right),$$

$$B_1(z) = B_o \left\{ \cos\left(\sqrt{\kappa^2+\delta^2}\ z\right) - \frac{j\,\delta}{\sqrt{\kappa^2+\delta^2}} \sin\left(\sqrt{\kappa^2+\delta^2}\ z\right) \right\}. \quad (44)$$

In fact, these are the output fields if the input fields are

$$A(0) = 0\ ,$$

$$B(0) = B_o\, e^{j\left(\frac{\beta_{a,1}+\beta_{b,1}}{2}\right) z}. \qquad (45)$$

In terms of optical power, $P_o = B_o\, B_o^*$, and so the powers at the two output ports are given by:

$$P_a = P_o \frac{\kappa^2}{\kappa^2+\delta^2} \sin^2\left(\sqrt{\kappa^2+\delta^2}\ z\right),$$

$$P_b = P_o - P_a\ . \qquad (46)$$

2.10 The $\Delta\beta$ Coupler Modulator Analysis in Practice

These results are the theory behind a $\Delta\beta$ coupler modulator. In a practical modulator the material used to fabricate the optical waveguides is an electro-optic material such as $LiNbO_3$. When an electric field is applied to the material,

$$\delta(E) \sim \frac{\omega}{c}\, n^3\, r_{33}\, E\ , \qquad (47)$$

so we can substitute this in (46) to obtain

$$P_a = P_o \frac{1}{1+\left(\delta(E)/\kappa\right)^2} \sin^2\left(\sqrt{1+\left(\delta(E)/\kappa\right)^2}\ \kappa z\right),$$

$$P_b = P_o - P_a\,. \tag{48}$$

We now note that the power at port a depends on two dimensionless quantities, i.e., κz and δ/κ. In fact, κz is an angle, so we can define

$$\theta = \kappa z\ . \tag{49}$$

We also note that the electric field strength is related to the voltage applied to the electrodes of the device by an effective distance d, so that $V = dE$. Then

$$\delta(V)/\kappa \sim \frac{\omega}{c}\, n^3\, r_{33}\, \frac{V}{d}\,. \tag{50}$$

Define V_o according to:

$$\delta(V)/\kappa = \frac{V}{\sqrt{3}\, V_o}\,, \tag{51}$$

so that the modulator transfer function is now given by

$$P_a = P_o \frac{1}{1+\left(\frac{V}{\sqrt{3}\, V_o}\right)^2} \sin^2\left(\sqrt{1+\left(\frac{V}{\sqrt{3}\, V_o}\right)^2}\ \theta\right),$$

$$P_b = P_o - P_a \,. \tag{52}$$

The significance of scaling V_o in the way I have indicated is that the value of θ is usually chosen to be $\pi/2$ (or sometimes an integer multiple of $\pi/2$). In the case where $\theta = \pi/2$, then $P_a=1$ when $V=0$, and $P_a=0$ when $V=V_o$. In other words, V_o is the switching voltage of a modulator where $\kappa L=\pi/2$. Note that V_o does not itself depend on the length of the modulator, only on its cross-section.

The transfer-function of this modulator, as given in (52) and Figure 2.6, is not linear, of course. The modulator is usually operated at the point of inflection of the transfer function so that there are no second-order products. However, third and higher-order products will be present, giving rise to significant distortion which may be unacceptable in some analog applications. The distortion performance of this modulator is very similar to that of the Mach-Zehnder modulator, as pointed out by Halemane and Korotky [5], and the same bias-point stabilization considerations apply.

2.11 The Frequency Response of a Traveling-Wave $\Delta\beta$ Coupler Modulator

The traveling-wave analysis of the $\Delta\beta$ modulator is not simple, and will not be presented here. I will, however, discuss briefly how it can be done. As the optical and electrical signals propagate at different velocities the effect is that any given optical phasefront experiences a variation in δ with distance along the coupler. In the case of a simple phase modulator, the phase contribution of an infinitesimal length of the modulator can be computed as a function of position along the modulator. The total phase-shift is then found by integrating over

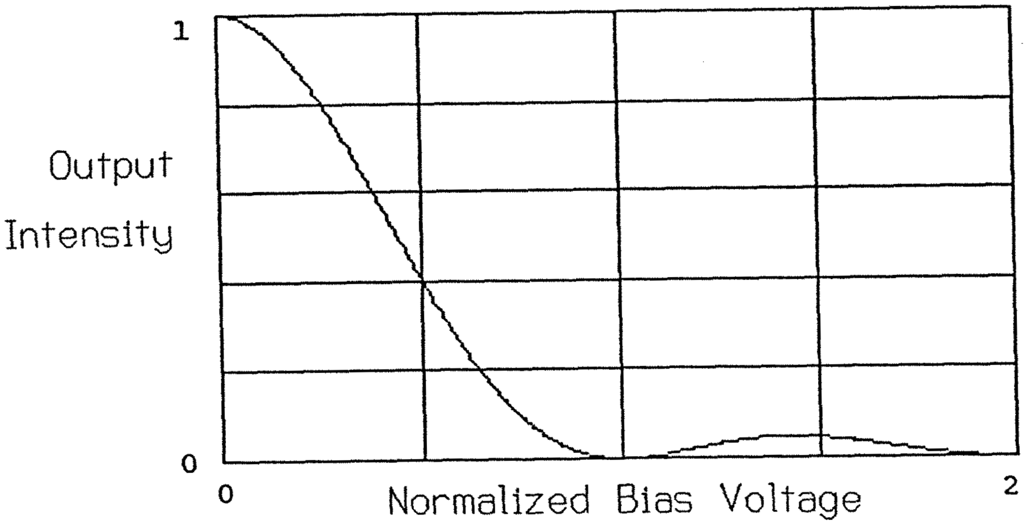

Figure 2.6 Transfer Function of
$\Delta\beta$ Modulator

the entire length of the modulator. Unfortunately this is not possible in the case of a directional coupler. This is because the coupler is a four-port device. The coupler is characterized by a transfer matrix of the form

$$\begin{bmatrix} \mathrm{a}_1 \\ \mathrm{b}_1 \end{bmatrix} = \begin{bmatrix} \mathrm{A} & \text{-}\mathrm{jB} \\ \text{-}\mathrm{jB} & \mathrm{A}^* \end{bmatrix} \begin{bmatrix} \mathrm{a}_o \\ \mathrm{b}_o \end{bmatrix}, \qquad (53)$$

where a_1 and b_1 are the field strengths at the two output ports, a_o and b_o are the field strengths at the input ports, and A and B are similar to S-parameters. The analogous process would be to divide the modulator into an infinite sequence of infinitesimally short lengths of coupler, each with the appropriate value of δ, and take the product of their transfer matrices - where the number of these matrices is infinite. This is not done. Korotky and Alferness [6] computed the time-domain impulse response of the modulator and took the Fourier transform of this. However, as Chung and Chang [7] point out, the modulator is nonlinear, so this is not a true small-signal frequency response. They obtained a perturbation solution by expanding a matrix differential equation - similar to (33) - as a power series and taking only the first term, producing a linear matrix differential equation which could be solved. Their result, for a directional coupler biased to the linear region, is

$$\Delta \mathrm{I}(\omega) = -\kappa_{ab} \{ [\mathrm{C}_1(\phi_c(\xi) - \tfrac{1}{2}\phi_c(\xi_m) - \tfrac{1}{2}\phi_c(\xi_p)) + \mathrm{C}_2(\phi_s(\xi_p) - \phi_s(\xi_m))]^2$$

$$+ [\mathrm{C}_1(-\phi_s(\xi) + \tfrac{1}{2}\phi_s(\xi_m) + \tfrac{1}{2}\phi_s(\xi_p)) + \mathrm{C}_2(\phi_c(\xi_p) - \phi_c(\xi_m))]^2 \}^{1/2}, \qquad (54)$$

where $\Delta I(\omega)$ is the small-signal change in intensity as a function of frequency for a given drive level, and

$$C_1 = \frac{\kappa\delta(3\delta - 1)}{2\,b^3}\sin(2\,b\,L) \qquad C_2 = \frac{-\kappa\,\delta^2}{b^4}\sin^2(b\,L) \tag{55}$$

$$\phi_s(\zeta) = \int_0^L e^{-\alpha z}\sin(\zeta\,z)\,dz \qquad \phi_c(\zeta) = \int_0^L e^{-\alpha z}\cos(\zeta\,z)\,dz \tag{56}$$

$$\xi_m = \xi - 2\,b \qquad \xi_p = \xi + 2\,b \tag{57}$$

$$\xi = \frac{\omega}{c}\,(n_m - n_{opt}) \qquad b = \sqrt{\delta^2 + \kappa^2}\,. \tag{58}$$

The normalized frequency response is then given by

$$M(\omega) = \frac{\Delta I(\omega)}{\Delta I(0)}\,. \tag{59}$$

According to this theory, for a $LiNbO_3$ modulator where there is no attenuation of the modulating signal ($\alpha = 0$), and where the effective microwave refractive index is 3.8, the bandwidth of a Mach-Zehnder interferometer modulator is given by

$$BW(GHz) = 82.9\;/\;L(mm)\;, \tag{60}$$

while that of a directional coupler modulator is given by

$$\mathrm{BW(GHz)} = 106\ /\ \mathrm{L(mm)}\ . \qquad (61)$$

So, in fact, the directional coupler has some 28% greater bandwidth. Remember, however, that this assumes no attenuation of the modulating signal in the electrodes, which is an unrealistic assumption. For a complete model of the frequency response, a model of the attenuation, including its frequency-dependence, would be required.

References

[1] M. Izutsu, Y. Yamane, and T. Sueta, "Broad-Band Traveling-Wave Modulator Using a $LiNbO_3$ Optical Waveguide," IEEE J. Quantum Elec., Vol. QE-13, No.4, pp. 287-290, April 1977

[2] S. Korotky, remarks made at Engineering Foundation Conference on High-Speed/High-Frequency Optoelectronics, held at Palm Coast, Florida, March 17-22, 1991 (no proceedings published)

[3] R.L. Jungerman, et al., "High-Speed Optical Modulator for Application in Instrumentation," J. Lightwave Tech., Vol. 8, No. 9, pp. 1363-1370, September 1990

[4] A. Yariv, Optical Electronics, 3rd Edition, Holt, Rinehart and Winston, New York 1985

[5] T.R. Halemane and S.K. Korotky, "Distortion Characteristics of Optical Directional Coupler Modulators," IEEE Trans. Microwave Theory & Techniques, Vol. 38, No. 5, pp. 669 - 673, May 1990

[6] S.K. Korotky and R.C. Alferness, "Time- and Frequency-Domain Response of Directional-Coupler Traveling-Wave Optical Modulators," IEEE J. Lightwave Tech., Vol. 1, No. 1, pp. 244-251, March 1983

[7] H. Chung and W.S.C. Chang, "Normal-Mode Small-Signal Analysis of Traveling-Wave Directional Couplers," IEEE J. Quantum Elec., **QE-28**, No. 5, pp. 1353 - 1359, May 1992

3. The Antenna-Coupled Modulator Concept

The analysis in Chapter 2 showed that the phase-velocity mismatch between the light and the modulating signal resulted in a sinc-function frequency response. The length of the modulator electrodes determined the cutoff frequency and the DC sensitivity, resulting in a constant sensitivity-bandwidth product. This means that if the modulator is to work at a high frequency it will have to be short and its sensitivity will be low, i.e., it will take a large driving voltage to produce a given phase-deviation.

It is possible to get a larger phase-deviation by positioning several sets of electrodes along the optical waveguide. The phase-velocity mismatch in each electrode segment produces some phase-error over its length, but with appropriate design the phase-error can be corrected at the start of the next electrode segment. This can be done in a number of ways [1-3]. Perhaps the best-known is the phase-reversal modulator (Figure 3.1). In this design the electrode segment length is such that the phase-error at the end is 90°. At this point the electrode structure reverses the electric field polarity, giving a -180° phase-change, so that the phase-error is now -90°. This procedure can be repeated any number of times, inserting a phase-reversal every time the phase error reaches 90°. There are also aperiodic phase-reversal designs [2]. An alternative approach, taken by Schaffner [3], uses a filter-type structure with delay stubs to produce the correct phase-velocity along the structure (Figure 3.2).

These methods achieve rephasing of the modulating signal at some center

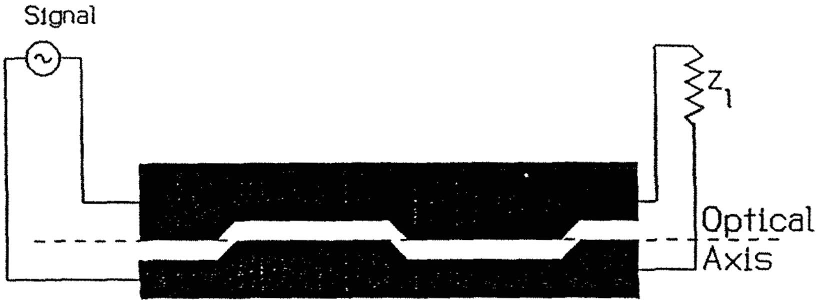

Figure 3.1 Phase-Reversal Modulator

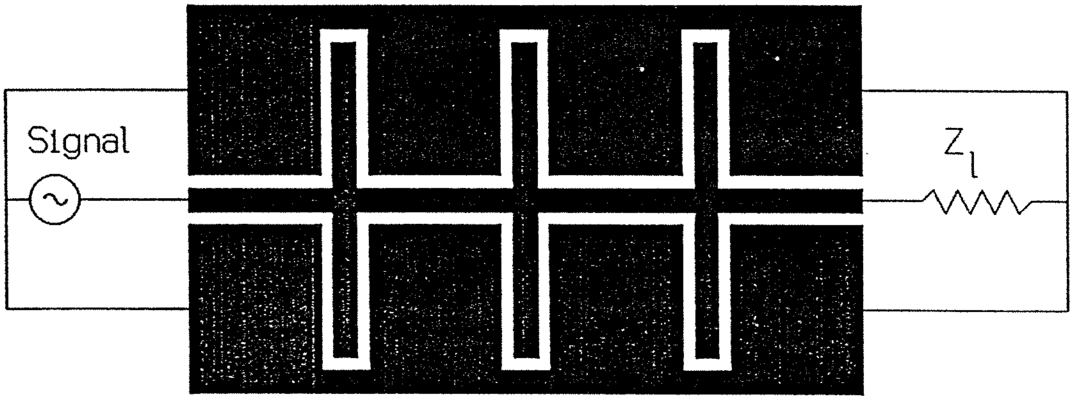

Figure 3.2 Schaffner Modulator

frequency, but are *essentially filter-structures. As more electrode segments are* added the sensitivity of the modulator at the center frequency increases, but the bandwidth decreases (Figure 3.3). Also, in practice it is not useful to keep adding more segments, because the modulating signal is attenuated at each step, so that eventually any additional electrode segments have little effect.

Bridges and Schaffner have suggested another idea, again involving a number of short modulator segments. They have proposed that the modulating signal be split into several parallel paths - actually delay-lines - whose lengths are chosen so that the signal arrives at the input to each modulator segment at exactly the right time to achieve proper phasing of the modulator segments. This method would achieve the rephasing by true time-delay, which has the advantage of working equally well at all frequencies - i.e., this is not a filter. A patent is pending on this idea.

The antenna-coupled modulator concept, originally proposed by Bridges (U.S. Patent No. 5, 076, 655), also achieves rephasing by true time-delay, so that it has no center-frequency and the bandwidth is independent of the number of segments. Each electrode segment is connected to its own surface antenna (Figure 3.4). The antennas are illuminated by the modulating signal at the angle which delays the modulating signal by the correct amount from antenna to antenna. This differs from the other approaches in a number of ways.

- Since the phase is corrected by a true time-delay method, rather than a filter structure, the bandwidth does not depend on the number of segments, but is equal to the bandwidth of a single antenna/electrode segment.

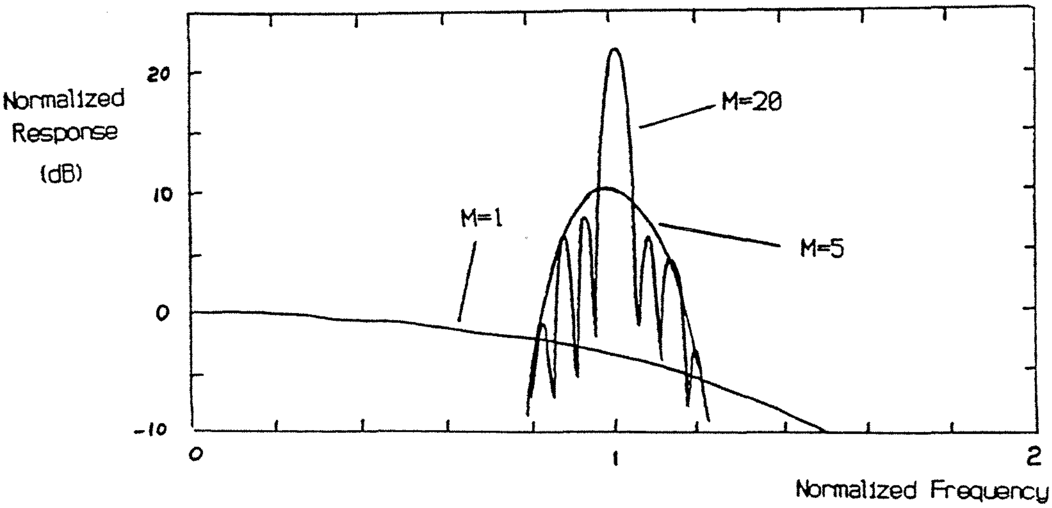

Figure 3.3 Frequency Response of M-Section Phase-Reversal Modulators

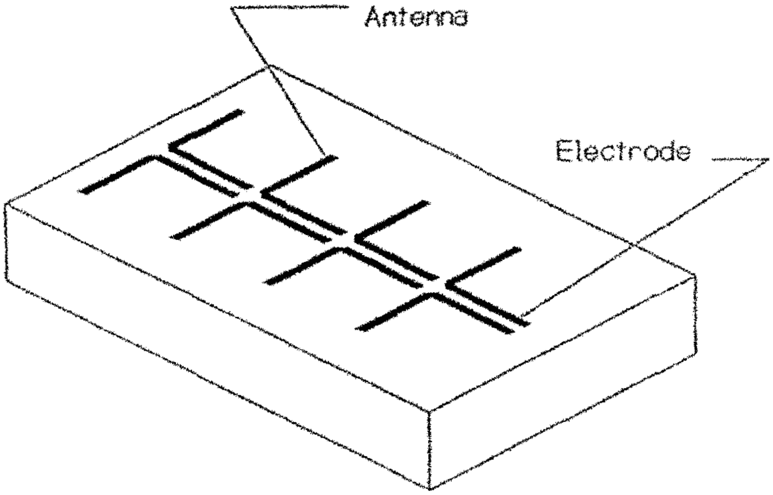

Figure 3.4
Antenna-Coupled
Modulator Concept

- The modulating signal drives the antennas in parallel, not in series, with the power divided equally between the antenna/electrode segments. Consequently the nth segment is driven with the same power as the 1st or any other segment - attenuation in the electrodes does not limit the number of segments which can be used.

- Millimeter-wave signals often originate in waveguide systems, which are compatible with the radiative feed required for this approach. Coax-to-electrode connections, with their associated parasitics, are not necessary.

- Although "manufacturing defects" are not usually considered, we note that a short-circuit in one antenna/electrode segment only degrades the performance by a small amount, while a similar defect in any other modulator renders the whole modulator entirely useless.

However, there are a few ways in which this approach is less attractive.

- The bandwidth of the modulator is determined by the bandwidth of the antenna/electrode elements. Antennas never have a DC response, and simple antennas have small bandwidths. Nevertheless, the bandwidth will be greater than for phase-reversal or other filter-type modulators, and useful bandwidths are feasible.

- Parallel distribution of power is less efficient than series distribution. While the sensitivity of a lossless phase-reversal-type modulator (with series feed from electrode to electrode) increases as the number of electrode elements n, the sensitivity of the antenna-coupled modulator increases as $\sqrt{n}$.

- As the number of antenna/electrode elements becomes large, the incident modulation signal must be kept very close to a plane wave. This amounts to a tradeoff between sensitivity and spatial bandwidth (in the sense that the incident signal may be represented as a spectrum of plane-waves, and this spectrum must be very limited).

- The dimensions of the modulation-signal feed can be quite large, especially when the number of antenna/electrode elements becomes large, requiring the feed to radiate the signal to the antennas with very small spatial bandwidth.

There remains the problem of finding the correct feed angle for the modulating signal. To understand how this works, consider Figure 3.5. If a signal is incident on the antenna array from the end, then its phase-velocity along the array is c/n, where n is the refractive index of the medium. If the signal is incident on the array from the side ("broadside"), then all the antennas are driven in the same phase, and the phase-velocity of the signal along the array is infinite. Thus any phase-velocity greater than c/n is possible by choosing the correct angle of incidence. In this case, the phase-velocity to match is the phase-velocity of light in the optical waveguide, i.e., $\frac{c}{2.2}$. This is less than c, so the method will not work if the modulating signal is propagating in free space. However, the index of $LiNbO_3$ is about 5.5 for the modulating signal, so the method will work if the modulating signal is incident on the antenna array from inside the $LiNbO_3$. This is fortunate, because antennas on a dielectric interface

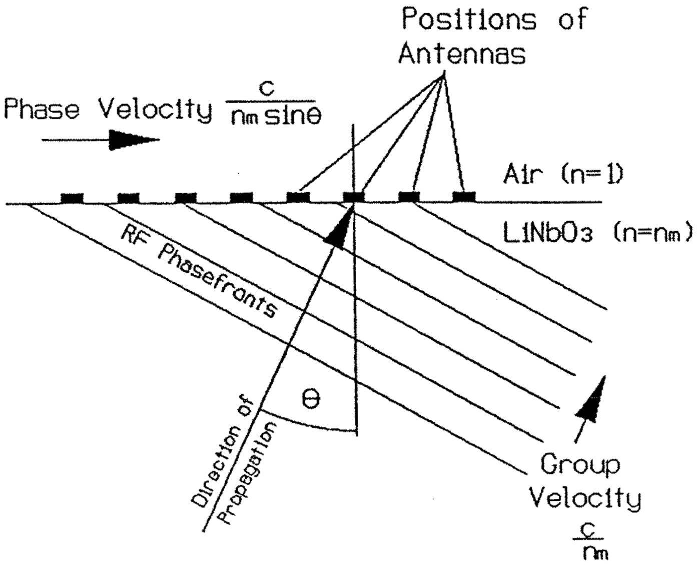

Set θ so that

$$\frac{c}{n_m \sin\theta} = \frac{c}{n_{opt}}$$

Figure 3.5 Angle-Matching of Phase Velocity

The antennas are located at the interface between $LiNbO_3$ and air. The positions of the antennas are shown in the diagram. The modulating signal is incident on the antenna array from inside the $LiNbO_3$ at the angle which provides a phase-velocity match as required.

are much more responsive to signals incident from inside the dielectric than to signals incident from the free-space side. The correct angle of incidence, θ, is at about 23° to normal ("broadside") incidence.

References

[1] R.C. Alferness, S.K. Korotky, and E.A. Marcatili, "Velocity-matching techniques for integrated optic traveling-wave switch/modulators," IEEE J. Quantum Electron., Vol. QE-20, pp. 301-309, 1984

[2] N. Zhu and Z. Wu, "Optimization of phase-reversal traveling-wave optical modulators," Microwave and Optical Tech. Lett., Vol.2, No.7, pp. 240-244, July 1989

[3] J.H. Schaffner, "Analysis of a millimeter-wave integrated electro-optic modulator with a periodic electrode," in Proc. SPIE OE-LASE Conf. 1217, paper 13, pp. 101-110, Los Angeles, CA, Jan 16-17 1990

4. Antenna-Coupled Modulators - Theoretical Considerations

4.1 Antennas on a Dielectric Half-Space

Since the electrodes of the antenna-coupled modulator are on the surface of the $LiNbO_3$ electro-optic material, the antennas will be on the interface between $LiNbO_3$ and air. The behavior of antennas is changed fundamentally by the presence of a dielectric interface like this. The simplest way to look at this effect is to assume that the $LiNbO_3$ is infinitely thick and examine the behavior of antennas on a dielectric half-space. A number of papers have been written on various aspects of this [1 - 5]. I will not go into a detailed examination of the physics involved here, but in Appendix A I derive antenna patterns for wire antennas on a dielectric half-space based on physical insight into the mechanism by which the antenna pattern is determined.

An antenna on a dielectric half-space cannot radiate along the interface, because no TEM wave can propagate along the dielectric interface - the phasefronts cannot match at the boundary. The radiation pattern therefore has a null along the interface. The other striking feature of such an antenna is that most of its power goes into the dielectric rather than into the air. Rutledge et al. [5] have given an explanation of this by considering the antenna as a receiving antenna. The antenna is at the interface between a low-impedance medium (the dielectric) and a high-impedance medium. Any power incident on the interface from the air-side will be reflected from a low-impedance medium. When this happens, the electric field-strength is small at the interface and the antenna response is small. When the power is incident from the dielectric side it is reflected from a high-impedance medium, so the electric field-strength is high at the interface and the antenna response is large.

Examples of the antenna-patterns of interfacial antennas are illustrated in Figures 4.1 - 4.3. Figure 4.1 shows the H-plane pattern of a dipole on a half-space of dielectric constant ϵ=4. (The antenna is normal to the plane of the diagram.) Note that there is very little coupling to the air-side of the interface. Almost all of the power is radiated into the dielectric. A notable feature of the antenna pattern is the cusp in the pattern on the dielectric side. This cusp occurs at the critical angle, i.e., at 30° in this case. Figure 4.2 is again a H-plane pattern of a dipole, but this time on a high-dielectric material, ϵ=36. This time there is virtually no coupling at all to the air-side of the interface. The cusp occurs at 9.6° now. If the length of the antenna is increased, and it is bent to form a V-antenna, quite different antenna patterns are possible. Figure 4.3 shows the H-plane pattern of a V-antenna on a dielectric half-space of ϵ=28. In this case the length of each arm of the V is one wavelength from end-to-end at the interface, where the effective refractive index is $\sqrt{(28 + 1)/2} = 3.8$. The V angle is 100°. This figure is taken from Appendix A, which goes into detail on the subject of wire antennas on dielectric half-spaces.

The fact that the antenna couples more efficiently into the dielectric is a fortuitous one. As we saw in Chapter 3, the modulating signal must be incident on the antenna array from inside the dielectric in order to achieve the necessary phase-velocity-match condition. This fits in nicely with the antenna's preference for radiation coming from inside the dielectric.

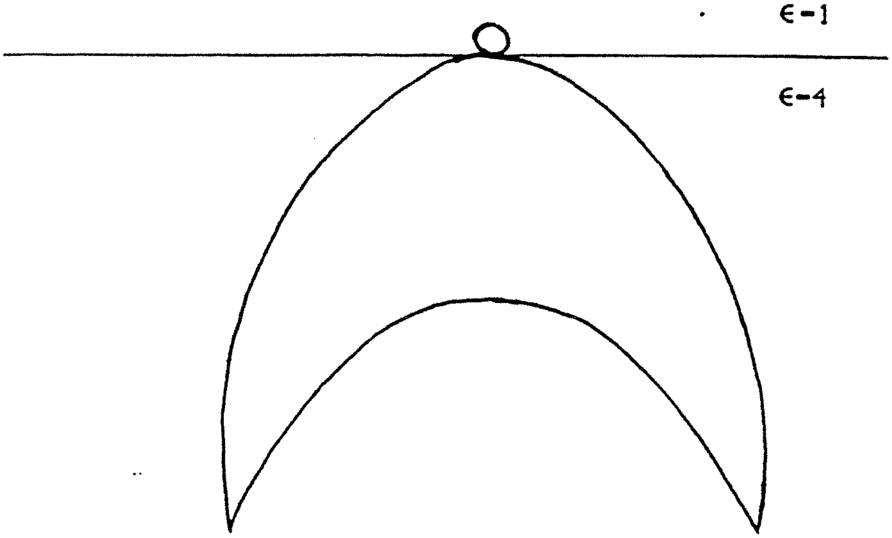

Figure 4.1 H-Plane Pattern of a Straight Dipole on Dielectric Half-Space $\epsilon=4$

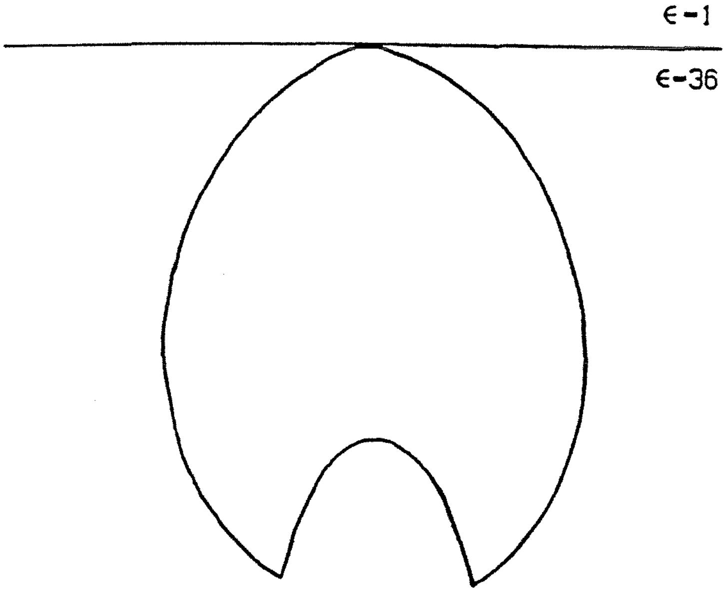

Figure 4.2 H-Plane Pattern of a Straight Dipole on Dielectric Half-Space ϵ=36

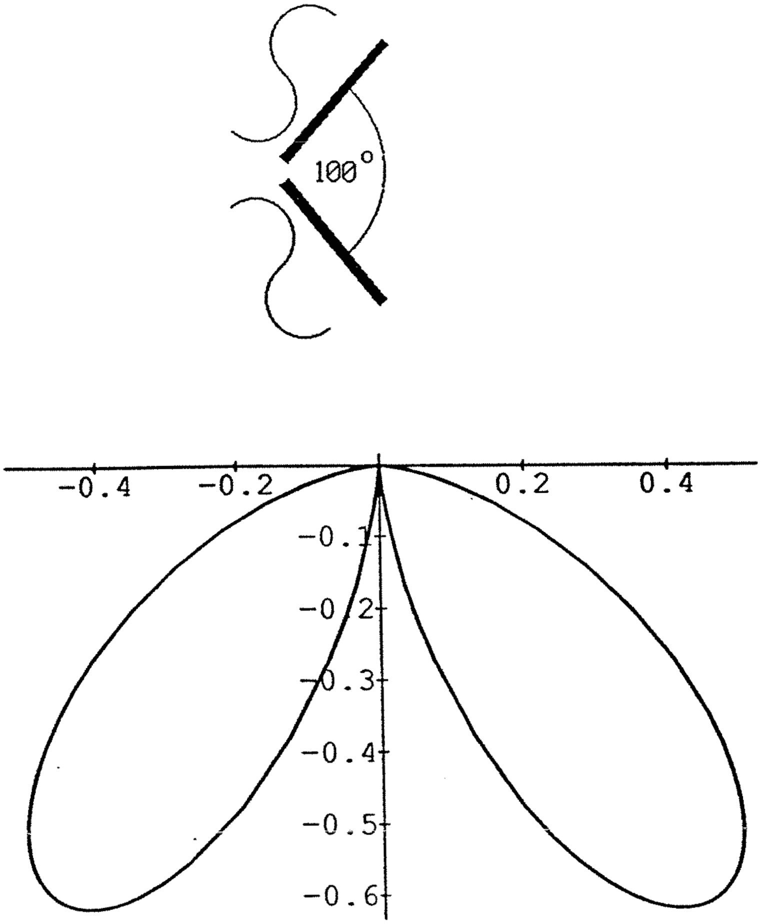

Figure 4.3 Antenna pattern of a V antenna on the surface of a dielectric, ϵ-28. Each arm of the V is one surface-wavelength long. The V angle is 100°. The pattern shown is in the dielectric, in the plane which bisects the V.

4.2 Modulation Efficiency as a Function of the Number of Antennas

The idea behind the antenna-coupled modulator concept is to allow the interaction length of the modulator to be made large so that the modulation efficiency (the total phase-shift per arm for a given input modulation signal power) can be increased. However, if there are two antennas then the power is split between them, so although the interaction length increases, the drive-power per unit length decreases. How does the net modulation efficiency behave?

The phase-shift depends on the modulating signal field strength and on the interaction length. The modulating signal power is proportional to the square of the field strength, which is to say that the field strength is proportional to the square root of the modulating signal power. When the number of antenna/electrode segments is increased from 1 to N, the total interaction length increases from L to NL, while the signal power per element decreases from P to P/N. This causes the field strength to decrease from E to $E/\sqrt{N}$. The net change in modulation efficiency is then from ηLE to $\eta(NL)(E/\sqrt{N}) = \sqrt{N}\,\eta LE$ (where η is the constant of proportionality which relates modulation efficiency to Length x Electric Field). So an N-element antenna-coupled modulator will be more efficient than a single-element modulator by $\sqrt{N}$.

It is instructive to compare this with a phase-reversal-type modulator. If there is no attenuation of the modulating signal, the electric field strength is independent of the number of phase-reversal sections because they are connected in series. Consequently the efficiency varies as N. However, there are two other matters to consider. First, there is attenuation of the modulating signal, so beyond some value of N there is very little further benefit to increasing the number of sections. Second, as I've noted previously, phase-reversal modulators are filters, and the bandwidth of the modulator decreases rapidly as N increases. The bandwidth of an antenna-coupled modulator is independent of N. The tradeoffs involved in choosing to drive modulator elements in series or parallel, and other power-split optimization considerations, are addressed in Appendix B.

4.3 Modulator Beamwidth and Phasefront Curvature

The antenna-coupled modulator concept requires that the modulating signal illuminate the antenna array in such a way that the antennas are driven in the proper phase. This is achieved by selecting the angle of incidence of the modulating signal. How precisely this angle must be maintained depends on the number of antennas in the modulator, and on their separation. Clearly if only one antenna is involved the angle of incidence does not matter. The analysis of the antenna-coupled modulator is essentially the analysis of a phased antenna array. The phasing, in this case, is determined by the light in the optical waveguide, whose propagation velocity from antenna to antenna determines the phasing of the array. Hence the modulator has an antenna pattern which is the product of the antenna pattern of a single antenna element with the array factor of the phased antenna array. (Note that the array factor may be modified to take account of the fact that the modulation signal feed will not, in general, illuminate the antennas with equal power. In fact, the modulator behaves like an apodized phased array.) As the array becomes longer, with more elements, its beamwidth narrows and its sidelobes become smaller. This means that although there is no electrical bandwidth penalty for increasing the interaction length (as there was in the case of the phase-reversal modulator) there is a spatial bandwidth penalty. The modulation signal must be radiated onto the antenna array with greater angular precision, and its phasefronts must be increasingly flat. Figure 4.4 shows an example of a modulator antenna pattern for a modulator with 18 antenna/electrode segments and an overall length of 3.6 λ_o, and Figure 4.5 shows how the modulation sensitivity of this modulator varies with phasefront curvature.

4.4 Feed Design

The importance of illuminating the antennas with the modulation signal in the correct way has been discussed above. The problem of doing this is the problem of feed design. Usually we would expect the mm-wave modulation signal to be coming from a rectangular metal waveguide. The feed should convert this guided wave so that it arrives at the antenna array with flat phasefronts at the correct angle of incidence. In addition, it should do so efficiently, losing as little power as possible to radiation, impedance mismatches, or overspill past the antenna array.

The lateral dimension of each antenna is generally of the order of the metal waveguide height (since the antenna is of the order of λ in length at the interface, i.e., $\lambda_o/3.8$, while typical waveguide height is $\lambda_o/6$) , but the length of the entire array may be an order of magnitude greater than the waveguide width. This means that the feed must somehow expand the power in one dimension but not the other. The most straightforward way to do this is to couple the power from the metal waveguide to a dielectric waveguide, then taper the width of the dielectric waveguide gradually until it matches the

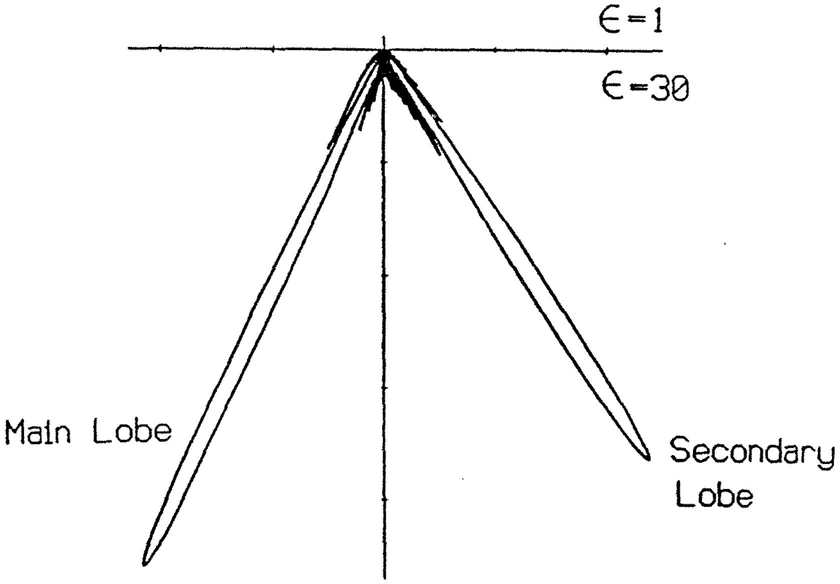

Figure 4.4 Antenna Pattern of a Modulator with 18 Dipole Antennas on $\epsilon=30$. Total Array Length = $3.6\,\lambda_0$

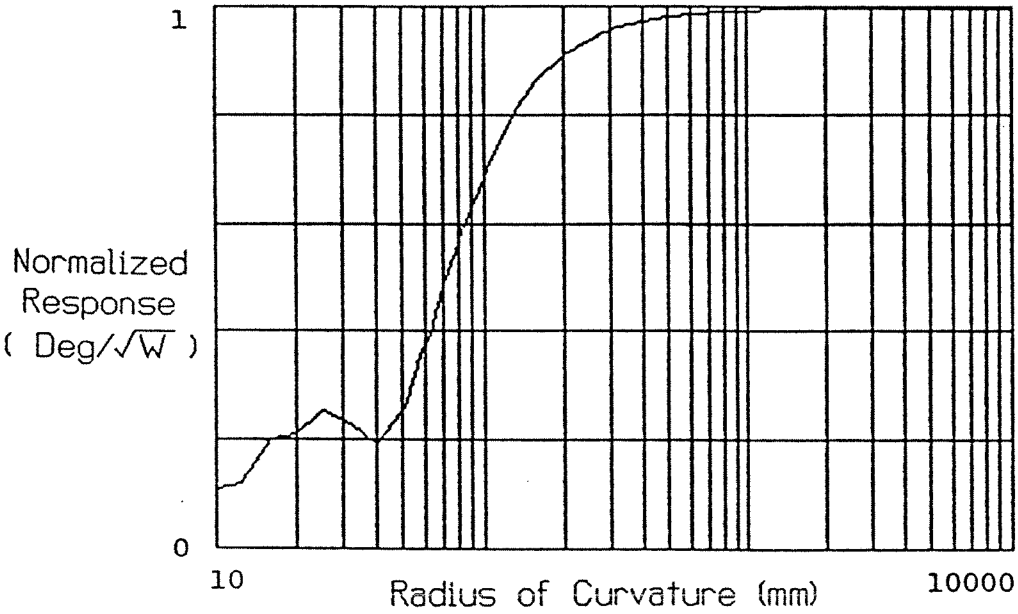

Figure 4.5 Modulator Response as a Function of Phasefront Curvature. This is the Modulator whose Antenna Pattern is shown in Figure 4.4.

length of the antenna array. This is not quite sufficient, however. The dielectric constant of the $LiNbO_3$ is very high, and it is difficult to couple power directly into a dielectric waveguide with high dielectric constant. It is easier to couple the power into a lower dielectric constant material, then couple from this low-dielectric-constant waveguide to a $LiNbO_3$ waveguide. This requires a matching network of some kind. The design of the feeds used in our experiments will be shown in the chapter on the experimental results, but is based on this concept.

References

[1] M. Kominami, D.M. Pozar, and D.H. Schaubert, "Dipole and Slot Elements and Arrays on Semi-Infinite Substrates," IEEE Trans. Ant. & Prop., Vol. AP-33, No. 6, pp. 600-607, June 1985

[2] N. Engheta and C.H. Papas, "Radiation Patterns of Interfacial Dipole Antennas," Radio Science, Vol. 17, pp. 1557-1566, November-December 1982

[3] G.S. Smith, "Directive Properties of Antennas for Transmission into a Material Half-Space," IEEE Trans. Ant. & Prop., Vol. AP-32, No. 3, pp. 232-246, March 1984

[4] R.C. Compton, R.C. McPhedran, Z. Popovic, G.M. Rebeiz, P.P. Tong, and D.B. Rutledge, "Bow-Tie Antennas on a Dielectric Half-Space: Theory and Experiment," IEEE J. Ant. & Prop., Vol 35, No.6, pp. 622- 631, June 1987

[5] D.B. Rutledge, D.P. Neikirk, and D.P. Kasilingam, "Integrated-Circuit

Antennas," Chapter 1, Infrared and Millimeter Waves, Vol. 10, Academic Press 1983

5. Antenna-Coupled Phase Modulator at 10 GHz

5.1 Design of the Prototype Modulator

In order to demonstrate the antenna-coupled modulator concept, we decided to build a prototype modulator at X-band. This prototype modulator should be as simple as possible, so that we would be able to understand its behavior. We chose to leave the modulator electrodes unterminated because of the practical difficulty of fabricating matched terminations for the electrodes at X-band, and because this problem would be even greater at mm-wave frequencies. We also decided to use simple dipole antennas, because we had a theoretical model for dipoles on a dielectric half-space. We chose to design a phase modulator rather than an intensity modulator. This is simpler to fabricate because it has no Y-junction in the optical waveguide (it consists of a single optical waveguide going from one end of the $LiNbO_3$ substrate to the other) and because it requires no DC bias to operate correctly (intensity modulators must be operated at the proper bias-point). Finally, we designed the optical waveguide for light at the HeNe wavelength of 0.633 μm, because experiments are easier when the beam is visible, and because HeNe lasers produce a nice, narrow, single-mode output, and because we happened to have some HeNe lasers available.

Thus, the baseline antenna/transmission line segment design we chose was a dipole antenna driving an unterminated (i.e., open-circuit) transmission line electrode above a single optical waveguide. The modulator has five of these antenna/transmission line segments on a 25 mm piece of X-cut $LiNbO_3$ (Figure 5.1). Each antenna is about a wavelength long (end to end), and the transmission line electrode is roughly a half wavelength long at 12 GHz. The

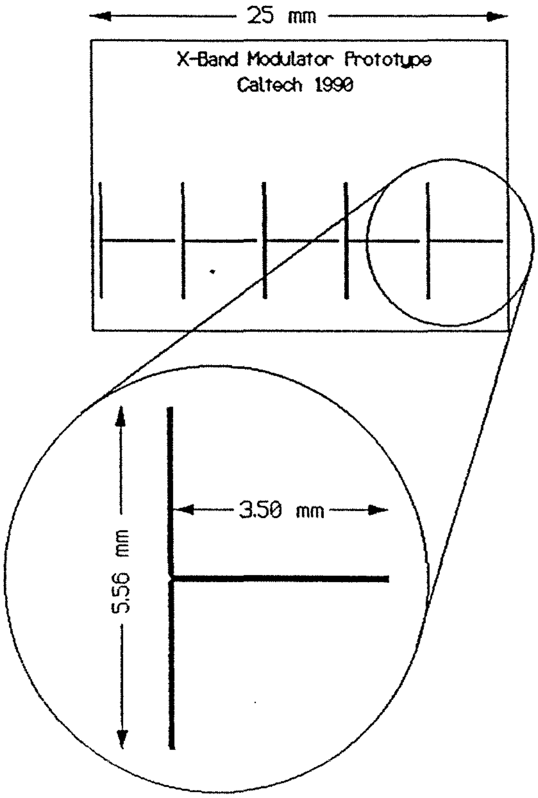

Figure 5.1 The 10 GHz Prototype Modulator

The inter-electrode gap cannot be resolved at this scale.

lengths were optimized using the theoretical model of the modulator. We had intended to optimize the modulator for 10 GHz, but it turned out that we were using a slightly wrong effective refractive index value in the model (4.6 instead of 3.8). When the correct index is used, the design turns out to be optimized nearer to 12 GHz.

5.2 Theoretical Model of the Modulator

The idea behind keeping the prototype modulator simple was to allow us to model it and show that its behavior could be accounted for. Thus, we needed to develop a theoretical model of the modulator. We were interested in the modulator's frequency response, its absolute sensitivity, and its spatial frequency-response (i.e., its sensitivity to being illuminated by the RF at the wrong angle of incidence).

We begin by looking at the transmission line electrode and the interaction between the modulating signal on the transmission line and the optical signal in the waveguide beneath. For a conventional traveling-wave modulator the modulation coefficient δ is a function of the transmission line length L, the optical refractive index n, the effective transmission line index n_m, and the modulation frequency $f_m \left(= \frac{\omega_m}{2\pi}\right)$. The relationship between these can be written:

$$\delta \, \alpha \, L \, \mathrm{Sinc} \left\{ \frac{\omega_m}{2\,c} (n - n_m) \, L \right\} . \tag{1}$$

However, in this design the transmission line has an open-circuit termination. The modulating signal will reflect from this open circuit and return toward the antenna. If the antenna is not well-matched to the transmission line there will be multiple reflections. Nevertheless, the various waves on the line may be summed to give one resultant wave propagating down the line to reflect (once) at the end. Then

$$\delta \;\alpha\; \mathrm{L} \;[\; \mathrm{Sinc} \left\{ \frac{\omega_m}{2\,\mathrm{c}} \,(\mathrm{n} - \mathrm{n}_m)\; \mathrm{L} \right\} + \mathrm{Sinc} \left\{ \frac{\omega_m}{2\,\mathrm{c}} \,(\mathrm{n} + \mathrm{n}_m)\; \mathrm{L} \right\}] \,. \tag{2}$$

Equation (2) allows us to compute the frequency-response of the electro-optic interaction, as determined by the phase-velocity mismatch.

Next I want to consider the amplitude of the modulating signal propagating on the transmission line. The bigger the modulating signal voltage, the more modulation we can expect. If the transmission line is low-loss (which it is, over the short length of the line) then the forward-propagating part of the modulating signal and the backward-propagating part (reflected) have the same amplitude and are in phase at the open-circuit end of the line. The amplitude of the forward-propagating wave is therefore half the amplitude of the signal at the open-circuit. Referring to Figure 5.2, the analysis is very simple.

$$\mathrm{Vt} = \frac{\mathrm{Z}_l}{\mathrm{Z}_a + \mathrm{Z}_l}\, \mathrm{V}_a \,, \tag{3}$$

$$\mathrm{Z}_l = \text{-j}\, \frac{\mathrm{Z}_o}{\tan \theta} \,, \tag{4}$$

$$\mathrm{V}_t = \mathrm{V}_{o/c} \,\mathrm{Cos}\, \theta \,, \tag{5}$$

$$\mathrm{V}_{fwd} = \frac{\mathrm{V}_{o/c}}{2} \,. \tag{6}$$

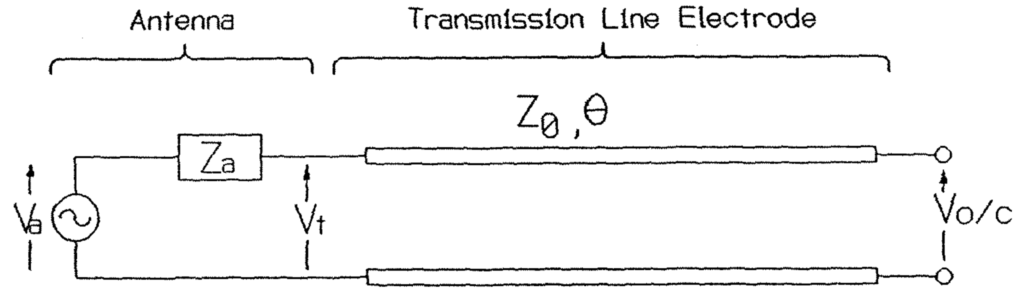

Figure 5.2 Equivalent Circuit Model of Modulator

Hence $$| V_{fwd} | = \frac{| V_a |}{2} \frac{Z_o}{| Z_a \operatorname{Sin} \theta - j Z_o \operatorname{Cos} \theta |} , \tag{7}$$

$$Z_a = R_a + j X_a , \tag{8}$$

$$V_a = 2 \sqrt{P_a R_a} , \tag{9}$$

where P_a is the power the antenna could deliver to a matched load $Z=Z_a^*$.

Hence $$| V_{fwd} | = \frac{Z_o \sqrt{P_a R_a}}{\sqrt{R_a^2 \operatorname{Sin}^2\theta + (X_a \operatorname{Sin} \theta - Z_o \operatorname{Cos} \theta)^2}} . \tag{10}$$

Equation (10) allows us to calculate the frequency response of the modulator if we know the center-frequency electrical length θ of the transmission line, its impedance Z_o, and the available power P_a and impedance Z_a of the antenna (which itself may be a function of frequency).

The impedance of a simple dipole antenna bears a well-known resemblance to the impedance of an open-circuited transmission line. For very short antenna lengths the impedance becomes very large and largely reactive, for antennas with a half-length approaching $\lambda/4$ the input impedance is very low and real, and for a half-length of $\lambda/2$ the input impedance is very high, but also real. Unlike the ideal transmission line, however, the antenna impedance is infinite only for zero length, and the impedance is never zero. This is because the antenna radiates, which makes it lossy. The simplest treatment of the antenna which allows for this is to treat it as a lossy transmission line, so that

$$Z_a = \frac{Z_{ao}}{\mathrm{Tanh}(\gamma \; L_a \;)} , \tag{11}$$

where
$$\gamma = \alpha + \mathrm{j} \; \beta \; . \tag{12}$$

Kominami et al. [1] have calculated antenna impedances for dipoles on a variety of substrates, although unfortunately they did not consider $LiNbO_3$. However, extrapolation of their results would suggest that for a dipole on a substrate of ϵ=36 the antenna impedance is close to

$$Z_a = \frac{95}{\mathrm{Tanh}(\; 0.157 \; \theta + \mathrm{j} \; \theta \;)} , \tag{13}$$

where θ (= 0.5 β L_a) is the electrical half-length of the antenna.

The power the antenna can deliver to a matched load, P_a, is a function of frequency also. Over narrow frequency ranges it can be assumed to be constant, but over wide frequency ranges it cannot. I made a very rough approximation to P_a by plotting the H-plane pattern of the dipole antenna (see Appendix A) and estimating the change in gain (and thus P_a) with frequency from the change in beamwidth. This resulted in the equation:

$$P_a \; \alpha \; 175.6 \text{ - } 6 \; \lambda + 0.167 \; \lambda^2 \; , \tag{14}$$

where λ is the free-space wavelength of the modulating signal. If this estimate for P_a is replaced by a constant, however, the calculated results do not change very much.

The transmission line itself is coplanar strip line. Rutledge et al. [2] have given the characteristic impedance (and also radiation loss) of this transmission line. Suppose the total width of the electrodes is W, and the gap between them is s, as in Figure 5.3. Then

$$Z_o = \eta_m \frac{K(k)}{K'(k)} , \tag{15}$$

and

$$\alpha_{rad} = \frac{20.2}{K'(k)\, K(k)} \left(1 - \frac{1}{\epsilon_r}\right)^2 \sqrt{1 + \frac{1}{\epsilon_r}} \left(\frac{W}{\lambda_d}\right)^2 \quad dB/\lambda_d , \tag{16}$$

where

$$K(k) = \int_0^{\pi/2} \frac{d\phi}{\sqrt{1 - k^2 \, Sin^2\phi}} , \tag{17}$$

and

$$K'(k) = \int_0^{\pi/2} \frac{d\phi}{\sqrt{1 - (1-k^2)\, Sin^2\phi}} , \tag{18}$$

and

$$k = s/W , \tag{19}$$

and

$$\eta_m = 120\, \pi \sqrt{\frac{1}{1 + \epsilon_r}} . \tag{20}$$

For the prototype modulator we used W=100 μm, s=8 μm, giving $Z_o \simeq 35\ \Omega$. We constructed a model of the modulator based on this information about the components. This model was to provide frequency response information only, not absolute response information. The predicted frequency response is shown in Figure 5.4.

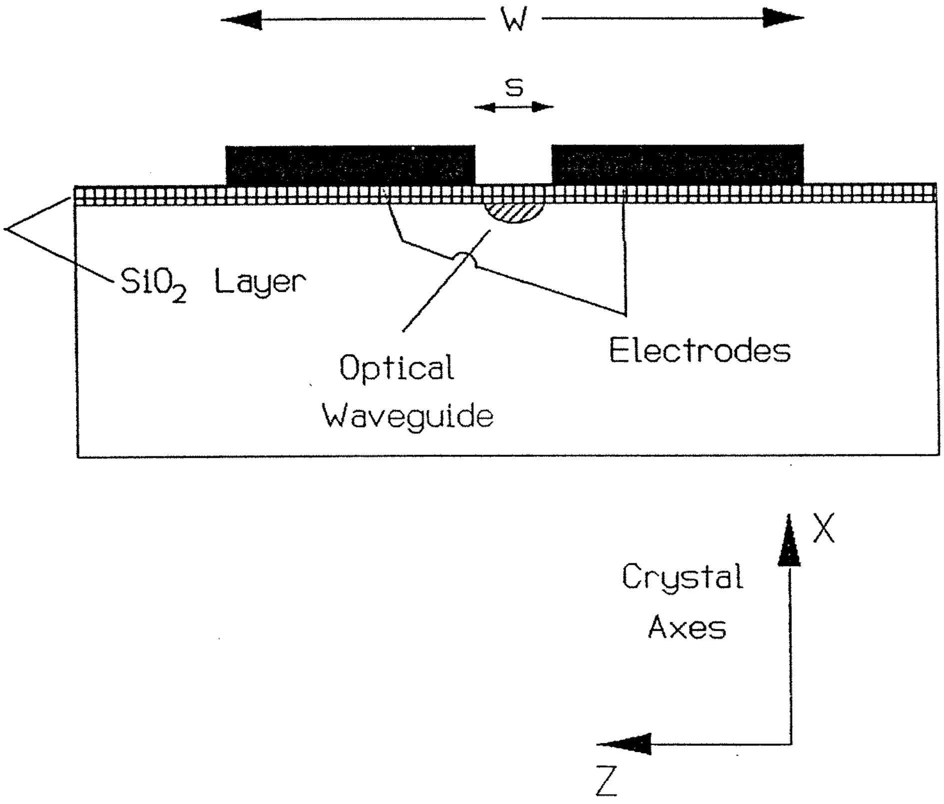

Figure 5.3 Coplanar Strip Transmission-Line Electrode Structure

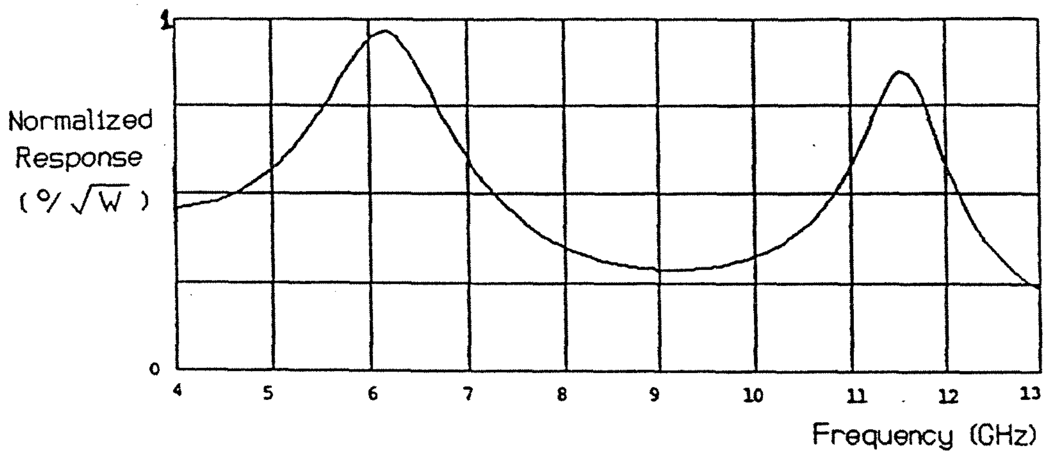

Figure 5.4 Predicted 10 GHz Prototype Modulator Frequency Response

5.3 Fabry-Perot Measurement Technique

Since the prototype modulator was a phase modulator, it was not possible to measure its performance by monitoring the output of a photodiode illuminated by the modulated optical beam. Photodiodes are completely insensitive to phase modulation. Instead we used a scanning Fabry-Perot interferometer as an optical spectrum analyser to look for the modulation sidebands. The Fabry-Perot is a very narrowband optical filter (bandwidth=13 MHz in the case of our Spectra-Physics 470-03), and by scanning its passband it is possible to measure only the light in the carrier at the photodiode, stripping off the power in the modulation sidebands, or conversely to measure the power in either of the sidebands alone.

When a carrier at frequency f_c is phase-modulated by a signal at modulation frequency f_m, it produces an infinity of sidebands at $f_c \pm nf_m$, n=1,2,3.... For small-signal modulation, however, only the two sidebands at $f_c + f_m$ and $f_c - f_m$ are significant. In this case each of these sidebands has sideband power

$$P_s = \frac{\phi^2 P_c}{4}, \tag{21}$$

where ϕ is the peak phase deviation, in radians, and P_c is the carrier power. Hence, by measuring the sideband/carrier power ratio P_s/P_c of a phase-modulated signal, it is possible to measure the amount of phase modulation present.

5.4 Experimental Setup

The modulator fabrication process is outlined in Appendix C, so I will not go into those details here. The experimental setup is shown in Figure 5.5. The optical signal source is a HeNe laser (λ_{opt}= 0.633 μm), mounted on a 2-axis translation stage for positioning. The optical beam (Gaussian, with diameter = 3 mm) is coupled into the modulator by a 40x microscope objective which brings the beam down to a beamwaist (diameter = 2 μm) at the optical waveguide input. At the output of the optical waveguide (at the other end of the modulator) there is another 40x objective which collimates the optical output into an output beam. This beam enters a scanning Fabry-Perot interferometer which is used as an optical spectrum analyser, as discussed above. The modulator itself is mounted on the face of a dielectric wedge, through which the modulating signal propagates. The dielectric constant of the wedge material (Stycast^R artificial dielectric from Emerson & Cuming) is 30 to approximate that of $LiNbO_3$, and the wedge is cut so that the modulating signal is incident on the antenna array at the required 23° angle. The modulating signal is coupled into this wedge from a rectangular metal waveguide via two quarter-wave matching layers of ϵ=3 and ϵ=10, again using Emerson & Cuming dielectric material (these values of ϵ do not provide precise matching, but the resulting match is effective over a wider bandwidth). The modulating signal source for the experiment was a Hewlett-Packard 0.01-20 GHz sweep oscillator. Because the experiment covers such a wide frequency range (5 - 13 GHz) it was necessary to use two different sizes of metal waveguide in the modulating signal feed (WR-137 & WR-90). Interestingly, there seems to be no change in the response of the modulator at the point where the waveguide size changes, even though the size of the dielectric wedge was the

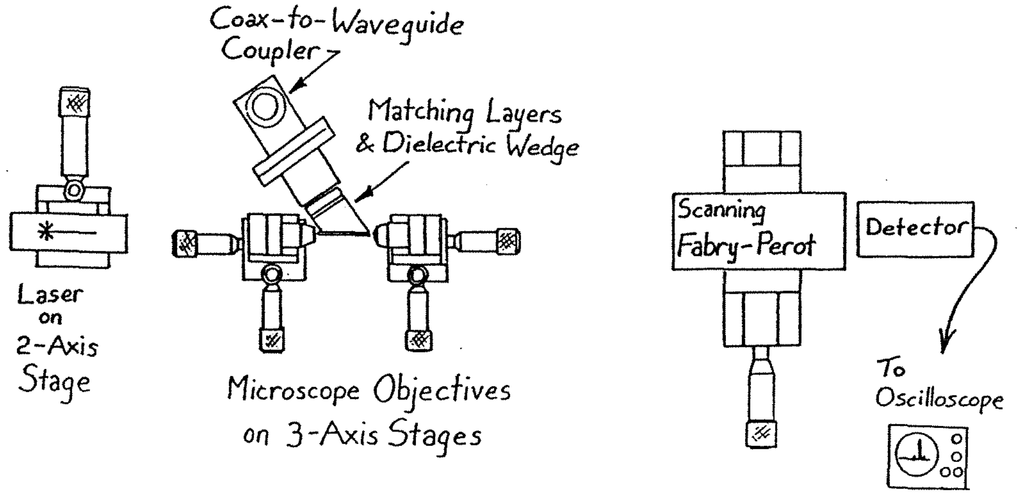

Figure 5.5 Prototype Phase Modulator Test Setup

same.

As this experiment involved aligning the optical elements, I will describe, briefly, how this was done.

Once the laser, microscope objectives, modulator and Fabry-Perot had been positioned approximately, the first step was to set the focus of the input microscope objective lens at the end-face of the modulator substrate. When the light, entering through the lens, struck this endface, some of it reflected back through the lens toward the laser. I put a beamsplitter in the path between the laser and the lens so that I could direct this reflected light onto a white card (since the wavelength was 0.633 μm I could see the beam on the card). When the lens was focussed properly the reflected beam was re-collimated by the lens and this produced a sharp spot on the white card.

Next the output lens position was adjusted so that this lens was positioned as far from the output end-face of the modulator as the input lens was from the input face. This gave a good approximation to proper focus at the output.

The position of the beamwaist on the input end-face of the modulator could be adjusted by moving the input lens. The beamwaist moved in the same direction as the lens. Ideally the beam should pass through the center of the lens, so this was not an ideal way to move the beam, but it was acceptable for small adjustments (if the lens was moved so that the beam was more than a little off-center, the beam would be steered so sharply that it would not couple into the optical waveguide). By moving the lens in a direction normal to the plane of the modulator in which the antennas lay ("up/down") it was possible to move the beamwaist to the edge of the substrate. When the beam struck the end-face of the modulator most of the light propagated through the substrate and re-emerged at the other end. The output lens imaged this light onto a white card, where I could see a dark region separated from a brighter region. The separation occured along a line, which was the image of the edge of the substrate. The brighter region appeared either uniformly bright or with interference fringes present. As the input lens was moved toward the edge of the substrate ("up") the interference fringes appeared and began to move farther apart until there was essentially only one fringe just before the beam was steered off the substrate entirely. As the beam was steered off the substrate there was a sudden change in the image, with bright and dark regions changing sides. Using this information I could position the beamwaist on the endface of the modulator very close to the edge.

Once I had positioned the input beam in this way I steered it parallel to the edge ("left/right") until it struck the input of an optical waveguide. When this happened the image of the output of the waveguide could be seen at once as a very bright spot in the image produced on the white card by the output lens.

When the waveguide had been "acquired" in this way I optimized the alignment of all the optical components iteratively to get maximum power through the optical waveguide. The laser and input lens had to be moved to get the beam passing through the center of the lens while still striking the end of the optical waveguide - this could produce a dramatic increase in output power. Once this had been done I re-adjusted the focus of the input lens. I then moved and focussed the output lens so that the beam was collimated into the Fabry-Perot. Finally, I aligned the Fabry-Perot with the beam.

$LiNbO_3$ is known to suffer from "optical damage" at 0.633 μm, and we were concerned that this might be a problem. Optical damage is the name given to the photorefractive effect when it is unwanted. At low levels it causes the output optical phase to wander. At high levels it produces scattering in the optical waveguide. The wandering optical phase is a problem in Mach-Zehnder amplitude modulators, but was not a problem in our high-speed phase modulator, since our Fabry-Perot measurement would be insensitive to the phase offset. The scattering in the optical waveguide caused the output intensity to vary, however, which was inconvenient during the measurement. The input optical power was limited to 0.5 mW to minimize this problem.

5.5 Experimental Results

Figure 5.6 shows the measured performance of this prototype modulator. The performance measure is shown as "degrees per $\sqrt{\text{Watt}}$." In the case of a more conventional phase modulator, with direct connections to the electrodes, one would measure degrees of phase modulation per Volt of modulating signal. However, in this case we cannot measure the voltage on the transmission line electrodes. Instead we can measure the signal power coming from the sweep oscillator. Of course, whatever voltage is present on the transmission line electrodes, it is proportional to $\sqrt{\text{oscillator power}}$. Hence we give results in degrees/$\sqrt{\text{Watt}}$. The power referred to is measured at the output of the signal generator. There is no correction for the power not coupled into the antennas. Thus, our quoted performance includes all coupling losses and inefficiencies, and

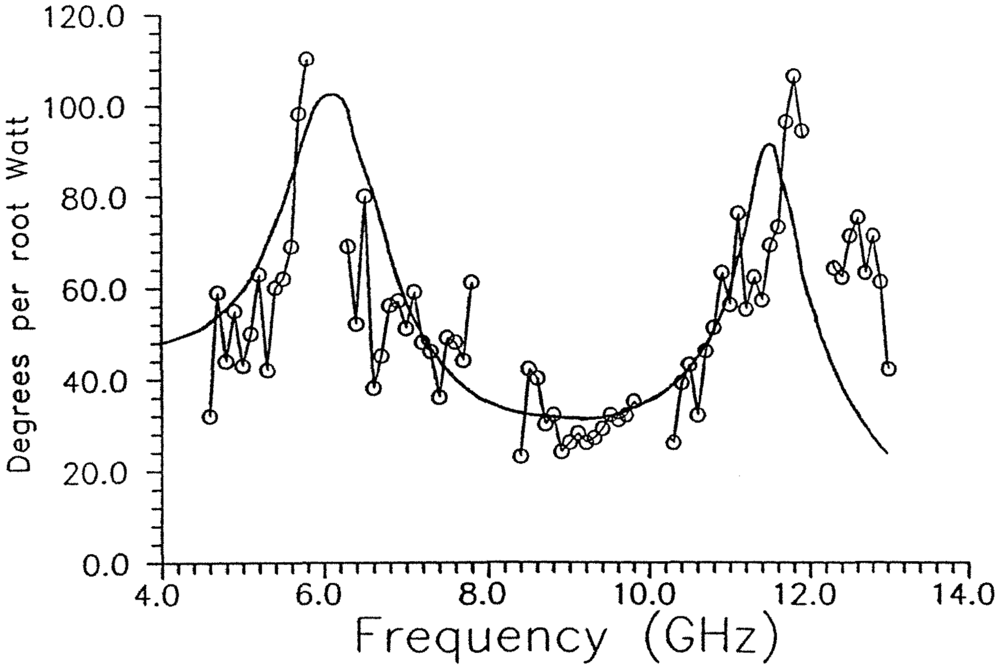

Figure 5.6 X-Band Prototype Modulator Frequency Response

Measured Frequency Response —o—

Frequency Response of Model ——

in this sense is a conservative measure.

The peak performance shown is approximately $110^\circ/\sqrt{W}$. This is comparable to the performance of a conventional traveling-wave modulator with direct connections, although not quite as good (see below). We were very pleased with the performance of this prototype modulator. While conventional modulators achieve somewhat better performance in this frequency range, we expected that antenna-coupled modulators would be superior at higher (mm-wave) modulation frequencies.

The frequency response, while having quite a bit of ripple in it, shows two clear peaks, one centered near 6 GHz, the other centered at 11.6 GHz. Unfortunately there are a few small gaps in our data over the frequency range covered in this measurement, because the free spectral range of the Fabry-Perot we used was 2 GHz. This meant that the Fabry-Perot produced aliased versions of the optical spectrum, repeating at 2 GHz intervals. Hence, whenever the modulation frequency is an integral multiple of 2 GHz, the sidebands fall in the same place in the spectrum as aliases of the carrier, so that the sidebands could not be measured. However, the measured frequency response is very similar to the frequency response predicted by the theoretical model (see below), suggesting that the behavior of this modulator is reasonably well-understood.

The idea behind using antennas to couple the modulating signal to the modulator, of course, was to allow for matching phase velocities of the modulating and optical signals. I wanted to confirm that the velocity-matching was, in fact, providing the expected benefit. In order to do this, I repeated the frequency response measurement with a number of different wedge angles, producing various illumination angles at the antenna array. I then plotted the average response (in degrees/$\sqrt{W}$) as a function of illumination angle. The measured result is shown in Figure 5.7, along with the theoretical prediction for a five-antenna modulator with cosine-squared distribution of power across the array. I varied the power across the antenna array in this way because this is the distribution of power at the output of the metal waveguide. If the antennas are all driven with equal power it does not change the predicted behavior much. The measured results show a peak at 23°, as expected, which was very gratifying. The expected nulls are not present, however. We believe that the reason for this is that the modulating signal feed is quite crude, and in particular there is a large reflection from the $LiNbO_3$-air interface at the antenna plane. This reflection results in RF power reflecting at many different angles in the signal feed, washing out the nulls in the response.

5.6 Comparison of Experimental and Theoretical Frequency Response

The theoretical model of the modulator predicts peak responses at 6.2 GHz and 11.5 GHz of approximately equal amplitude (the lower-frequency peak is slightly bigger). The minimum response between the peaks is predicted to be broad, between 8.5 and 10 GHz, with amplitude about one third that of the peaks.

The experimentally measured frequency response of the prototype modulator shows peak responses near 6 GHz and at 11.6 GHz. The peaks have essentially the same amplitude. The minimum response between the peaks is broad, between 8 and 10 GHz. The amplitude of the response at the minimum is

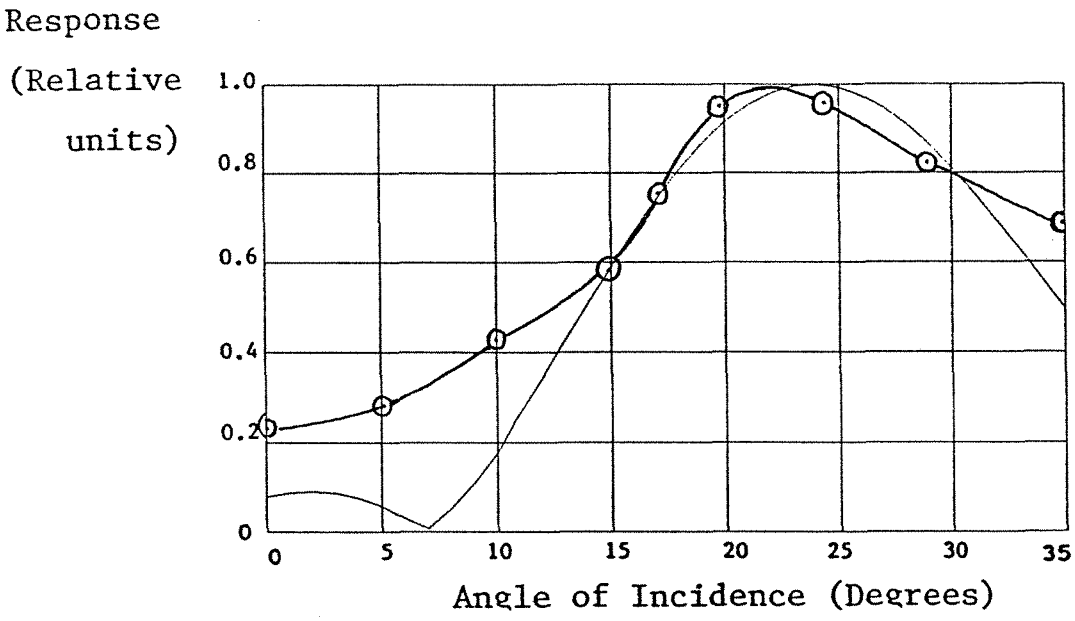

Figure 5.7 Modulator Response as a Function of Angle of Incidence of Modulating Signal

Measured points for X-band prototype modulator —o—

Theory : Five antennas illuminated by the signal
with a Sin^2 power-distribution —

about one third of the peak response.

The close correspondence between these features of the predicted and measured frequency response suggests that the behavior of this modulator is reasonably well understood, and is properly modelled. Based on this, we can say that the lower-frequency peak occurs when the antenna is about one half wavelength long (end-to-end) at the modulating signal frequency, while the transmission line electrode is about one quarter wavelength long. At this point there is an impedance match between the antenna driving-point and the input of the transmission line (which has an open circuit at the other end). The higher-frequency peak occurs when the antenna is about one full wavelength long, while the transmission line electrode is a half wavelength long. At this point there is another impedance match producing the peak response.

5.7 Comparison of Peak Performance with that of Conventional Modulators

I develop an expression for the performance of a conventional modulator in Chapter 8. Since conventional modulators are usually amplitude modulators, equation (5) of that chapter gives

$$\frac{m^2}{P_{in}} = 2\,R\left(\frac{\pi}{V_\pi}\right)^2 , \tag{22}$$

where m is the modulation index, P_{in} is the modulating signal power, R relates that power to the voltage on the electrodes according to $P=V^2/2R$, and V_π is the ON-OFF switching voltage of the modulator. The modulation index m is equal to the phase deviation (in radians) for small values of m, so we can convert this expression to give

$$\frac{\text{degrees}}{\sqrt{\text{W}}} = \sqrt{2\text{ R}}\ \frac{180}{\text{V}_\pi}\ . \tag{23}$$

For a conventional modulator R is usually 30 - 50 Ω. The switching voltage V_π is typically 6 - 10 V. This gives a range of performance:

$$\frac{\text{degrees}}{\sqrt{\text{W}}} = 140 - 300\ . \tag{24}$$

For actual examples in the literature, the value is rarely higher than $200°/\sqrt{W}$. Hence the performance of the prototype, at $110°/\sqrt{W}$, compares with that of conventional traveling-wave modulators, but is not quite as high.

5.8 Conclusion

We designed a simple antenna-coupled phase-modulator to demonstrate the concept behind the antenna-coupled high-speed modulator project. We constructed and tested this prototype modulator and showed that its performance was quite good, that its frequency response could be accounted for by a simple transmission line equivalent circuit model, and that the strategy for angle-matching the phase-velocities was working as predicted. This work has been reported in several papers [3 - 6].

References

[1] M. Kominami, D.M. Pozar, and D.H. Schaubert, "Dipole and Slot Elements and Arrays on Semi-Infinite Substrates," IEEE Trans. Ant. & Prop., Vol. AP-33, No. 6, June 1985

[2] D.B. Rutledge, D.P. Neikirk, and D.P. Kasilingam, "Integrated Circuit Antennas," Chapter 1, Infrared and Millimeter Waves, Vol. 10, Academic Press 1983

[3] William B. Bridges, Finbar T. Sheehy, and James H. Schaffner, "Wave-Coupled $LiNbO_3$ Electrooptícl Modulator for Microwave and Millimeter-Wave Modulation," IEEE Photonics Tech. Lett., Vol. 3, No. 2, pp. 133 - 135, Feb. 1991

[4] __________ , "Antenna-Coupled Millimeter-Wave $LiNbO_3$ Electro-Optic Modulator," Proc. IEEE/LEOS Summer Topical Meeting on Optical Millimeter-Wave Interactions: Measurements, Generation, Transmission, and Control. Newport Beach, California, pp. 16 - 17, 24-26 July 1991

[5] __________ , "Velocity-Matched Electro-Optic Modulator," High-Frequency Analog Fiber-Optic Systems , Proc. SPIE Vol. 1371, San Jose, California, pp. 68 - 77, 17 - 18 September 1990

[6] __________ , postdeadline paper presented at IEEE/LEOS Summer Topical Meeting on Broadband Analog Optoelectronics - Devices & Systems, Monterey, California, 23 - 25 July 1990.

6 Antenna-Coupled Millimeter-Wave Modulators

6.1 Design of the Narrowband 60 GHz Phase Modulator

Based on the success of the 10 GHz modulator, we decided to try to repeat the experiment at 60 GHz. We chose this frequency because we happened to have a klystron there to provide the modulating signal. Since the optical waveguide is not affected by the change in modulating signal frequency, its transverse dimension remained the same. This meant that the gap between the conductors of the transmission line electrode remained the same, and in order to keep the same transmission line impedance the other transverse dimensions of the transmission line electrode had to remain the same. However, the lengths of the transmission line segments and antennas were scaled to bring the center frequency of the modulator to 60 GHz, and the width of the antenna was reduced to keep its aspect ratio (length/thickness) high. In the scaling process the length of each segment was reduced to less than 1mm, so many more segments were needed for a 25 mm modulator substrate. In fact, there were 29 antenna/transmission line segments on the mask. The design is shown in Figure 6.1. The experimental results achieved with this modulator will be discussed in a later part of this chapter.

6.2 Design of the Broadband 60 & 94 GHz Amplitude Modulators

Once we had demonstrated that the basic idea of matching the phase velocities using antenna-coupling, we wanted to demonstrate a more practical design. The prototype designs at 10 GHz and 60 GHz were narrowband phase modulators operating at 0.633 μm. In practice one would like to see broadband amplitude modulators at 1.3 μm or 1.5 μm. So we had three changes to make:

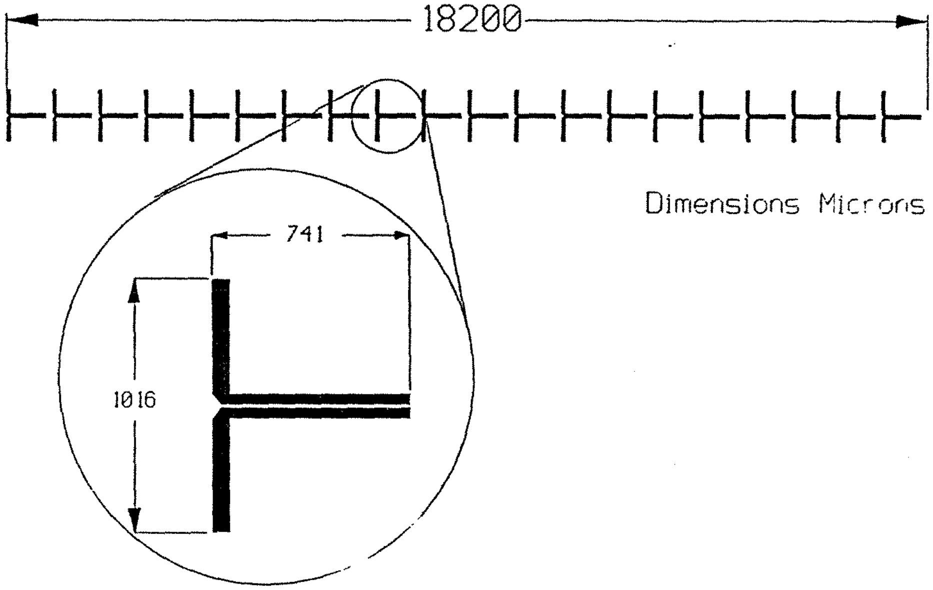

Figure 6.1 60 GHz Dipole Modulator

Gap between electrodes may be difficult to resolve at this scale.

design a broadband antenna/transmission line segment; design an amplitude modulator instead of a phase modulator; change the optical waveguide for 1.3 or 1.5 μm optical wavelength.

It was relatively easy to design the modulator for the new optical wavelength, requiring only a change in the dimensions of the optical waveguide (see Appendix C), although we did not yet have a suitable laser source for use with the new modulator. Designing an amplitude modulator meant splitting the optical signal into two paths to make a Mach-Zehnder amplitude modulator. The optical splitting and recombining is achieved using Y-junctions. The Y-junction is a transformation of the optical waveguide from a single guide into two separate waveguides (or vice-versa), with the power split equally between them. This is done by first gradually widening the input waveguide, then splitting it in the center and gradually moving the two halves away from each other. The angle at which the two sides diverge is usually less than 1° in order to minimize optical losses. The waveguides must be separated by enough distance to ensure that there will be no cross-coupling between them, and because of the small divergence angle this can take considerable distance - several millimeters, in fact. Consequently the Y-junction takes up quite a bit of the space on the 25 mm modulator substrate. Again, however, this is not a difficult design issue.

There were two difficult design issues: first, designing a broadband antenna/transmission line segment; second, arranging for DC bias to be applied to each of the segments. Using the theoretical model developed for the 10 GHz prototype, I established that if the antenna could be made to have a constant impedance which was similar to the characteristic impedance of the transmission line electrode, the bandwidth of the antenna/transmission line segment would be large. Constant-impedance or near-constant-impedance antennas exist as frequency-independent antennas or nearly-frequency-independent antennas such as spiral antennas and log-periodic antennas. However, it turns out that these antennas are too big for this application. The antennas are so large that very few antenna/transmission line segments would fit on the substrate. Instead we chose to use short bow-tie antennas. Long bow-tie antennas are frequency-independent, but have no main beam on the axis of symmetry, and so would not be very useful here. Compton et al. [1] have pointed out that long bow-tie antennas are traveling-wave antennas, and each half of the antenna transmits its own beam into the substrate. Essentially the traveling wave in each half of the antenna radiates downward into the substrate at an angle to the direction of propagation of the wave in the antenna arm. Short bow-tie antennas are not frequency-independent, but are quite broadband [1] and have antenna patterns similar to dipole antennas. In addition, these antennas are reported to be less sensitive to perturbations such as bias-connections made at their ends.

The length of the transmission line electrode no longer had to be chosen to resonate with the antenna at the center frequency. However, the choice of length was limited by phase-velocity mismatch considerations, which prevented any significant increase in the length of the electrode. We used electrodes whose length was $\lambda/2$, where λ is the effective wavelength in the electrodes, i.e., $\lambda_o/3.8$.

The substrate to be used was X-cut, which meant that the optical waveguides needed to be modulated with a field parallel to the surface of the substrate. With only two conductors in the transmission line electrode, we chose to position the antenna/transmission line segments so that one optical waveguide ran along the center of the transmission line electrode gap (as in Figure 5.3), with the other optical waveguide running under the metal of one of the conductors, well away from the gap. The electric field in this second region is very small.

The design of the 60 & 94 GHz broadband amplitude modulator metal masks is shown in Figure 6.2. The figure shows close-up views of individual segments as well as each entire modulator. The close-up view shows the bow-tie antenna and electrode (the gap between the electrode conductors cannot be seen at this scale). At the ends of the bow-tie antenna the antenna does not end abruptly, but is continued at each end by metallization whose width is equal to the width of the end of the antenna. This is intended to reduce the amplitude of the reflection at the end of the antenna, thereby increasing the bandwidth as much as possible. The end of this metallization is believed to have negligible effect on the antenna's behavior (because the RF is expected to have radiated most of its power before reaching this point), so it is connected to a bias-pad by a thin metal strip, as shown in the view of the entire modulator mask. The performance of these modulators will be discussed in a later section.

6.3 Study of Phasefront Curvature in Scale Model of Feed

As I described in Chapter 4, if the number of antenna/transmission line segments becomes large then the modulating signal incident on the array must

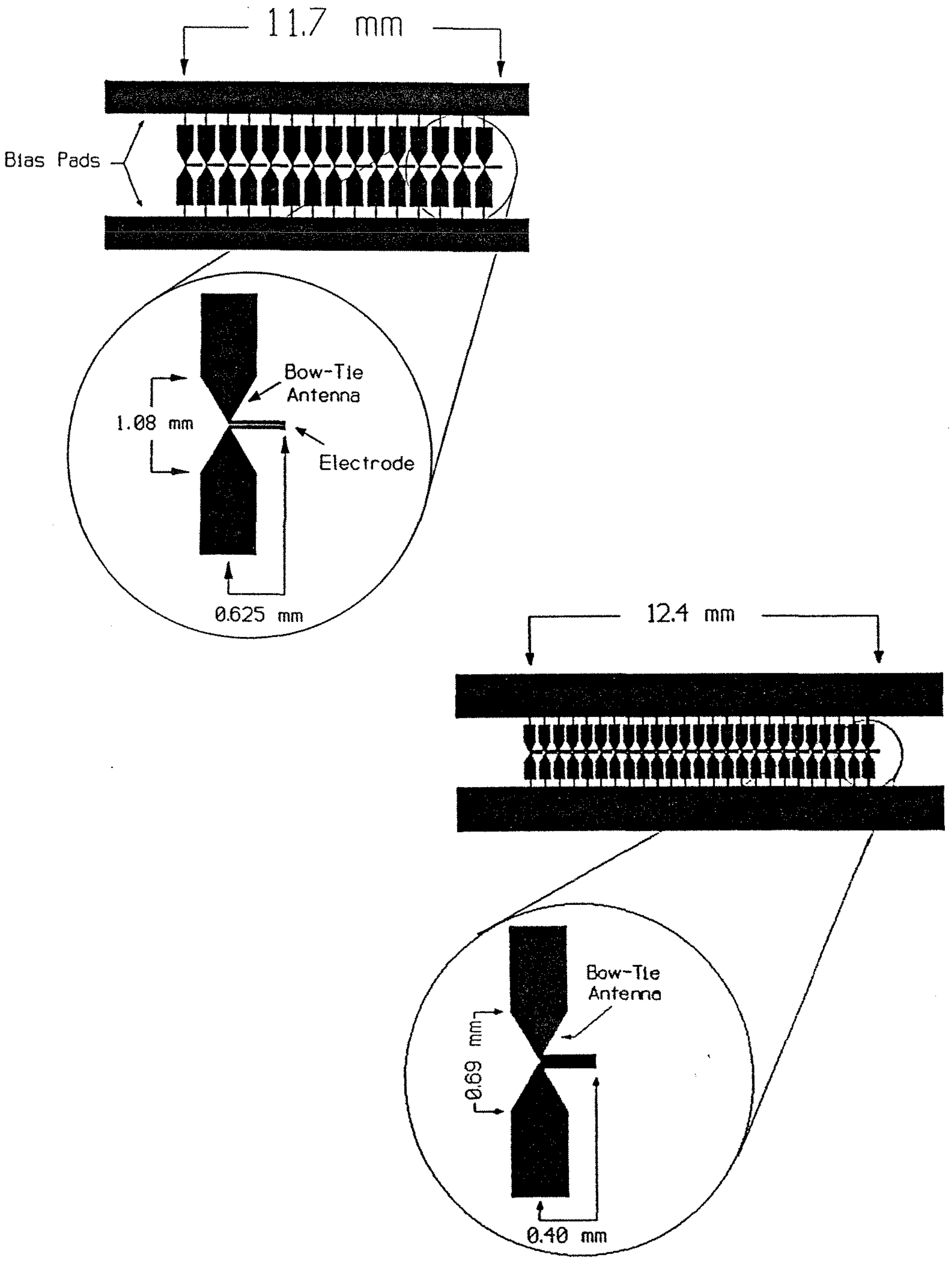

Figure 6.2 60 & 94 GHz Bow-Tie Modulators

Gaps between electrodes cannot be resolved at this scale.

be very close to a pure plane wave and must be incident at an angle very close to the optimum. This amounts to saying that the radius of curvature of the phasefronts of the modulating signal must be very large, and the angle of incidence must be very accurate.

The accuracy of the angle of incidence is a matter of accurate cutting of the end of the modulating signal feed, but for large phasefront curvature some careful design may be required. We wanted to know what kind of phasefront curvature would occur in the modulating signal feed we would use. The feed we proposed to use is described in more detail in part 6.4 of this chapter. To determine whether this feed would provide acceptable phasefront curvature, I built a scale model of the tapered dielectric waveguide part of the proposed signal feed (Figure 6.3) and measured the phasefront curvature at various points on the feed. Figure 6.4 shows the experimental setup for the measurement. The perturber reflected some of the wave being guided by the dielectric taper, and this reflection was mixed with a sample of the original signal at the detector. This arrangement constitutes a phase detector. By positioning the perturber at the points above the taper which minimized the output from the detector, I could plot the locus of points having a constant phase. The first taper I tried was 600 mm long, with an end-aperture of 118 mm. The test frequency was 10 GHz. I found that the deviation of the phasefronts from flat at the end-aperture was no more than 1.5 mm over the entire width, which meant that the phase error was less than 23°. I next tried the same experiment with a much shorter taper, 220 mm long with a 112 mm end-aperture. In this case I found that the radius of curvature of the phasefronts had a minimum a short distance outside the mouth of the feedhorn I was using (see Figure 6.5). Note that the

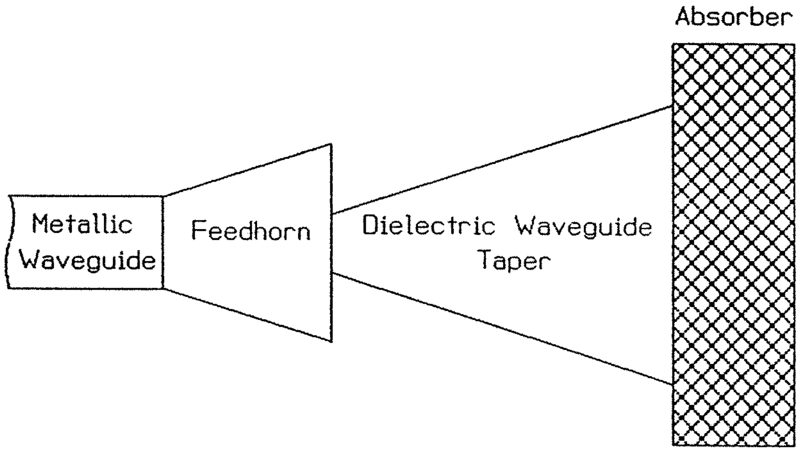

Figure 6.3 Scale Model of Feed

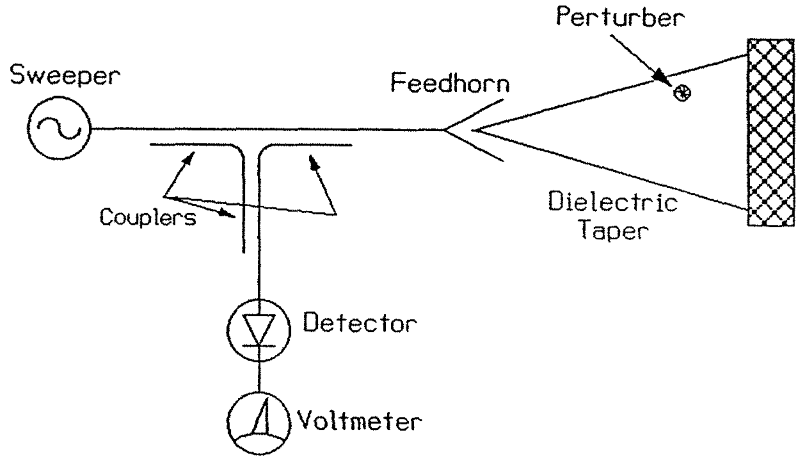

Figure 6.4 Scale Model Phasefront Measurement: Experimental Setup

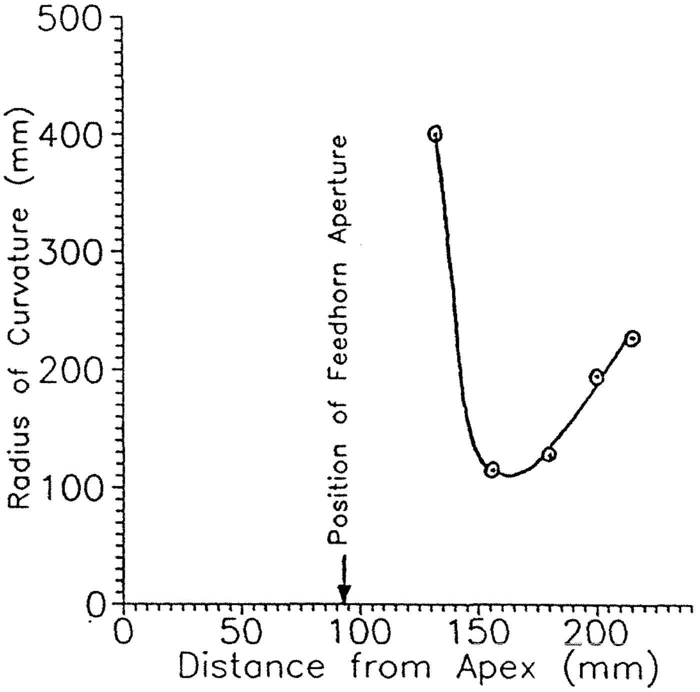

Figure 6.5 Measured Radius of Curvature of Phasefronts

phasefront radius of curvature is sharply increased when the signal is coupled into the $LiNbO_3$ wedge, because of refraction, but the maximum phase-error remains the same. In this experiment I made no effort to simulate the $LiNbO_3$, so the radius of curvature is measured in the low-ϵ material. At the end-aperture the radius of curvature was approximately 260 mm, corresponding to a maximum phase-error of 90°. This would produce a 1.6 dB reduction in modulator response.

During the actual mm-wave modulator experiments it was necessary (for reasons of spacing on the table) to use a dielectric taper longer than the scaled length of either of these experimental tapers. For this reason I expect that phasefront curvature was not a problem during the mm-wave experiments.

6.4 Experimental Setup

The mm-wave experiments were performed at both 0.633 μm and 1.3 μm optical wavelength. For the 0.633 μm wavelength we used the same HeNe laser and Fabry-Perot interferometer as before. For 1.3 μm we used a diode-pumped YAG laser as the optical source. Both could provide a single optical wavelength with a narrow linewidth, which was necessary for measurements with a scanning Fabry-Perot. The light was coupled into and out of the optical waveguide using 40x microscope objectives, as before (at the 1.3 μm wavelength the 40x microscope objective focussed a 4 mm input optical beam to a 3 μm spot at the optical waveguide input, while at 0.633 μm optical wavelength the input beam and spot sizes were 3 mm and 2 μm respectively). The modulation was detected by optical spectrum analysis, as before, but we had to obtain a new Fabry-Perot with 1.3 μm mirrors for operation with the YAG laser.

The alignment of the optical components followed the same general procedure as outlined in Chapter 5, section 5.4, except that the 1.3 μm beam is not visible. It was possible to see the beam using an infrared phosphor card, although when alignment was poor the beam could be very weak, which meant that dark-adjusted eyes could barely see the glowing phosphors in complete darkness - a situation which made working with equipment rather difficult!

The modulating signal feed was loosely based on the X-band prototype design. The RF was coupled from rectangular metal waveguide to a tapered dielectric slab waveguide which increased the width over which the RF was spread from the width of the metal waveguide (WR-15, width = 3.81 mm, aspect ratio 2:1) to the length of the modulator antenna array (length approximately 12 mm, aspect ratio 12:1 to 18:1). The RF power then propagated through a quarter-wave matching layer (Stycast^R ϵ=9) into a slab of $LiNbO_3$ which also acted as a dielectric slab waveguide. This slab had constant width, but was cut at an angle to ensure that the RF would be incident on the antenna array at the correct angle. Since $LiNbO_3$ is anisotropic, the slab of material being used as the dielectric waveguide was z-cut so that its crystal axes aligned with those of the x-cut $LiNbO_3$ modulator substrate. The experimental setup and modulating signal feed are shown in Figure 6.6.

6.5 Scaling Law for Antenna-Coupled Modulators

There is a scaling law for antenna-coupled modulators which can be used to predict performance when design/operating parameters are changed. The sensitivity of the modulators (measured in degrees of phase modulation per

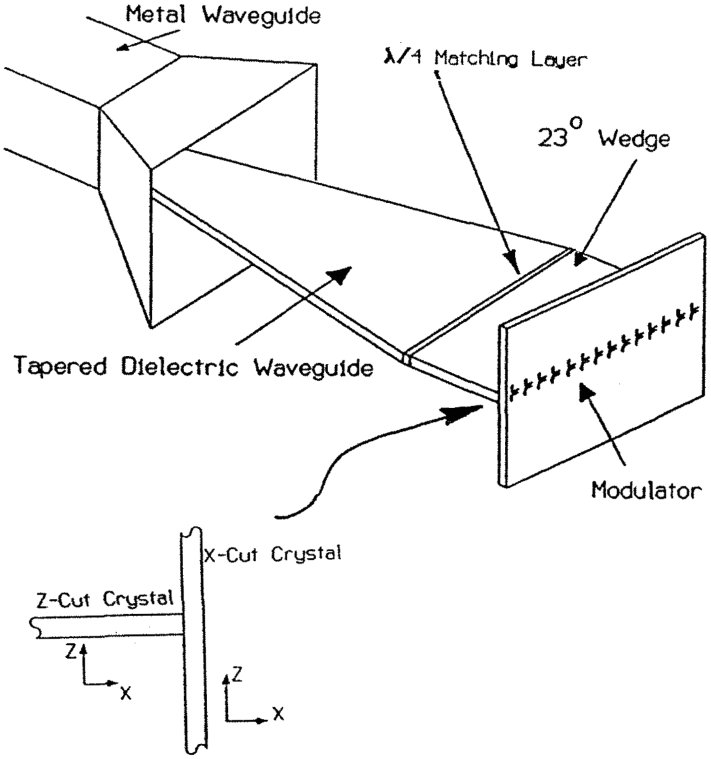

Crystal Orientation of Feed is
Matched to that of the Modulator.

Figure 6.6 60 GHz Dipole Modulator with Signal Feed watt$^{1/2}$) scales according to the factor $\frac{L}{\lambda\sqrt{N}}$, where N is the number of antenna/transmission line segments, L is the total interaction length (i.e., L= N.ℓ, where ℓ is the length of an individual segment), and λ is the optical wavelength. The dependence on L and λ are common to all electrooptic phase modulators. The length ℓ of an individual segment is inversely proportional to the signal frequency, in order to ensure that the segment has sufficiently large bandwidth. Hence if the interaction length L is fixed, the number of segments is proportional to the center frequency f, so the sensitivity is proportional to $\sqrt{1/f}$. On the other hand, given a center frequency, the sensitivity can be increased by increasing the interaction length L. However, this also involves increasing N by the same factor, so the net increase in sensitivity is proportional to $\sqrt{L}$.

6.6 Narrowband Phase Modulator Results at 60 GHz

The narrowband phase modulator was based on the 10 GHz prototype we had demonstrated previously. I used the mm-wave feed described above to bring the modulating signal from the 60 GHz klystron to the modulator. The process used to polish the end-faces of the modulator substrate destroyed a few of the antennas at each end of the substrate so that only 20 antennas remained of the original 29, giving a total interaction length of 18 mm. The damaged antennas were located under the small $LiNbO_3$ pieces used temporarily at each end to protect against chipping the edges during polishing. An interesting feature of antenna-coupled modulators is that shorting or otherwise destroying part of the modulator in this way simply reduces the sensitivity. By contrast, it would render a conventional modulator useless.

During this experiment I had an E-H tuner at the waveguide end of the feedhorn in order to get the best possible impedance-match in the mm-wave feed. Subsequent experience has suggested that this was a bad idea, and that much of the frequency-response structure we observed may have been determined by this tuner. We were unable to confirm this, however, due to the untimely demise of the 60 GHz klystron, a victim of a murderous "failsafe" filament protection circuit in a commercial power supply.

The experimental results are shown in Figure 6.7. The peak response is almost $80^\circ/\sqrt{W}$, which is very good. The bandwidth appears small, although it is not clear whether this is due to the E-H tuner or something else. The frequency range over which the performance could be measured was limited by the tuning range of the klystron. Based on the results at 10 GHz and the scaling law, we would have expected performance of about $40^\circ/\sqrt{W}$ with this modulator. The higher sensitivity suggests that this modulator is coupled to the modulating signal more efficiently than the prototype 10 GHz modulator was. Since the other millimeter-wave modulators have essentially the same RF feed as the new modulator, we will use it as the basis for comparison for the other mm-wave modulators.

6.7 Broadband Modulator Results at 60 GHz

The next modulator tested was the 60 GHz broadband Mach-Zehnder amplitude modulator. This modulator was designed for operation at 1.3 μm optical wavelength, but the substrate arrived several months before a suitable 1.3 μm laser was available. The modulator would not work as an amplitude modulator at 0.633 μm optical wavelength because the 1.3 μm optical

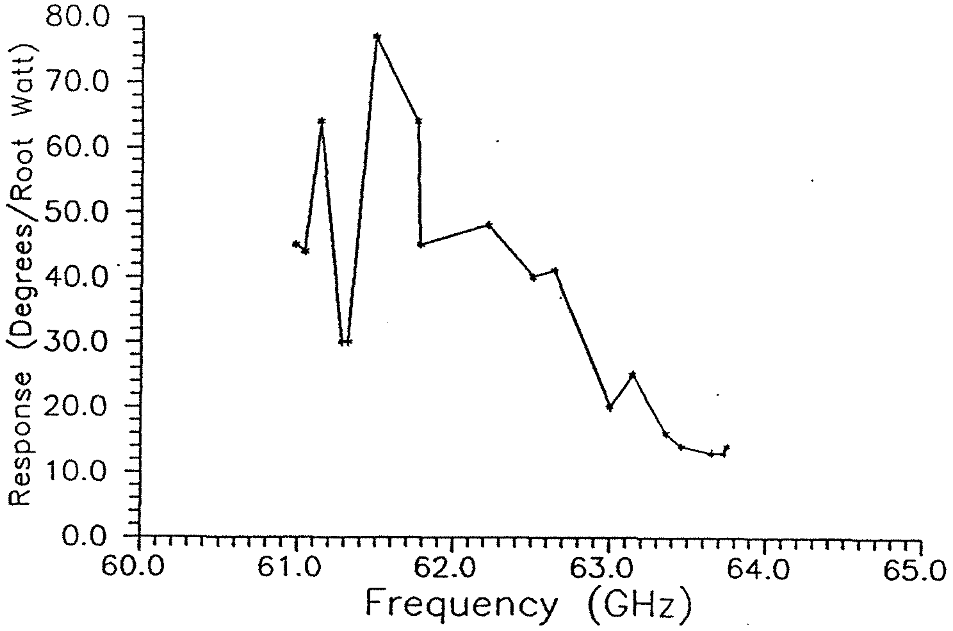

Figure 6.7 60 GHz Dipole Phase Modulator: Experimental Results

waveguide was multimoded at the shorter wavelength, but it would work as a phase modulator. In this case the modulator would be biased to the point where the optical delay through the two arms were equal. The modulator would phase-modulate one arm, and the output of this arm would be added to the unmodulated output of the other arm. This would produce an output which was phase-modulated by half as much as the single arm.

I went ahead and made this measurement, and derived single-arm phase modulation results from it. These results are shown in Figure 6.8. The peak response is about $26^\circ/\sqrt{\mathrm{W}}$.

Unfortunately I was not able to measure the performance of this modulator at 1.3 μm optical wavelength, as originally intended, because the klystron was destroyed by the faulty commercial klystron power supply before the 1.3 μm laser arrived. A dirty potentiometer caused the beam-voltage power supply to generate a voltage spike, triggering a fault in the filament "protection" circuit (which was incorrectly designed), which, in turn, applied an over-voltage to the klystron filament, which burned out. Owners of Harris Model PRD Type 819 A klystron power supplies should modify this circuit if they value their klystrons!

The broadband antennas were expected to reduce the response by a factor of 2 compared to dipole antennas, and the interaction length was reduced even further, from 18 mm to 12 mm. This resulted in an expected peak performance of $30^\circ/\sqrt{\mathrm{W}}$. The measured peak response of $26^\circ/\sqrt{\mathrm{W}}$ is consistent with this.

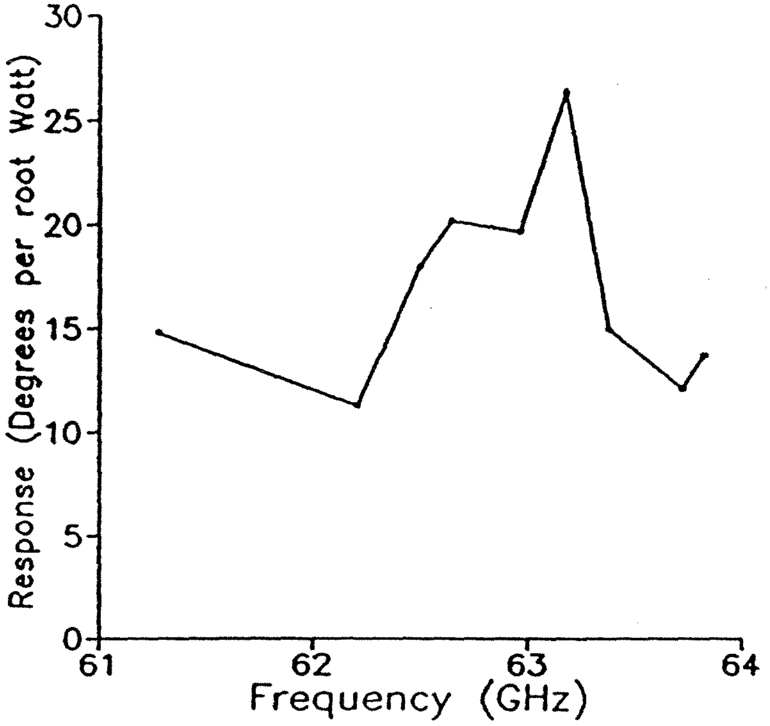

Figure 6.8 60 GHz Bow-Tie Modulator: Experimental Results

6.8 Broadband Modulator Results at 94 GHz

The 94 GHz broadband modulator was based on the same design as the 60 GHz broadband modulator (Figure 6.2). However, there were now 25 antennas covering a 12 mm interaction length. The feed system was very similar. Compared to the 60 GHz narrowband phase modulator's performance (with dipoles) at 0.633 μm we expected to see reduced performance due to the longer optical wavelength, shorter interaction length (12 mm), increased number of antenna/transmission line segments, and use of broadband (non-resonant) antennas. The scaled value predicted for a single-arm response was $12^\circ/\sqrt{\text{W}}$. Since this modulator is a Mach-Zehnder amplitude modulator, this corresponds to a modulation index squared per Watt (m^2/W) of 0.044.

The measured response is shown in Figure 6.9. Although this modulator is an amplitude modulator, and photodiodes are sensitive to amplitude modulation, there are no photodiodes available which can respond to modulation at 94 GHz. Consequently we again used the scanning Fabry-Perot technique to look at the modulation sidebands in order to measure the modulator's performance. There is a gap around 96 GHz in the response shown in Figure 6.9 because of the 8 GHz free spectral range of the 1.3 μm scanning Fabry-Perot, which results in the 12^{th} alias of the optical carrier falling on the sideband, making it impossible to measure. This modulator's performance is about $\text{m}^2/\text{W}{=}0.055$ over the measured range, corresponding to single-arm phase modulation of $13^\circ/\sqrt{\text{W}}$. This is consistent with the result expected from applying the scaling law to the 60 GHz phase modulator. The 94 GHz modulator does have a peak response of $\text{m}^2/\text{W}= 0.072$, corresponding to single-arm phase modulation of $15^\circ/\sqrt{\text{W}}$, which is somewhat higher than expected. The frequency range was again limited by

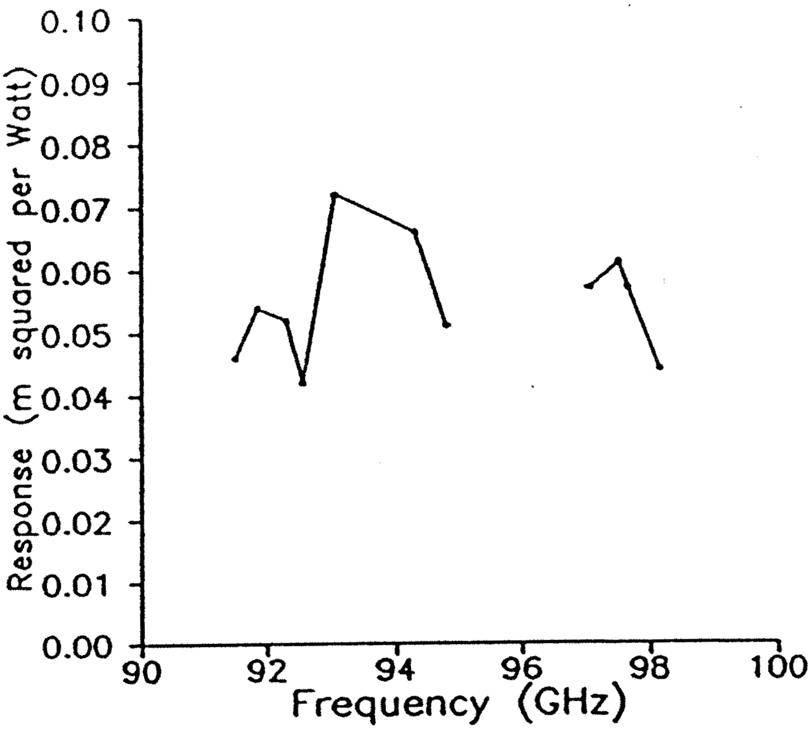

Figure 6.9 94 GHz Bow-Tie Amplitude Modulator: Experimental Results at 1.3 μm

the tuning range of the klystron, so we can only say that the 3 dB bandwidth is greater than 7 GHz.

6.9 Design of the 94 GHz $\Delta\beta$ Coupler-Modulator

When James H. Schaffner at Hughes Research Laboratories informed us that he was preparing some optical waveguide masks for $\Delta\beta$ coupler-modulators (see Figure 6.10), we decided it would be interesting to try to design a mm-wave $\Delta\beta$ coupler-modulator. Just as for a Mach-Zehnder modulator, the switching voltage required by a $\Delta\beta$ coupler-modulator is inversely proportional to the interaction length, and increased electrode length gives rise to reduced bandwidth in conventional $\Delta\beta$ modulators (see Chapter 2, section 2.11), so our antenna-coupled phase-velocity matching technique is relevant.

We decided to go back to dipole antennas because this would be our first venture into this type of modulator. Since dipole antennas and open-circuit transmission-lines give rise to resonant modulator structures, they give higher performance at the center frequency, maximizing the chance of detecting the sidebands. The drawback to this idea was that it would be impossible to apply DC bias to the antennas.

I designed the modulators with three sections: two DC-biased sections, one at the input and one at the output, and an antenna-coupled section consisting of the array of antenna/transmission line segments. The idea was to apply bias to the DC sections so that if the signal only were applied to the antenna-coupled section (i.e., no bias in that section) there would be a variation in the output intensity.

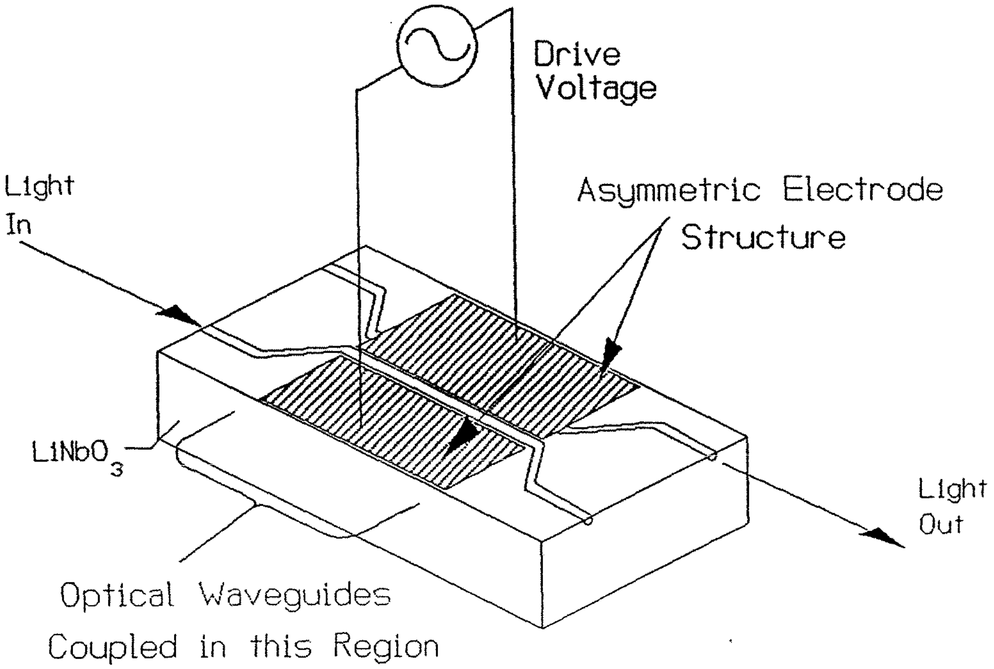

Figure 6.10 $\Delta\beta$ Coupler with Asymmetric Electrodes

I tested this design concept with a simple model of the modulator. The model consisted of five $\Delta\beta$ couplers cascaded. The first coupler had DC bias only. The second, third, and fourth were driven by the signal only, with no DC bias. The fifth had DC bias only. I could apply different DC biases to the first and fifth couplers, or the same DC bias. Similarly, I could apply the same signal level to the second, third, and fourth couplers, or choose some other distribution. For a more realistic model I could have had ten or twelve sections driven by the signal only, each one representing an antenna/transmission line segment. For still greater realism I could have had short sections with neither signal nor bias in between all the others, representing the gaps. All of this would have required long computer run-times and I felt that I would not learn much more anyway. The simple model I used suggested that it would be quite easy to get modulation using a design like this.

The individual antenna/transmission line design was based on the original 10 GHz prototype, scaled appropriately.

The mask design and antenna/transmission line details are shown in Figures 6.11 and 6.12. The modulators were fabricated at Hughes Research Laboratories and returned to Caltech for testing.

At this point some difficulties became apparent. It is very difficult to fabricate identical optical waveguides, and in any case $LiNbO_3$ stores charge in the crystal structure. Both of these facts mean that zero bias on the antennas does not necessarily mean $\Delta\beta$=0 for the underlying coupled optical waveguides. The

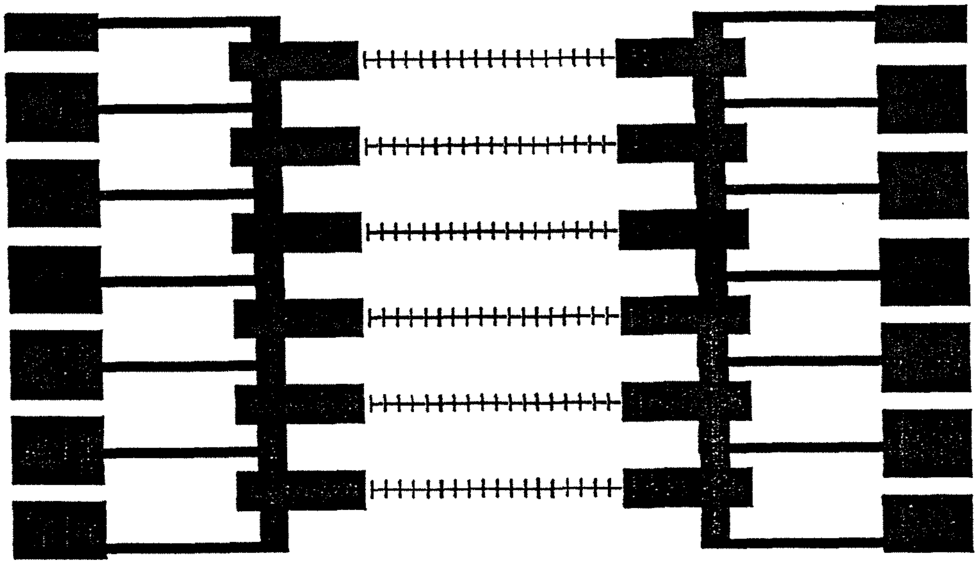

<u>Figure 6.11</u> 94 GHz $\Delta\beta$ Coupler-Modulator Mask Design

There are 6 modulators here. The antenna/electrode segments are visible at the center of each modulator. The bigger dark areas are the DC bias electrodes and DC bias pads.

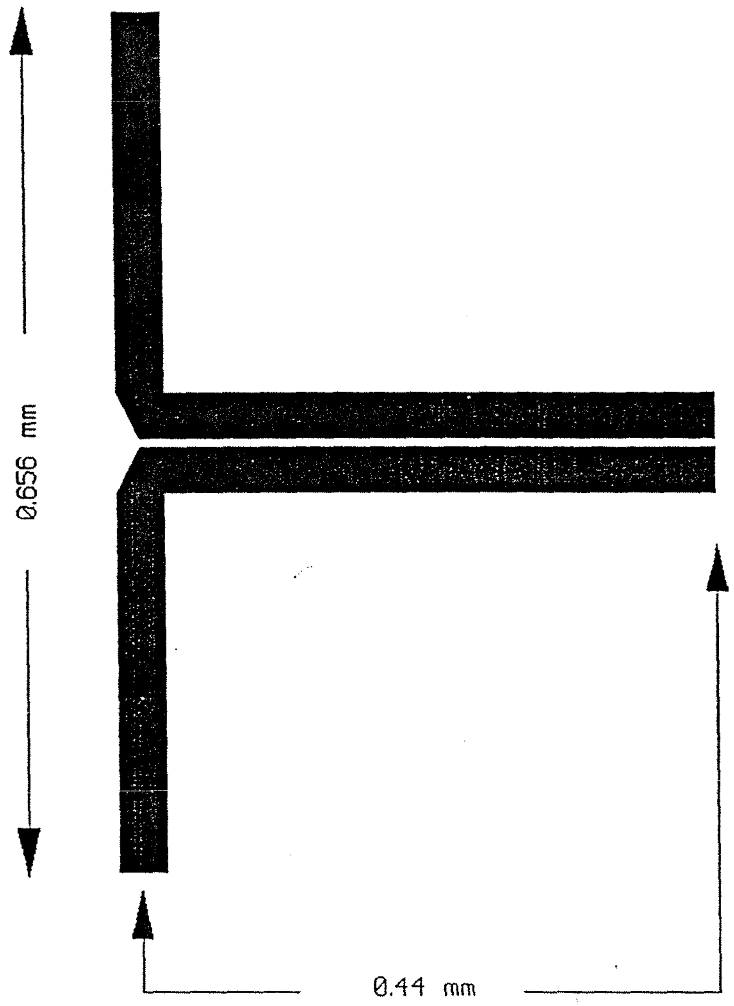

Figure 6.12 94 GHz $\Delta\beta$ Coupler-Modulator Design Details

DC bias characteristics of the modulators did not look at all like the characteristics expected from the model, and with no way to apply bias to the transmission line electrodes, we could not establish why. Furthermore, knowing that we would have to measure the modulation performance using the scanning Fabry-Perot technique again, I realized that this time it would be more difficult because a $\Delta\beta$ coupler-modulator does not produce pure amplitude modulation. It produces mixed amplitude and phase modulation. In order to determine the amount of amplitude modulation present from the sideband amplitude, we would need to be confident that we understood the modulator's behavior. Since we did not understand its DC bias behavior, it was hopeless to attempt to measure its amplitude modulation performance at 94 GHz.

6.10 Conclusions

Following on the original success of our 10 GHz prototype, we have demonstrated sensitive antenna-coupled integrated $LiNbO_3$ electro-optic modulators at 61-63 GHz and at 91-98 GHz. No other workers are operating modulators at these frequencies to date, and we do not expect the performance of competing modulators to exceed the performance we have achieved any time soon. We have tested narrowband and broadband designs. The measured results are consistent with the proposed scaling law for antenna-coupled modulators. Sensitivity can be increased by increasing the number of segments to obtain greater interaction length, and by improving on the simple slab waveguide illumination scheme. We have estimated that performance improvements of up to 12 dB may be possible. This can be done without affecting the bandwidth, which remains equal to the bandwidth of a single antenna/electrode segment. This work has been published in [2 - 3].

Our first attempt at designing an antenna-coupled $\Delta\beta$ modulator was not entirely successful, but was educational. We have not yet determined why this modulator does not work as expected, but intend to find out. It may be necessary to use biased antenna/electrode segments in future designs to allow for asymmetry between the optical waveguides as a result of thermal or mechanical stress effects, or asymmetry resulting from fabrication.

References

[1] R.C. Compton, R.C. McPhedran, Z. Popovic, G.M. Rebeiz, P.P. Tong, and D.B. Rutledge, "Bow-Tie Antennas on a Dielectric Half-Space: Theory and Experiment," IEEE Trans. Ant. & Prop., Vol. 35, No. 6, pp. 622-631, June 1987

[2] Finbar T. Sheehy, William B. Bridges, and James H. Schaffner, "60 GHz and 94 GHz Antenna-Coupled $LiNbO_3$ Electrooptic Modulators," IEEE Photonics Tech. Lett., Vol. 5, No. 3, pp. 307 - 310, March 1993

[3] William B. Bridges, Finbar T. Sheehy, and James H. Schaffner, "Antenna-Coupled Millimeter-Wave $LiNbO_3$ Electro-Optic Modulator," Proc. IEEE/LEOS Summer Topical Meeting on Optical Millimeter-Wave Interactions: Measurements, Generation, Transmission and Control, Newport Beach, California, pp. 16 - 17, 24 - 26 July 1991

7. Design and Implementation of Linearized $\Delta\beta$ Electro-Optic Modulators – A Theoretical Study

7.1 Introduction

In optical communication systems, external modulation of a laser can provide attractive advantages over direct modulation of the laser. Usually, however, the nonlinearity of external modulators is worse than that of directly-modulated lasers. Directly-modulated lasers have very little third-order nonlinearity, but this is not generally true of external modulators. The transfer-function of a Mach-Zehnder electro-optic modulator is sinusoidal, for example, and that of a $\Delta\beta$ coupler modulator is a sinc^2 function. Usually these modulators are operated at the inflection-point of the transfer function to minimize second-order distortion. However, third-order and higher-order distortion is present, and this is a problem in applications requiring high dynamic range. As a result of studies being performed at Hughes Research Laboratories by Bridges, Schaffner, and others, I became interested in certain aspects of this problem, which are reported here. The final report on the Hughes study [1], by Schaffner et al., refers to some of the results of this work, although not entirely accurately.

The $\Delta\beta$ modulator can be linearized to a significant degree. I will discuss how and why this can be done, and evaluate the benefits of doing so. Specific examples of linearization methods have been given by Lin et al. at the University of California at San Diego [1,2] and by Lam and Tangonan at Hughes Research Labs [3]. I will show that these cascade-type linearization schemes add at most four degrees of freedom which can be used to modify the modulator transfer function. I will show how these degrees of freedom can be separated, so the search for solutions becomes straightforward, if tedious. Finally, I will discuss how to realize a given solution in a way which is suitable for practical implementation, and give examples.

7.2 Cascade Linearization of $\Delta\beta$ Modulators

The $\Delta\beta$ modulator is a 4-port device, but when it is used as a modulator only two of the four ports are used. The modulator is an electrically-controlled coupler. Optical power is applied to one of the two input ports, and the output is taken from one of the two output ports. The output ports are complementary to each other, so either port can be used, depending on the desired signal polarity. Since this device has four ports, one may wonder whether it is possible to change the transfer function by using all four ports in some way. In fact, there are many possible ways to do so, but I will introduce a constraint here, which is that the input signal, V_{in}, must be applied to only one set of electrodes. This constraint results from the fact that it is difficult to split power between several electrodes over large bandwidths with any precision. Any additional networks used to linearize the transfer function cannot have V_{in} as an input; they must be passive networks. This constraint essentially reduces the number of possibilities to three - see Figure 7.1.

The three possibilities use three-port networks to combine both outputs from the coupler into a single linearized output; or to split power between the inputs of the coupler so that the outputs are linear; or to split power between the inputs and combine the outputs so that the final result is linear. Of course, there is no apparent reason to believe *a priori* that any of these networks can

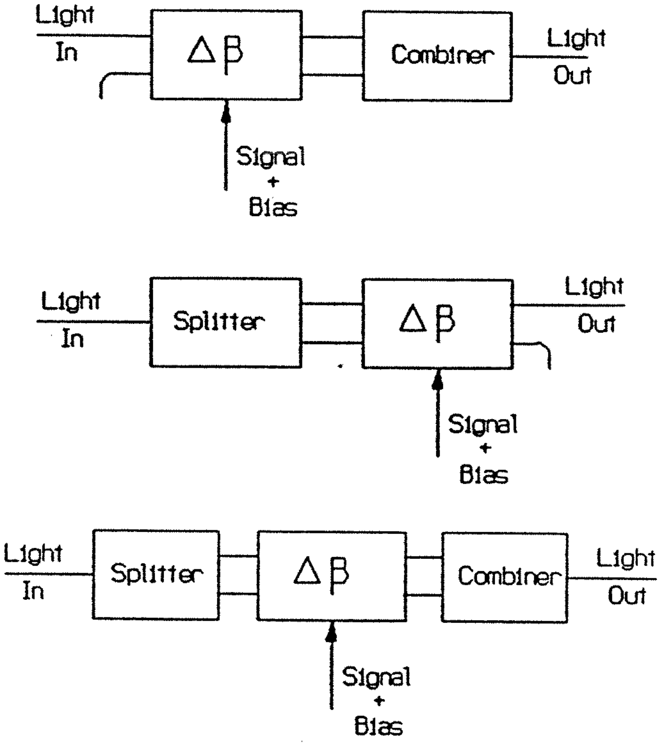

Figure 7.1 Linearization Methods

actually produce a linearized modulator. The approach I will take to this question is simply proof-by-example. It is not easy to understand how the three-port networks linearize the modulator. The reason is that the three-ports operate on the optical fields, while the quantity of interest is the optical intensity. Most people seem to have trouble getting any feel for how to manipulate the fields so that the square of the modulus of the output field is a linear function of the input voltage!

7.3 The Splitter/Combiner Networks

Consider these three-port splitter/combiner networks. Their properties may be represented by S-parameters. In the case of the splitter network we are only interested in S_{21} and S_{31}, where port 1 is the input port and ports 2 and 3 are the output ports. (For practical reasons we would also like to have $S_{11}=S_{22}=S_{33}=0$, because reflections are usually not good in an optical system.)

As an aside here, I should note that we would like these networks to be not only matched, but also reciprocal (because non-reciprocal optical elements are inconvenient) and lossless (because throwing away optical power serves no purpose). Unfortunately there is no such thing as a matched, reciprocal, lossless three-port network. Instead, we will have to consider our three-port to be a matched, reciprocal, lossless four-port network with one port terminated. This termination produces a lossy three-port. In the case of the splitter network it is possible to ensure that no power is dissipated in this termination, but when the network is used as a combiner there will be losses. All will become clear shortly, I hope.

Conservation of energy demands that

$$|S_{21}|^2 + |S_{31}|^2 \leq 1 , \tag{1}$$

so we can write that

$$|S_{21}| = k \text{ Cos } \gamma ,$$
$$|S_{31}| = k \text{ Sin } \gamma , \tag{2}$$

where

$$k^2 \leq 1 . \tag{3}$$

Then the output signals at ports 2 and 3 are

$$b_2 = a_1 \, e^{j\angle S_{21}} \, k \text{ Cos } \gamma ,$$

$$b_3 = a_1 \, e^{j\angle S_{21}} \, e^{j(\angle S_{31} - \angle S_{21})} \, k \text{ Sin } \gamma , \tag{4}$$

where a_1 is the input signal at port 1.

The leading factor $e^{j\angle S_{21}}$ is a phase offset, which we don't care about. The scaling factor k will affect the insertion loss of the modulator but will not affect the shape of its transfer function. So there are two useful degrees of freedom here: γ and $(\angle S_{31} - \angle S_{21})$. We can control these two values independently by cascading a coupler with a differential phase-shifter (Figure 7.2). This cascade of coupler and differential phase-shifter is the general splitter network. Anything we can achieve with any other linear, reciprocal network to linearize the modulator can be achieved with this one. In fact, if it is operated in reverse it becomes a general combiner instead of a splitter, and no other linear, reciprocal combiner network could do any better (although there may be others

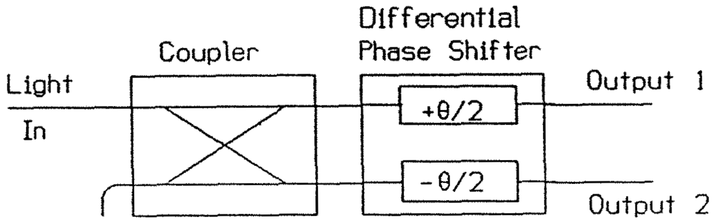

Figure 7.2 Coupler/Phase-Shifter Splitter

which could do equally as well).

It is possible to add at most two degrees of freedom with either a splitter network or a combiner network alone, and it is possible to add at most four degrees of freedom with both a splitter and a combiner network. No cascade of couplers, phase-shifters, or other possible linear reciprocal networks can do any more than this. Consequently we can say that the best linearization possible by cascading such networks with a $\Delta\beta$ coupler modulator can be achieved by cascading the general splitter, $\Delta\beta$ coupler modulator, and general combiner. This simplifies the search for linearization methods by defining and limiting the search space.

Since we have generalized splitter and combiner networks to connect to the inputs and outputs of the $\Delta\beta$ coupler, we can go ahead and define the general linearized $\Delta\beta$ modulator. This is a $\Delta\beta$ coupler with a splitter network connected across its inputs and a combiner network connected across its outputs. There are at most six degrees of freedom in this modulator. They are:

- The coupling angle α which defines the power-split in the splitter-network coupler;

- The phase-angle β of the splitter-network phase-modulator;

- The coupling length κL of the $\Delta\beta$ coupler itself;

- The bias-point V_o of the $\Delta\beta$ coupler;

- The phase-angle ϕ and coupling angle θ of the combiner network.

The design of the modulator is specified by the design vector $\{\alpha, \beta, \kappa L, V_o, \phi, \theta\}$. Note that α=0 eliminates the input splitter, and θ=0 eliminates the output combiner. So $\{0, 0, \kappa L, V_o, 0, 0\}$ represents a basic $\Delta\beta$ modulator of length κL, operated at a normalized bias-point V_o. (The normalization I use here is such that the switching voltage of a modulator with $\kappa L = \pi/2$ would be V=1.) This simple modulator can be operated with the second derivative of its transfer function equal to zero. Various modulators of the form $\{0, 0, \kappa L, V_o, \phi, \theta\}$ have been proposed [1-4], and since these add two degrees of freedom it is, perhaps, not too surprising that it is possible to set the second, third and fourth derivatives to zero simultaneously. It is possible to do the same thing with a modulator of the type $\{\alpha, \beta, \kappa L, V_o, 0, 0\}$, which has a splitter but no combiner network. This is because splitter-only and combiner-only modulators are equivalent to each other by reciprocity.

7.4 Design of a Linearized $\Delta\beta$ Modulator

The design of the modulator can proceed by searching the six-dimensional space for a design vector where the modulator satisfies the design requirements. One or more degrees of freedom may be fixed to reduce the amount of search necessary or for other practical reasons. For example, if the number of sections is to be limited, then a splitter-only or combiner-only design may be used, which sets two of the degrees of freedom to zero. It is also common to set $\kappa L = \pi/2$. The full search would be straightforward, if tedious. I have not done this search, but will give some useful design vectors below.

There is some symmetry which makes the design-points for splitters or combiners equivalent to each other in pairs. If the output ports of a splitter network are re-labeled, the effect is to convert the coupling angle γ to $(\pi/2-\gamma)$, while at the same time converting the phase ϕ to $-\phi$. However, since re-labeling the ports does not change reality, both the points (γ, ϕ) and $(\pi/2-\gamma, -\phi)$ must be equivalent design-points. The coupling angle γ should be specified in the first quadrant (i.e., $0 \leq \gamma \leq \pi/2$) because other quadrants simply amount to changing ϕ to $-\phi$ and back.

7.5 Practical Implementation of the Splitter/Combiner Networks

I have discussed how the modulator may be described in terms of a six-element vector. The middle two elements describe the $\Delta\beta$ coupler, while the first two and last two elements describe the splitter and combiner networks. Assuming, for the present, that some design vector has been decided upon, how can these splitter and combiner networks be implemented?

The splitter/combiner networks may be implemented in the obvious way, using phase-shifters and couplers (Figure 7.3). However this is not the most convenient structure to fabricate. Any bends in the optical waveguide must be very gradual in order to minimize bending losses, so structures which require alternately large and small inter-optical-waveguide spacing become very long. It would be better if the optical waveguide spacing could be kept constant. Since a coupler is required, the spacing would be kept small.

It is possible to get a $\Delta\beta$ coupler to act almost like a phase-shifter. For large

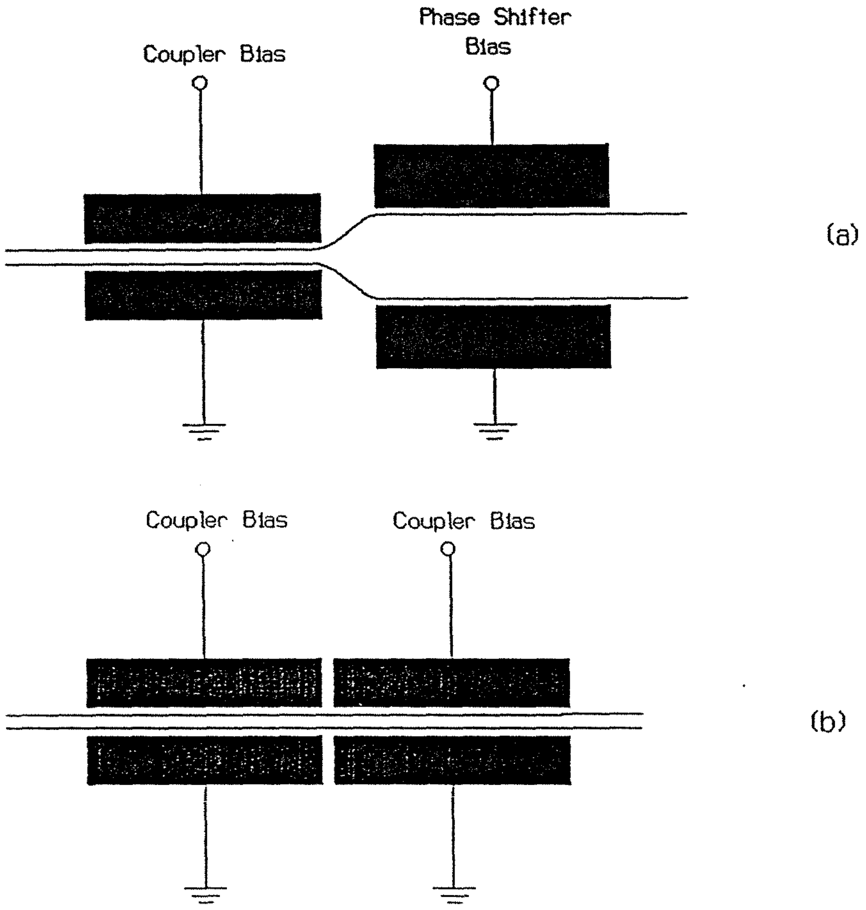

Figure 7.3

Coupler and phase shifter may be implemented directly as hardware (a), but this is inconvenient as the waveguide bends take up a lot of space (they must be much more gradual than this Figure would suggest). Alternatively they may be implemented using two cascaded $\Delta\beta$ couplers (b), which is more compact, but cannot realize every possible phase-amplitude combination.

values of $\Delta\beta$ the coupling factor is small and varies only slightly with $\Delta\beta$. However the output phase depends on $\Delta\beta$ directly. Hence the coupler is similar to a phase-shifter, with only a small amount of crosstalk between the arms. The large value of $\Delta\beta$ may be schieved by using a high bias voltage or by having different waveguide dimensions in the two arms. A second $\Delta\beta$ coupler with its own fixed bias can act as the coupler required for the splitter/combiner (see Figure 7.3b). Since the phase-shifter is no longer ideal, however, there will be regions of $(\gamma,\ \phi)$ space which are not accessible, although these can be made small by appropriate choice of coupler-lengths (Figure 7.4). Analysis of the proposed structure will establish whether the design vector can be achieved, given the limitations of the structure. Remember that design-points for splitters or combiners come in pairs, and one of the points may be accessible while the other is not. If neither point can be reached, either a new design vector or a new structure will be needed.

7.6 Design Examples

I want to consider a few design examples to illustrate how linearized modulators can be designed and realized. I have not undertaken an exhaustive search of the entire six-dimensional design vector space, but instead will use specific design vectors as an illustration of what can be done. Undoubtedly there are other useful design vectors which are even more linear than any of these. I have limited my search to modulators where $\kappa L = \pi/2$. I have been able to find design vectors which give considerable improvements in linearity where either a splitter or combiner is used alone. To date I have not found the best conditions for the more general splitter-coupler-combiner modulator, but I have found approximate conditions which suggest that quite impressive performance

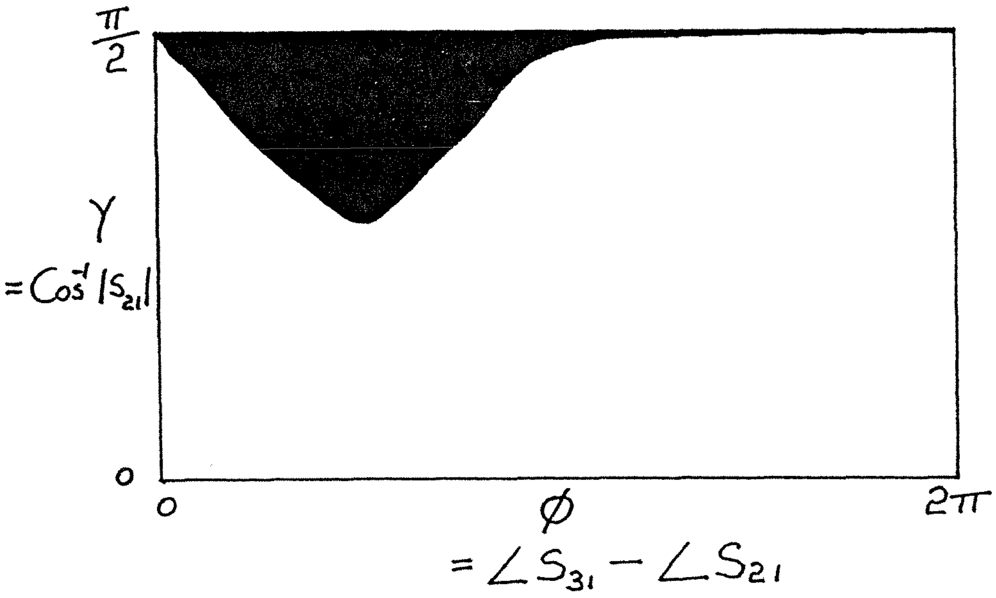

Figure 7.4 Implementing the Splitter/Combiner Network

The dark area shows the region of (γ,ϕ) space which cannot be reached if the splitter is implemented using two cascaded $\lambda/4$ $\Delta\beta$ couplers, and the bias-voltages used are limited to $|V\text{bias}| \leqslant 2\ V\text{o}$. If the first coupler's length is increased to $\lambda/2$, most of (γ,ϕ) space can be reached except for thin strips near $\gamma = 0$ and $\gamma = \pi/2$.

Note that $\gamma = \text{Cos}^{-1}|S21|$ and $\phi = \angle S31 - \angle S21$.

is possible.

First consider the basic $\pi/2$ $\Delta\beta$ coupler-modulator with neither a splitter nor a combiner. For the sake of brevity I refer to this as a Class 0 (zero) modulator. The design vector for this modulator is $\{0, 0, \pi/2, V_o, 0, 0\}$. V_o represents the only degree of freedom. The obvious value to choose for V_o is the one which biases the modulator to the inflection-point of its transfer-function. This is the vector $\{0, 0, \pi/2, 0.43936, 0, 0\}$. At this point there are no second-order products, but there are third- and higher-order products. Note that there will be second-harmonic content in the output even though the second derivative of the transfer-function is zero, because nonzero fourth, sixth and higher even-order derivatives of the transfer-function give rise to second-harmonic outputs. Figure 7.5 shows the calculated performance of this modulator. The method of calculation used to produce this result, and the other results presented here, is explained in Appendix E.

Next consider trying to improve on this performance by adding either a splitter or a combiner (remember, these are equivalent by reciprocity). I refer to these as Class 1 modulators. This class of modulators includes those mentioned previously, proposed by Chang and coworkers [2,3] and by Lam and Tangonan [4]. There is more than one design vector for this class of modulator which gives improved linearity. One such point is $\{0, 0, \pi/2, 0.508929, 1.31156, 0.327598\}$. The necessary combiner network can be made by cascading two fixed-bias $\Delta\beta$ couplers of length $\kappa L = \pi/4$, with their normalized bias-points set to 0.73826, 0.77022. This example is mentioned in [1] on page 42 as the "UCSD modulator," based on [2] and [3]. This modulator is markedly more linear than

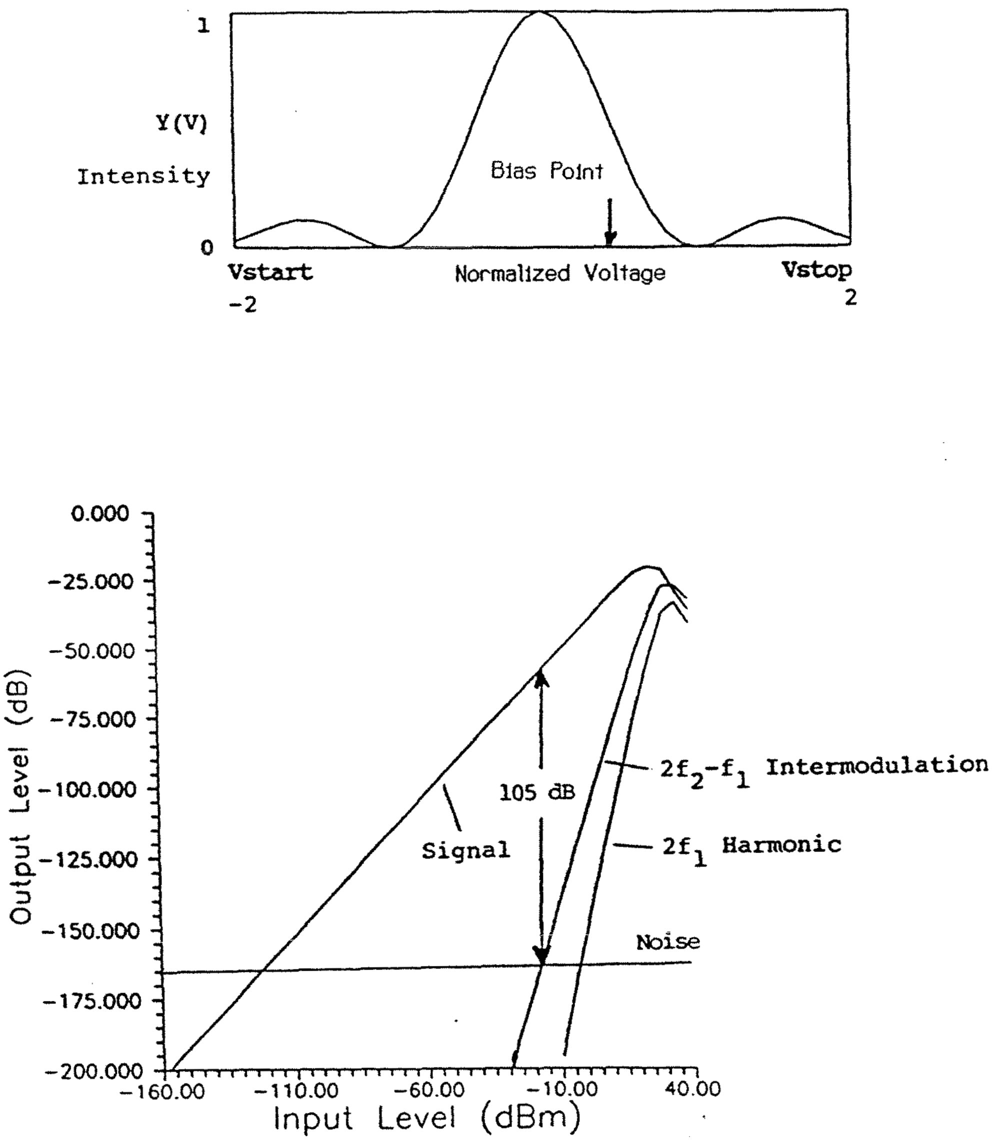

Figure 7.5 Class 0 (Unmodified) Modulator Transfer Function & Dynamic Range

the basic $\Delta\beta$ coupler-modulator, with a dynamic range improvement of 15-20 dB in a typical system. Figure 7.6 shows the transfer function and the calculated performance of this Class 1 modulator.

I believe it is possible to gain further performance improvements by using both a splitter and a combiner network to produce a Class 2 modulator. To date I have not found design vectors which significantly improve the dynamic range of a typical system over that of the Class 1 modulator above, but I have found one which is nearly linear over a wide range (Figure 7.7). This modulator has the design vector $\{0.3314,\ 1.6266,\ \pi/2,\ 0.5725,\ 2.3735,\ 0.2264\}$ approximately. Unfortunately, while the second derivative is zero and the third through sixth derivatives are all small, I have not found a design vector which makes them all simultaneously zero, and consequently there are residual nonlinearities which produce unwanted frequency components. The result is that although this modulator has smaller-amplitude intermodulation products than the Class 1 modulator at high signal levels, the intermodulation is worse at low signal levels, resulting in a smaller dynamic range. However, there may well be a design vector which does, in fact, set all these derivatives to zero simultaneously, giving a further improvement in dynamic range. I have also found a Class 2 modulator which has similar performance to the Class 1 modulator example I gave above, and which can be realized using only two additional $\Delta\beta$ couplers, one across the modulator input and one across the output ports. These couplers are of length $\kappa L = \pi/2$, and are biased respectively to 0.72809 and 1.17391. This corresponds to the design vector $\{0.3658,\ -2.5552,\ \pi/2,\ 0.44,\ 2.7900,\ 0.1800\}$. This design is also reported on page 46 of [1], as the "Caltech type" modulator.

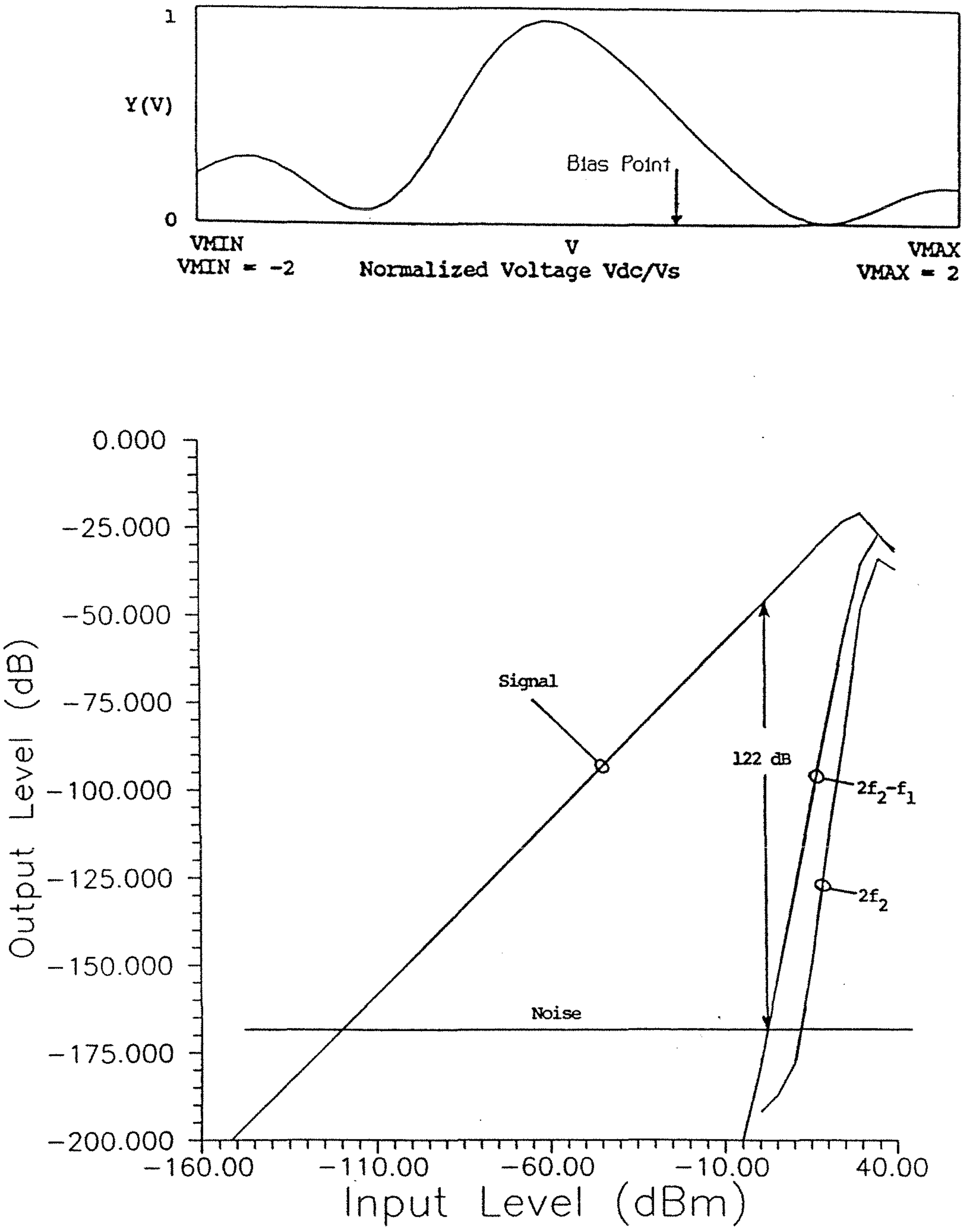

Figure 7.6 Class 1 Modulator

Transfer Function and Dynamic Range

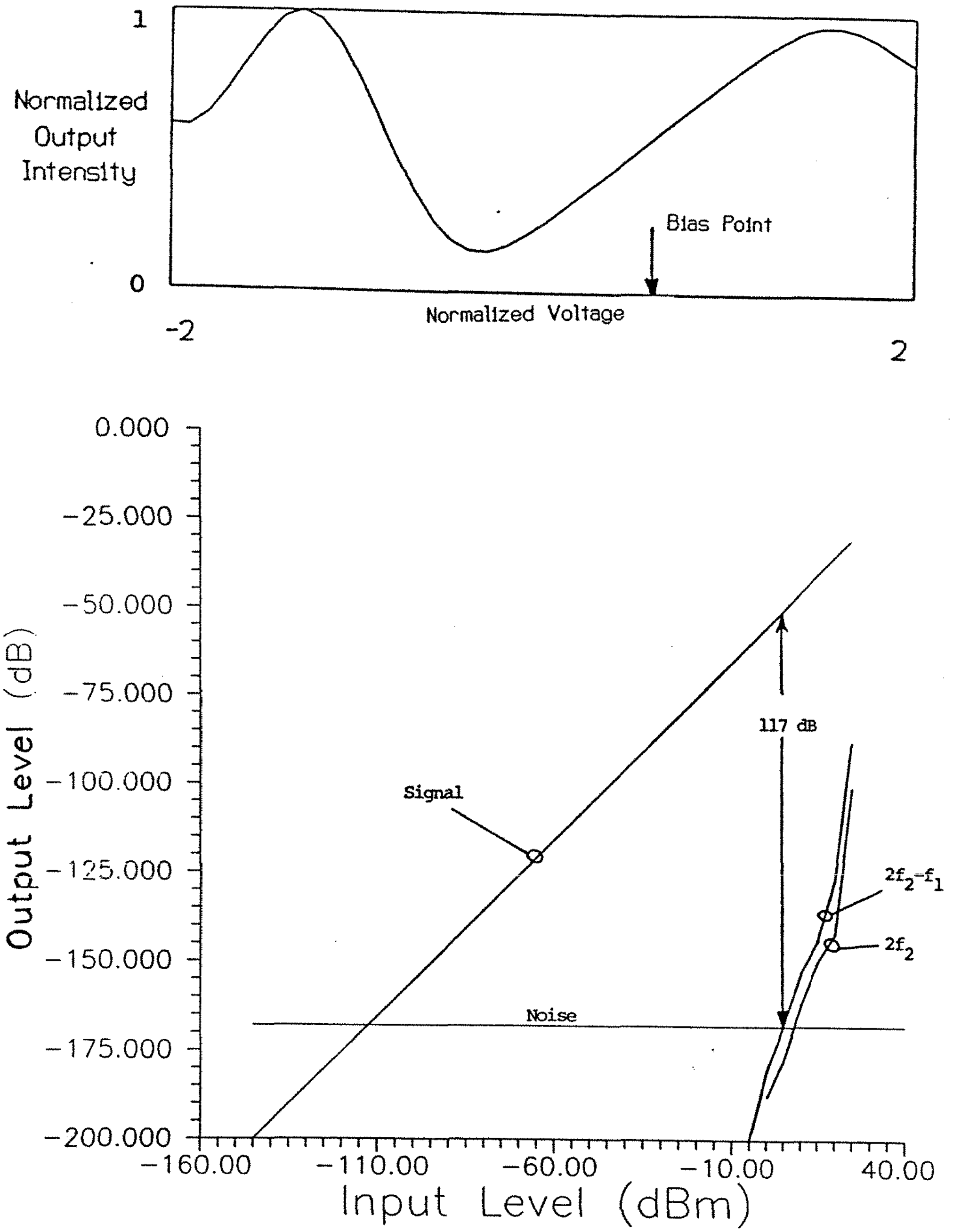

Figure 7.7 Class 2 Modulator (Example) Transfer Function and Dynamic Range

This example has not been fully optimized. It may be possible to improve dynamic range to 125 - 130 dB by optimizing a Class 2 modulator.

7.7 Conclusion

External electro-optic modulators may be limited in their applications by their nonlinear transfer-functions. It is possible, however, to modify a $\Delta\beta$ coupler-modulator by cascading it with a splitter network across its optical input ports and/or a combiner network across its output ports. These networks add at most four degrees of freedom which can be used to modify the transfer function of the modulator. If these networks are properly designed the transfer function of the modified modulator may be made significantly more linear. I have shown that a phase-shifter and a coupler are all that is required to realize either of these networks, and have discussed how the networks can be implemented in practice. I have shown some examples of linearized modulator designs to illustrate the concepts.

References

[1] J. Schaffner, W. Bridges, C. Gaeta, R. Hayes, G. Tangonan, R. Joyce, and J. Lewis, "High Fidelity Microwave Remoting," Final Report to USAF Rome Laboratory, Contract No. F30602-91-C-0104, Hughes Ref. No. J4373, November 1992

[2] Zong-Qi Lin and William S.C. Chang, "Waveguide Modulators with Extended Linear Dynamic Range - A Theoretical Prediction," IEEE Photonics Tech. Lett., Vol. 2, December 1990, pp. 884 - 886

[3] Mark L. Farwell, Zong-Qi Lin, Ed Wooten, and William S.C. Chang, "An Electrooptic Intensity Modulator with Improved Linearity," IEEE Photonics

Tech. Lett., Vol. 3, September 1991, pp. 792 - 795

[4] Juan F. Lam and Gregory L. Tangonan, "A Novel Optical Modulator System with Enhanced Linearization Properties," IEEE Photonics Tech. Lett., Vol. 3, December 1991, pp. 1102 - 1104

8. Comparison of mm-Wave Electro-Optic Transmission Systems

8.1 Introduction

Our project considered the development of mm-wave electro-optic modulators as transmitter elements. We assumed that someone else would, in time, produce a high-frequency photodiode which would make it possible to build the corresponding receiver. So far this has not happened. It is interesting to consider how such a photodiode would be used, however. The detected signal would be a mm-wave signal, and in most applications the user would down-convert this signal to a lower frequency, the intermediate frequency (IF). Hence the photodiode would be a high-frequency diode, used to convert the signal from the optical to the electrical domain. A second high-frequency diode would then be needed for the mm-wave mixer.

There is another way to build this receiver. If we pass the incoming optical signal through a second modulator, and drive this modulator with the local oscillator signal (LO), then the output of this modulator will have a low-frequency modulation corresponding to the desired IF. This signal can be applied to a low-frequency photodiode, and the output of this photodiode will be the IF. This requires a minimum of mm-wave circuitry (only the LO circuit), since the conversion to the electrical domain occurs at the IF. Further, if it is possible to build the transmitter, it must be possible to build the receiver, since the required components are the same.

There is yet another potentially useful configuration using a similar approach. This configuration is suggested by a paper by Kolner and Dolfi [1] in which the electro-optic modulator is proposed as a broadband mixer. Essentially the configuration is the same as the previous one, but the optical signal is modulated first with the LO, then with the RF input. I propose that the mm-wave signal should be applied directly to an electro-optic modulator, but that the optical input signal for the modulator should be supplied by a mode-locked semiconductor laser, where the mode-locking frequency would be the LO frequency. The laser could be at the user's location, with its output conveyed to the remote location by a fiber, or could be at the remote location. Such lasers have been demonstrated at mode-locked frequencies up to 130 GHz [2]. Such a laser could provide a simple and rugged LO source, although such lasers are not yet mature. At the user end, the incoming optical signal is detected with a low-frequency photodiode, which need pass only the IF.

Various workers have proposed distributing reference frequency and phase information, for example to the various elements of a phased array, using optical transmission. The electro-optic mixer may be of use here also. To take a concrete example, suppose that each element of the phased array is equipped with an oscillator to provide power for transmission, and a phase-locked-loop to lock this oscillator to the reference. Instead of detecting the reference signal with a high-frequency photodiode, then using a mm-wave mixer as a phase detector, we can consider using an electro-optic modulator as a mixer, which means that only a low-frequency photodiode is required to detect the difference frequency.

Of course, another, more conventional approach is also of interest. This is the idea of putting a mm-wave receiver at the transmit end, transmitting only the

IF.

This chapter is a study of the relative merits of the various approaches, particularly from the point of view of gain, noise performance, and intermodulation distortion. I will also mention some practical considerations.

8.2 Performance of System Components

In this section I will analyse the various components which can be combined to make a system.

8.2.1 Modulator Performance

The modulator converts an input voltage V_{in} ($=V_{rf} + V_{bias}$) to an output light intensity $\mathbf{I}_{out}$ according to the relationship

$$\mathbf{I}_{out} = \mathbf{I}_o \left(1 + \mathrm{Cos}\left(\pi V_{in}/V_\pi\right)\right), \tag{1a}$$

where we note that the maximum possible output intensity is 2 $\mathbf{I}_o$. Rewriting in terms of V_{rf} and V_{bias},

$$\mathbf{I}_{out} = \mathbf{I}_o \left(1 + \mathrm{Cos}\left(\pi (V_{rf} + V_{bias})/V_\pi\right)\right). \tag{1b}$$

If we set $V_{bias} = V_\pi/2$, as is usual, this is equal to

$$\mathbf{I}_{out} = \mathbf{I}_o \left(1 - \mathrm{Sin}\left(\pi V_{rf}/V_\pi\right)\right). \tag{1c}$$

The reason I chose to set the maximum possible output intensity from the modulator to 2 I_o was that I_o is now the output intensity at the chosen bias-point. Clearly there is a small-signal transfer function here which is

$$\frac{dI_{out}}{dV_{rf}} = -\ I_o\ \frac{\pi\, V_{rf}}{V_\pi}\ . \tag{2}$$

Hence the modulation index, m, which results from the modulation process, is given by

$$m = \frac{\pi\, V_{rf}}{V_\pi}\ . \tag{3}$$

Assuming a sinusoidal input, the input signal power is

$$P_{in} = \frac{V_{rf}^{\ 2}}{2\ R}\ , \tag{4}$$

where R, the modulator input impedance, depends on the modulator structure. Combining these results gives

$$\frac{m^2}{P_{in}} = 2\ R \left(\frac{\pi}{V_\pi}\right)^2 . \tag{5}$$

We will denote the modulator gain as

$$G_{mod} = \frac{m^2}{P_{in}}\ . \tag{6}$$

The intermodulation distortion due to the modulator can be described in the conventional way, by considering its third-order intermodulation intercept, evaluated by extension of small-signal behavior. This need not be the actual third-order intercept. I want to depart from the usual by specifying the input intercept, rather than the output intercept. The input intercept is the input power for each of two tones which would produce an output third-order product equal in amplitude to the signal outputs, if there were no saturation in the device.

Recall equation (1c) and substitute a two-tone input for the voltage V_{rf}, as

$$V_{rf} = V_t \left(\mathrm{Cos}(\omega_1 t) + \mathrm{Cos}(\omega_2 t)\right), \tag{7}$$

so that

$$\mathbf{I}_{out} = \mathbf{I}_o \left(1 - \mathrm{Sin}\left\{\frac{\pi V_t}{V_\pi}\left(\mathrm{Cos}(\omega_1 t) + \mathrm{Cos}(\omega_2 t)\right)\right\}\right). \tag{8}$$

Now write

$$Q = \frac{\pi V_t}{V_\pi}, \tag{9}$$

and consider only small-signal components:

$$\frac{-\mathbf{I}_{out}}{\mathbf{I}_o} = \mathrm{Sin}\left(Q\ \mathrm{Cos}(\omega_1 t)\right) \mathrm{Cos}\left(Q\ \mathrm{Cos}(\omega_2 t)\right) + \mathrm{Cos}\left(Q\ \mathrm{Cos}(\omega_1 t)\right) \mathrm{Sin}\left(Q\ \mathrm{Cos}(\omega_2 t)\right) \tag{10}$$

$$= 2\sum_{m=0}^{\infty} (-)^m \mathbf{J}_{2m+1}(Q)\ \mathrm{Cos}\left\{(2m+1)\omega_1 t\right\}\left\{\mathbf{J}_o(Q) + 2\sum_{n=1}^{\infty} (-)^n \mathbf{J}_{2n}(Q)\ \mathrm{Cos}\left\{2n\omega_2 t\right\}\right\}$$
$$+ 2\sum_{n=0}^{\infty} (-)^n \mathbf{J}_{2n+1}(Q)\ \mathrm{Cos}\left\{(2n+1)\omega_2 t\right\}\left\{\mathbf{J}_o(Q) + 2\sum_{m=1}^{\infty} (-)^m \mathbf{J}_{2m}(Q)\ \mathrm{Cos}\left\{2m\omega_1 t\right\}\right\} \tag{11}$$

The third-order intermodulation products come from terms like

$$-2\, \mathbf{J}_1(Q)\, \mathbf{J}_2(Q)\, \mathrm{Cos}\left\{(2\omega_2 - \omega_1)\, t\right\} . \tag{12}$$

The signal outputs are of the form

$$2\, \mathbf{J}_o(Q)\, \mathbf{J}_1(Q)\, \mathrm{Cos}(\omega_1 t) , \tag{13}$$

so the ratio of third-order intermodulation products (IMP) to the signal (S) is

$$-\mathbf{J}_2(Q) \,/\, \mathbf{J}_o(Q) . \tag{14}$$

For small arguments, $\mathbf{J}_o(Q) = 1$, and $\mathbf{J}_2(Q) = \frac{Q^2}{8}$, so for small arguments the ratio IMP/S is given by

$$\frac{\mathrm{IMP}}{\mathrm{S}} = -\frac{Q^2}{8} . \tag{15}$$

The intermodulation intercept, as I have defined it, occurs when $Q = 2\sqrt{2}$. But Q is formally the same as m, the modulation index (the difference is due to the existence of two tones), and we know the relationship of m to the input power. Using equations (3)-(6), this defines the point at which the third-order intercept occurs :

$$P_{IM} = \frac{8}{G_{mod}} , \tag{16}$$

which is equivalent to the statement

$$V_{t_{IM}} = \frac{2\sqrt{2}\,V_\pi}{\pi}\,, \tag{17}$$

and in fact this result was previously derived by Kolner and Dolfi in [1], using slightly different notation in the derivation.

8.2.2 Detector Performance

The detector is a reverse-biased diode. Photocarriers resulting from illumination by the optical signal give rise to a current which depends linearly on the illumination intensity. Since the reverse-biased p-i-n junction has a very high resistance, the impedance of the detector is dominated by the diode and (especially) package capacitances and lead inductance. Once these are fixed, the cutoff frequency is determined by the load impedance.

The current out of such a detector is given by

$$i_s = \frac{e\,\eta}{h\,\nu}\,\mathbf{I}_{\boldsymbol{opt}}\,, \tag{18}$$

where the quantity $\frac{e\,\eta}{h\,\nu}$ is called the Responsivity of the detector (A/W).

If we assume a 50 Ω load, this gives the detector gain:

$$G_{det} = \frac{P_{det}}{\mathbf{I}_{\boldsymbol{opt}}^{\,2}} = \frac{50\,\overline{i_s^{\,2}}}{\mathbf{I}_{\boldsymbol{opt}}} = 25\left(\frac{e\,\eta}{h\,\nu}\right)^2. \tag{19}$$

The detector contributes to noise because of its shot noise:

$$\overline{i_n^2} = 2\, e\, \overline{i}\, B\,. \qquad (20)$$

But of course the mean current in the detector, $\overline{i}$, is related to the mean optical intensity by:

$$\overline{i} = \frac{e\,\eta}{h\,\nu}\, I_o\,, \qquad (22)$$

and the noise power delivered to a 50 Ω load is simply 50 $\overline{i_n^2}$, giving the result

$$P_n = 100\, \frac{\eta\, e^2\, B}{h\,\nu}\, I_o\,. \qquad (23)$$

I will also refer to the detector effective input noise temperature, which is $T_{det}=P_n/\left(k\ G_{det}\right)$.

8.2.3 Diode Mixer Performance

I will not get into the theory of diode mixers, but will simply say that the typical single-ended whisker-contacted 100 GHz Schottky-barrier diode mixer is characterized by the following numbers:

$$\text{Gain} = \text{-7 dB} \qquad (24)$$

$$\text{Input Noise Temperature} = 1800\ \text{K} \qquad (25)$$

$$\text{Input } 3^{rd} \text{ Order Intercept} = P_{LO} \qquad (26)$$

where P_{LO} is typically 1-5 mW (i.e., 0-7 dBm).

8.2.4 Electro-Optic Mixer Performance

We have not quite got enough information above to analyse the performance of an electro-optic mixer. An electro-optic mixer multiplies two signals in the optical domain, using two electro-optic modulators. The input optical signal is multiplied by the first electrical signal in the first modulator. This modulated optical signal is applied to the second modulator where it is multiplied in turn by the second electrical signal. Finally the optical signal must be converted back into the electrical domain by a detector. The mixer thus has three parts: two modulators (one for the signal, one for the local oscillator) and a detector. We have analysed the performance of the signal modulator and the detector, but not the performance of the local oscillator (LO) modulator. It is this second modulator which, in the second multiplication process, results in the conversion of power from the signal frequency to the intermediate frequency (IF).

If the optical input to this modulator is modulated by a tone at ω_1, with modulation depth m, and the electrical input to the modulation port is a tone at the LO frequency ω_o, producing modulation depth m_o, then the output is in the form

$$\mathbf{I}_{out} = \mathbf{I}_o \Big(1 + \mathrm{m}\cos(\omega_1 t)\Big)\Big(1 + \sin\Big\{\mathrm{m}_o \cos(\omega_o t)\Big\}\Big) . \qquad (27)$$

Retaining only the relevant term in the output, at the IF,

$$\mathbf{I}_{IF} = \mathbf{I}_o\, \mathrm{m}\, \mathbf{J}_1(\mathrm{m}_o) . \qquad (28)$$

For small LO drive powers, $J_1(m_o) = m_o/2$, so the total gain is $\frac{1}{4}\, m^2\, m_o^2$, but part of this results from the modulator gain (m^2), so I will use the term "mixer gain" to denote the additional term $m_o^2/4$. Then, substituting for m_0,

$$G_{eox} = \frac{1}{4}\, G_{LOmod}\, P_{LO}\ . \tag{29}$$

For large LO powers, the quantity $\mathbf{J_1}$ has a maximum value of 0.5815 at m_o = 1.8, so

$$G_{eox}\ \leq\ 0.5815^2\ . \tag{30}$$

8.3 Analysis of System Performance

Each of a number of systems will be analysed to establish its performance in terms of gain, noise performance (minimum detectable signal), and dynamic range.

8.3.1 Performance of Conventional Modulate-Detect-Mix System

This is the analysis of the "conventional" system (Figure 8.1) where the signal is first modulated onto an optical carrier, transmitted, detected by a high-speed photodiode, then mixed down to IF by a conventional mm-wave receiver.

The gain of this system is

$$G_{con}= \mathbf{I_o}^2\ G_{mod}\ G_{det}\ G_{mxr}\ , \tag{31}$$

where $\mathbf{I_o}$ is the optical intensity incident on the detector. We can evaluate this

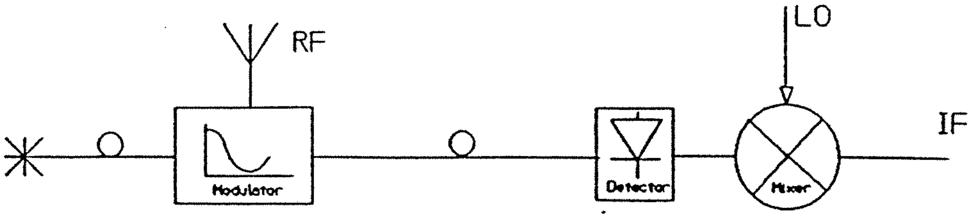

Figure 8.1 Modulate - Detect - Mix

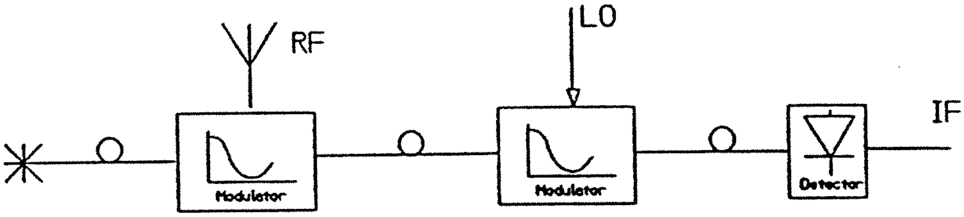

Figure 8.2 Modulate - Mix - Detect

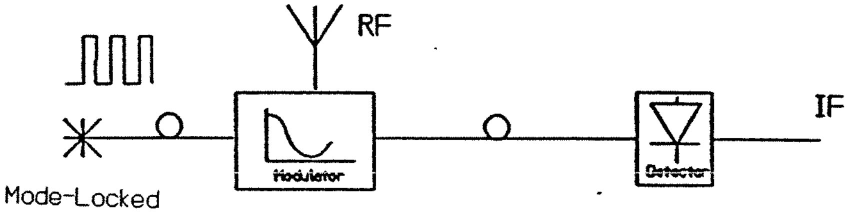

Figure 8.3 Mode-Locked

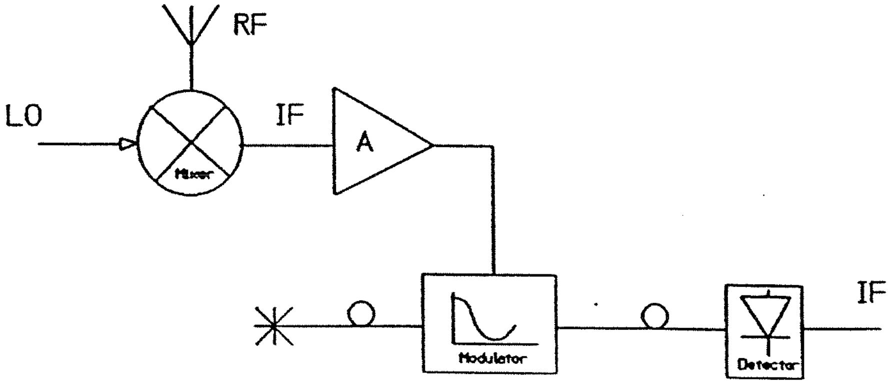

Figure 8.4 Mix - Amplify - Modulate - Detect

expression if we now make the following assumptions:

$\mathbf{I_o}$ = 5 mW, limited by the survival of the hypothetical
but necessarily small 94 GHz photodetector;
G_{mod} = 0.1 which is a bit more than we achieved at 94 GHz;
η = 0.2 for a hypothetical high-frequency detector;
G_{mxr} = 0.2 which is typical for a mm-wave mixer at 100 GHz;
$\frac{e}{h\,\nu}$ = 1 for a 1.3 μm system;

then

$$G_{sys} = 0.005^2 \text{ x } 0.1 \text{ x } 25 \text{ x } 0.2^2 \text{ x } 0.2 = 5 \text{ x } 10^{-7} = \text{-63 dB} . \tag{32}$$

There are two sources of noise in this system, one being the shot noise in the photodiode and the other being the mixer noise. The mixer input impedance is relevant here, but for the sake of argument I will assume 50 Ω. The expression for the input noise temperature of a cascade of noisy gain elements is

$$T = T_1 + T_2/G_1 + T_3/G_1G_2 \,.\,.\,.\,.\,. \tag{33}$$

In this case the noise temperature of the photodiode may be taken as the noise power it delivers to its load in a 1-Hz bandwidth divided by Boltzman's constant k and the detector gain, i.e.,

$$T_{det} = \frac{100\,\eta\,e^2}{h\,\nu\,k}\,I_o\left(\frac{h\,\nu}{e\,\eta}\right)^2\frac{1}{25} = \frac{4\,h\,\nu\,I_o}{\eta\,k}\,, \tag{34}$$

so then equation (33) becomes

$$\mathrm{T}_{sys} = \left(\frac{4\,\mathrm{h}\,\nu}{\eta\,\mathrm{k}}\,\mathrm{I}_o + \frac{1800}{25\left(\frac{\mathrm{e}\,\eta}{\mathrm{h}\,\nu}\right)^2} \right) \frac{1}{\mathrm{I}_o^{\,2}\,\mathrm{G}_{mod}} \ . \tag{35}$$

The minimum detectable signal is then $\mathrm{mI}_o = \mathrm{kT}_{sys}$.

Using the same assumptions as before, we get

$$\mathrm{T}_{sys} = 1.2\ \mathrm{GK}\ , \tag{36}$$

$$\mathrm{S}_{min} = \text{-}108\ \mathrm{dBm}\ . \tag{37}$$

As for intermodulation distortion, this would be specified for an optical carrier modulated with two tones of similar frequency and the same amplitude. The photodiode, being linear or very nearly so, introduces essentially no distortion. The mixer, however, is nonlinear, and will introduce distortion. The third-order intermodulation intercept can be referred back to the input of the modulator by

$$\mathrm{IMD} = \mathrm{IMD}_{mxr}\ /\ \left(\mathrm{I}_o^{\,2}\ \mathrm{G}_{mod}\mathrm{G}_{det}\right)\ , \tag{38}$$

so we have

$$\mathrm{IMD} = \frac{\mathrm{P}_{LO}}{\mathrm{I}_o^{\,2}\ \mathrm{G}_{mod}\ 25\left(\frac{\mathrm{e}\,\eta}{\mathrm{h}\,\nu}\right)^2}\ , \tag{39}$$

which, for a 5 mW LO, is 63 dBm. This is not important compared to the intermodulation intercept of the modulator itself. Recall that its intercept is at $8/\mathrm{G}_{mod}$, which is 49 dBm. Hence the dynamic range of this system is 105 dB.

8.3.2 Modulate-Mix-Detect System

This is a possible alternative to the system described above. Here (Figure 8.2) an electro-optic mixer is used, either at the receive or transmit end, to convert the signal information to an IF, with the signal-processing performed in the optical domain. The photodiode need not be a high-frequency diode, because it detects the IF.

For this system, $$\text{Gain} = \mathbf{I}_o^2\ \text{G}_{mod}\ \text{G}_{eox}\ \text{G}_{det}\ . \tag{40}$$

Now I need to make assumptions again. Initially I will use these:

$\mathbf{I}_o$ = 50 mW because the detector is a large, low-frequency detector;

G_{mod} = 0.1 again, because it is the same one;

G_{LOmod} = 0.1 because it is the same as the modulator;

η=0.5 for the large photodiode;

P_{LO} = 5 mW for comparison with the previous system;

$$\text{G}_{sys} = 0.05^2 \text{ x } 0.1 \text{ x } \frac{0.1}{4} \text{ x } 0.005 \text{ x } 25 \text{ x } 0.5^2\ , \tag{41}$$

$$= 1.95 \text{ x } 10^{-7} = -\ 67 \text{ dB}\ , \tag{42}$$

which is about the same as the previous system.

The noise now comes from the detector shot-noise, so

$$\text{T}_{sys} = \text{T}_{det}\ /(\text{G}_{eox}\ \text{G}_{mod})\ , \tag{43}$$

$$= \left(\frac{4\,h\,\nu}{\eta\,k}\, I_o \right) / \left\{ \left(\frac{P_{LO}}{4}\, G_{LOmod} \right) \left(G_{mod}\, I_o^{\,2} \right) \right\} , \tag{44}$$

$$= 4400 \;/\; \left\{ 0.000125 \text{ x } 0.00025 \right\} = 1.4 \text{ x } 10^{11}\ \mathrm{K}\ , \tag{45}$$

$$T_{sys} = 1.4 \text{ x } 10^{11}\ \mathrm{K}\ , \tag{46}$$

which is very high. The reason the shot noise has become so serious even though the system gain is about the same is that the shot-noise is now preceded by the mixer loss, instead of coming before it. The mixer loss thus effectively "amplifies" the shot noise when referred back to the system input. This has very serious impact on the minimum detectable signal:

$$S_{min} = \text{-87 dBm}\ . \tag{47}$$

In this system the only contribution to intermodulation comes from the modulator itself, so we know at once that the third-order intercept occurs at 49 dBm, giving

$$\text{Dynamic Range} = 91\ \text{dB}\ . \tag{48}$$

8.3.3 Modulate-Mix-Detect with Mode-Locked Laser

In the above analysis I assumed a two-modulator mixer with an external LO. However, there is another possibility (Figure 8.3). Suppose the laser is mode-locked at the LO frequency. This dramatically improves the electro-optic mixer performance. The expression for G_{eox} now becomes equal to 0.5815^2 (at best-case), so that the analysis changes as follows:

$$\text{Gain} = \mathbf{I_o}^2\ \text{G}_{mod}\ \text{G}_{eox}\ \text{G}_{det}\ ,$$

$$= 0.025^2 \text{ x } 0.1 \text{ x } 0.5815^2 \text{ x } 25 \text{ x } 0.5^2 = 2.3 \text{ x } 10^{-4}\ , \qquad (49)$$

$$\text{G}_{sys} = \text{-36 dB}\ , \qquad (50)$$

which is actually pretty good. Note that I've assumed 25 mW of optical power at the detector, to allow for the somewhat lower output power of the mode-locked laser. The noise analysis changes also, of course:

$$\text{T}_{sys} = \left(\frac{4\ \text{h}\ \nu}{\eta\ \text{k}}\ \mathbf{I_o} \right) / \left\{ \left(\text{G}_{eox} \right) \left(\text{G}_{mod}\ \mathbf{I_o}^2 \right) \right\}, \qquad (51)$$

$$= 2200\ /\ \left\{ 0.5815^2 \text{x} 0.1 \text{x} 0.025^2 \right\} = 1.04 \text{ x } 10^8\ ,$$

$$\text{T}_{sys} = 1.04 \text{ x } 10^8 \text{ K}\ , \qquad (52)$$

which is the best so far. The minimum detectable signal is now

$$\text{S}_{min} = \text{-118 dBm}\ . \qquad (53)$$

The intermodulation intercept is unchanged at 49 dBm, so that:

$$\text{Dynamic Range} = 112 \text{ dB}\ . \qquad (54)$$

8.3.4 Mix-Amplify-Modulate-Detect System

The final system I will analyse is one in which the mm-wave input is mixed down to IF at once, then amplified at the IF before being modulated onto an optical carrier for transmission (Figure 8.4). The detector is a low-frequency detector, required to detect the IF.

$$\text{Gain} = G_{mxr}\ A\ I_o^2\ G_{mod}\ G_{det}\ , \tag{55}$$

where now A is the gain of the IF amplifier. I will analyse the system for two values of A: one value will be 30 dB and the other 0 dB (i.e., no amplifier). The values computed for the 0 dB case will be noted in parentheses like this:

{ } .

The assumptions in this analysis are:

$G_{mxr} = 0.2$ which is typical for a 100 GHz mixer;

$A = 1000\ \{1\}$ as stated above;

$I_o = 50$ mW because the photodiode can take it;

$G_{mod} = 6$ for a low-frequency modulator (35 Ω, $V_\pi = 10$ V);

$\eta = 0.5$ for the low-frequency photodiode;

$T_{mxr} = 1800$ K which is typical;

$T_A = 70$ K which is typical;

$$G_{sys} = 0.2 \text{ x } 1000\ \{1\} \text{ x } 0.05^2 \text{ x } 6 \text{ x } 25 \text{ x } 0.5^2 = 18.75\ \{0.01875\}\ , \tag{56}$$

$$G_{sys} = 13 \text{ dB } \{\text{-}17 \text{ dB}\}\ , \tag{57}$$

which is clearly excellent performance.

The noise analysis takes the form:

$$T_{sys} = T_{mxr} + \frac{T_A}{G_{mxr}} + \frac{T_{det}}{G_{mod}\ A\ G_{mxr}}\ , \tag{58}$$

$$= 1800 + \frac{70}{0.2} + \frac{4400}{6 \text{ x } 1000\ \{1\} \text{ x } 0.2}\ ,$$

$$T_{sys} = 1800 + 350 + 3.5\ \{3650\}\ ,$$

$$T_{sys} = 2150\ \{5800\}\ . \tag{59}$$

This is very good performance compared to anything we've seen before. The minimum detectable signal is, consequently, very low.

$$S_{min} = \text{-165 dBm}\ \ \{\text{-161 dBm}\}\ . \tag{60}$$

The intermodulation in this system comes from the mixer, amplifier and modulator. The mixer intercept is at about the same level as the LO drive, i.e., about 5 dBm. The amplifier intercept is at about 22 dBm when referred back to the mixer input. The modulator intercept is

$$IM_{ref} = \frac{8}{G_{mod}\ A\ G_{mxr}}\ , \tag{61}$$

$$= \frac{8}{6 \text{ x } 1000\ \{1\} \text{ x } 0.2} = 8 \text{ dBm}\ \{38 \text{ dBm}\}\ , \tag{62}$$

which is somewhat higher than the mixer intercept. This is because I chose the IF amplifier gain to make everything after the amplifier more or less unimportant from both noise and intermodulation standpoints. Hence the third-order intercept is 4 dBm (the parallel result of the mixer and modulator intercepts) so that:

$$\text{Dynamic Range} = 112 \text{ dB } \{110 \text{ dB}\} \ . \tag{63}$$

8.3.5 System Performance Summary

In the table below the noise temperature is quoted as noise figure, because the temperatures are so large. The noise figure is $F = 1+T_{sys}/290$, expressed in dB.

System	Gain	Noise Figure	S_{min}	Dyn. Range
Mod-Det-Mix	-63 dB	66 dB	-108 dBm	105 dB
Mod-Mix-Det	-67 dB	87 dB	-87 dBm	91 dB
Mode Locked	-36 dB	56 dB	-118 dBm	112 dB
Mix-Amp-Mod	13 dB	9.2 dB	-165 dBm	112 dB
Mix-Mod-Det	-17 dB	13 dB	-161 dBm	110 dB

8.4 Practical Considerations

Of the above systems, the clear performance winner for almost all real applications is the mix-amplify-modulate system analysed in section 3.4. The mode-locked system in 3.3 has a large dynamic range, but at such high power levels as to have no practical usefulness over much of that range.

However, performance may not be the only criterion. The mix-amplify-modulate system has a mm-wave mixer at the transmit end of the link, which may be unacceptable. For example, remotely-located sensors may need to be rugged and/or cheap, which these mixers are not. The user may wish to have the local oscillators phase-locked to each other, which is a difficult thing to arrange (although not impossible - the reference may be sent via fiber - see below), and so may prefer to have the mixing performed at the receive end. In this case it is probably preferable to use the modulate-detect-mix system in section 3.1.

Similarly, for applications where the user wishes to send a mm-wave reference to one or more remote locations, the mixer must again be at the receive end. Either a conventional mixer or an electro-optic mixer may be used. The e-o mixer introduces more noise, but is more rugged (although it does require DC stabilization circuitry). In such cases the e-o mixer may be preferred. Such a system might be used for a phased-array antenna, or, as noted above, for a number of remotely located mixers in systems of the mix-amplify-modulate type, where the local oscillators must be locked to each other.

It is worth noting that the photodiodes for all the systems except the modulate-detect-mix type are low-frequency photodiodes, which are cheaper, more rugged and allow the use of higher optical powers. It is also worth pointing out that the performance of the mode-locked system is the best of the "modulate-at-RF" systems, although I should add that the noise introduced by the mode-locked laser may be considerable if the mode-locking is not highly stable, and I have not taken this into account.

References

[1] Brian H. Kolner and David W. Dolfi, "Intermodulation distortion and compression in an integrated electrooptic modulator," Applied Optics, Vol. 26, No. 17, pp. 3676 - 3680, September 1987

[2] Amnon Yariv and Steve Sanders, "Modelocked Pulses From Semiconductor Lasers at Greater Than 100 GHz," Proc. IEEE LEOS 1991 Summer Topical Meeting, Newport Beach CA, *Optical Millimeter-Wave Interactions: Measurements, Generation, Transmission and Control*, pp. 30-31, July 1991

9. Broadband Substrate-Wave-Coupled Electro-Optic Modulator

9.1 Introduction

This chapter describes a proposed new structure for antenna-coupled electro-optic modulators. This invention is the subject of a patent application.

9.2 The Proposed New Structure

The proposed structure is shown in Figure 9.1. The modulating signal is launched as a slab waveguide mode in the modulator substrate, as shown. Broadband antennas on the surface of the substrate couple the modulating signal into the short transmission lines to form a modulator, as before. In Figure 9.1 the underlying modulator is assumed to be a Mach-Zehnder amplitude modulator. Such a modulator requires provision for DC bias. In our experimental work we applied DC bias to the antenna/modulator segments themselves. In Figure 9.1 we show an alternative method, where the DC bias is achieved using separate electrodes reserved for the purpose. This removes the need to provide for DC bias to each antenna/electrode segment.

Figure 9.2 shows a single antenna/electrode segment in more detail, with some approximate dimensions included. The dark areas in the diagram represent apertures in a metal plane which otherwise covers the entire surface of the modulator. Hence this segment uses a slot-V antenna (I will discuss the reason for this choice below). The electrode is a three-conductor electrode, suitable for push-pull use in a Mach-Zehnder amplitude modulator on X-cut $LiNbO_3$.

This structure differs from the structure used in our experiments in that it uses

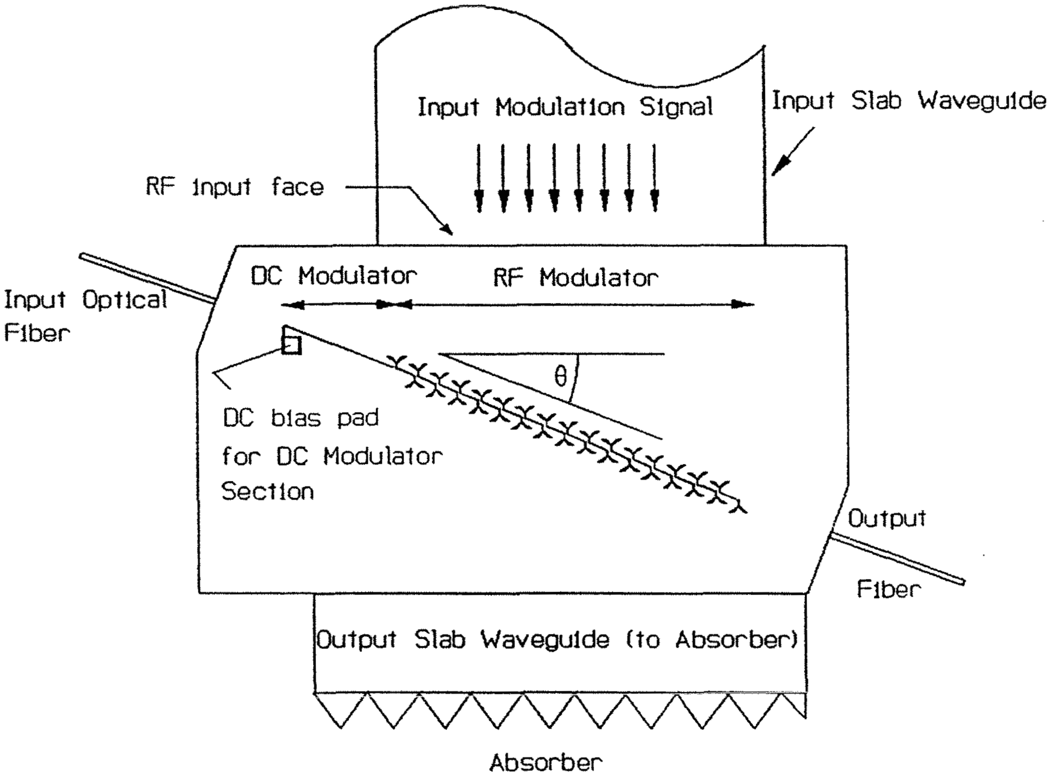

Figure 9.1 Proposed New Modulator Structure

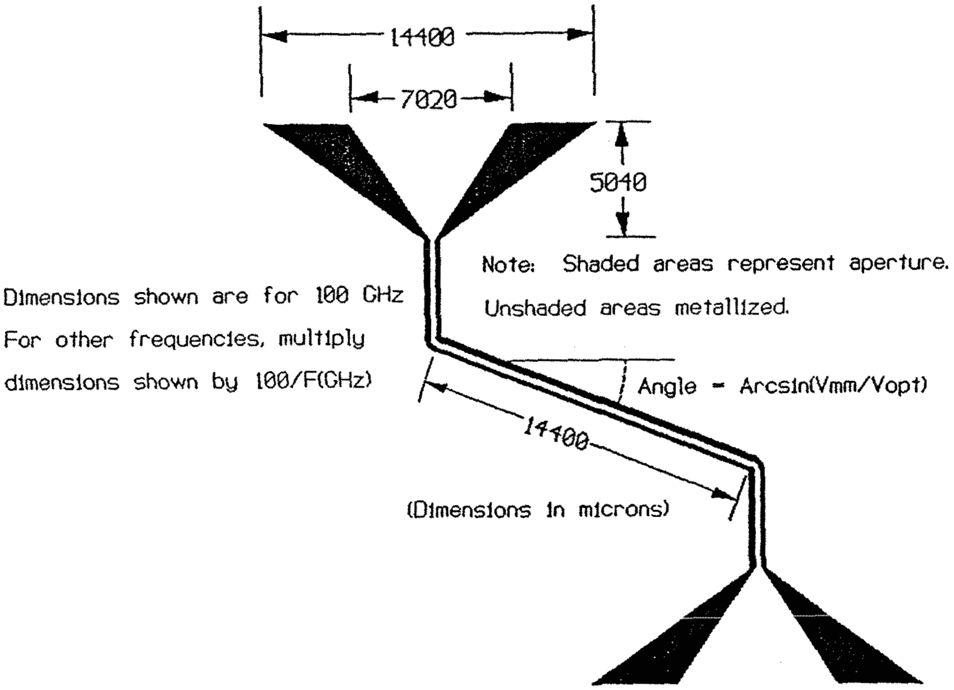

Figure 9.2 Proposed New Modulator Segment

endfire instead of broadside antennas. The endfire antennas allow the use of the substrate as the input waveguide for the signal, which produces a simpler and more robust structure for the modulator. In the modulators we used in the experiments, the transmission-line electrodes were short compared to the dimensions of a broadband broadside antenna, so that it would not have been possible to make efficient use of the area of the modulator substrate if we had used broadband antennas. However, with this new structure it is possible to use broadband antennas, as I will explain below. Furthermore, the phase response of broadband endfire antennas is very much better than that of broadband broadside antennas. This is because broadband antennas couple to different frequencies with different parts of their structure. High frequencies are coupled closer to the feedpoint, low frequencies farther away. In broadside antennas, this means that the high frequencies arrive at the feedpoint first, low frequencies later. In endfire antennas, however, the high-frequency signals couple to the antenna closer to the feedpoint, but have to travel farther to get there because the signal is propagating along the antenna structure instead of normal to it. The result is that they arrive at the feedpoint at about the same time as the low-frequency signals, which had to travel farther along the antenna structure to get to the feedpoint, but had to travel a shorter distance before coupling to the antenna. I should point out that the separate DC bias electrodes are not a distinguishing feature of this new structure; such an arrangement is possible with the earlier structure also.

I said that this structure makes it possible to make efficient use of the modulator substrate area using broadband antennas. The reason is that the proposed structure also provides a solution to the problem of constructing matched terminations for the short transmission line electrodes. In our experiments we could not make terminations, and used open-circuit transmission line electrodes, which I will call *standing-wave electrodes.* In this structure, however, we can terminate the transmission line electrode in a second broadband antenna, as shown, and radiate the power back into the substrate. This means that the electrodes are now true *traveling-wave electrodes*, and these can be longer than standing-wave electrodes. It is this which allows us to use the modulator area effectively, because now the length of the transmission line electrode is comparable to the size of the broadband antenna.

In our experimental modulators the modulating signal was radiated onto the antenna array through the substrate. This required a signal feed structure in a plane normal to the modulator substrate. In the proposed structure, however, the modulating signal propagates in the substrate as a guided wave. This requires a feed structure in the same plane as the modulator substrate. From a practical point of view, this may be more rugged and more convenient to build.

There is a variety of candidate antennas for this structure, such as straight tapered coplanar strip antennas, exponentially tapered slot, exponentially tapered coplanar strips, and so on. The problem with these two-conductor antennas is that they cannot radiate in a direction which is truly endfire when they are on the surface of a dielectric. The reason is that there cannot be a propagating TEM wave along a dielectric interface - a well-known result which can also be observed in the antenna patterns in Appendix A. Quite simply, the required continuity of the fields of such a wave across the interface would be impossible. If the antenna is to couple to a low-order substrate mode it may be necessary to have an antenna radiation pattern which is almost parallel to the surface of the substrate. This can be done if the complementary forms of these antennas are used - see Figure 9.3. The complementary form of the antenna has metal where the bare interface used to be, and vice versa. Now radiation along the interface is possible, because the interface is a metallic boundary, and radiation along such a boundary is possible if the electric field is normal to the boundary. The complementary form of the straight tapered coplanar strip (2-conductor) V antenna, for example, is the straight tapered coplanar waveguide (3-conductor) V antenna. In the switch from the coplanar strip antenna to the coplanar waveguide antenna the polarization of the coupled radiation changes also. The coplanar strip antenna couples to radiation where the electric field is parallel to the interface, with the magnetic field normal to the interface. The coplanar waveguide antenna, on the other hand, couples to radiation where the magnetic field is parallel to the interface, the electric field normal to it. The 3-conductor coplanar waveguide antenna (slot-V antenna) has been investigated by Moussessian & Rutledge [1].

Most of the substrate will be metal-covered, so the dielectric waveguide formed by the substrate will now have one metal boundary. For continuity it will be necessary for the feed structure, too, to have a metal boundary. This makes the mechanical layout of the structure all the easier, since now the feed and modulator can be assembled on a metal backplane for rigidity (Figure 9.4). In Figure 9.4 the antenna/electrode segments are under the modulator substrate, close to the metal backplane. The backplane would have to have a slot in it to provide clearance near the slot antenna array.

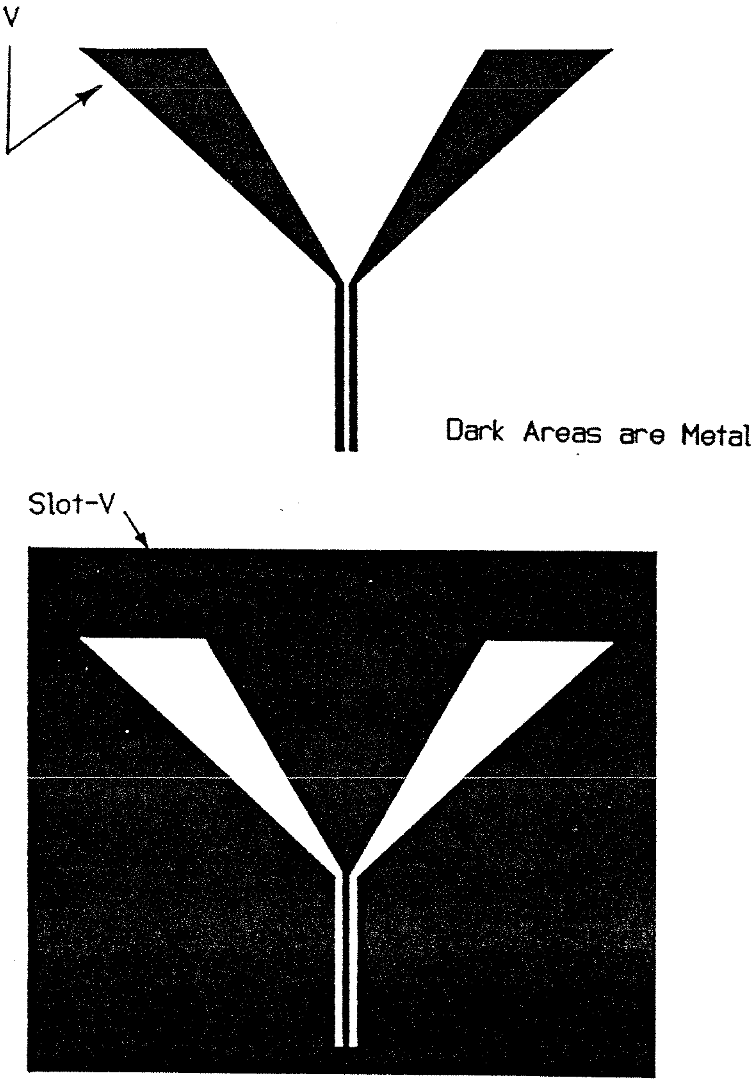

Figure 9.3

V-Antenna (2 Conductors) and its Complement, the Slot-V-Antenna (3 Conductors)

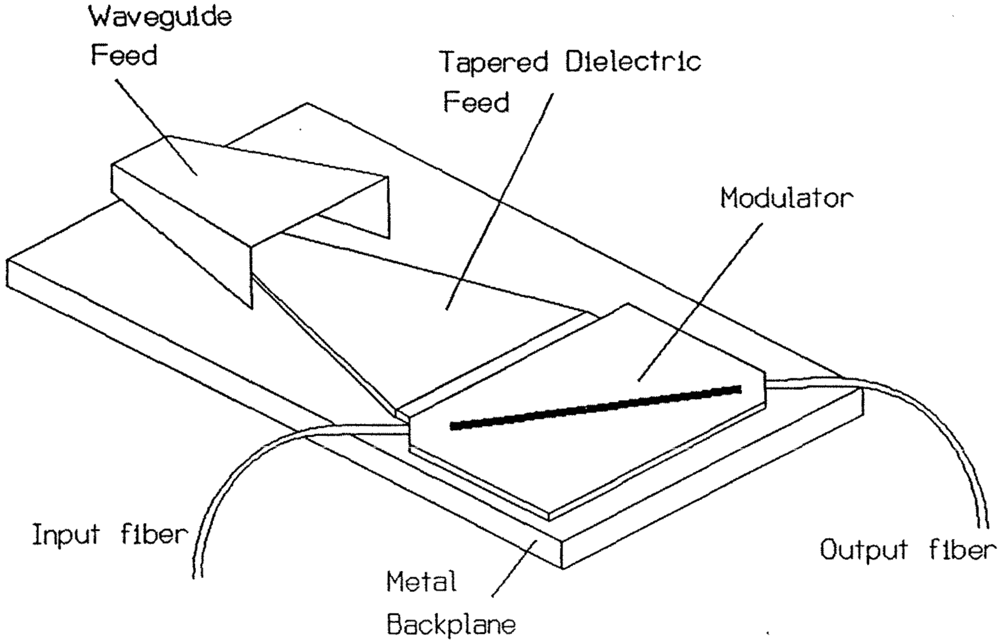

Figure 9.4 Proposed Mechanical Layout

References

[1] Alina Moussessian and David B. Rutledge, "A Millimeter-Wave Slot-V Antenna," Proc IEEE AP-S International Symposium, Chicago, Illinois, 18 - 25 July 1992

Appendix A

Radiation Pattern of the Interfacial Antenna

A1. Introduction

The problem of an antenna on a dielectric half-space (or at the interface between two dielectric half-spaces) has been addressed by a number of workers [1 - 4] using a variety of mathematical techniques. In particular [3] is quite detailed. The purpose of this appendix is to provide physical insight into the mechanisms which affect the antenna pattern of an interfacial antenna, and to use this insight to show explicitly how the antenna pattern of an interfacial wire antenna of arbitrary length and shape can be computed. By way of illustration, the radiation pattern of a thin V-antenna of arbitrary length and angle is computed in closed form, subject to the assumption that the current distribution in the wire is sinusoidal. Special cases of interest include the infinitesimal interfacial dipole, which has been analysed previously by Engheta et al. [2] by a method which is more mathematically involved than that presented here. This method gives an identical result.

A2. The Interfacial Antenna

Consider an antenna above a dielectric interface. Suppose the antenna lies entirely in a plane parallel to the interface, so that its antenna pattern above that plane is a mirror image of its pattern below it (in the absence of the interface itself). Referring to Figure A1, the far-field of the antenna in the direction (θ) in the presence of the interface is composed of two parts: one is

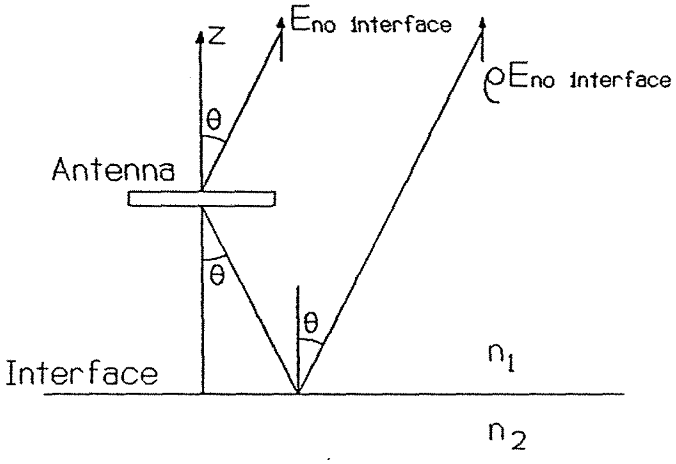

Figure A1 Computation of Antenna Pattern of an Antenna Above a Dielectric Interface the direct radiation in that direction by the antenna in the absence of the interface; the other is the radiation reflected by the dielectric interface. Note that only the antenna far-fields need be considered, even though the dielectric interface itself may be in the near-field - this point is addressed in [3]. Essentially, fields which are not radiated by the antenna are not radiated after reflection from a surface which is invariant in the plane of reflection. The problem of finding the far-field of the antenna can be solved by linear superposition of radiation fields from the antenna itself and from its reflection in the dielectric interface. The reflected wave is the same as the direct wave except for a phase term due to the extra distance traveled and a reflection coefficient which in general affects both amplitude and phase. As the antenna moves closer to the interface the phase term due to extra distance traveled becomes smaller. When the antenna lies on the interface this phase term disappears entirely, and the far-field in the medium n_1 is simply

$$E_{far} = E_{no\ interface}\ (\ 1 + \rho\ )\ . \tag{1}$$

The reflection coefficient ρ depends on both the angle of incidence and polarization of the wave. For horizontally polarized waves it is :

$$\rho = \frac{n_1 \cos\theta_1 - n_2 \cos\theta_2}{n_1 \cos\theta_1 + n_2 \cos\theta_2}\ , \tag{2}$$

where θ_1 is the angle of incidence,

and
$$\cos\theta_2 = \sqrt{1 - \left(\frac{n_1}{n_2}\right)^2 \sin^2\theta_1}\ . \tag{3}$$

For vertically polarized waves the reflection coefficient is:

$$\rho = \frac{n_1 \cos\theta_2 - n_2 \cos\theta_1}{n_1 \cos\theta_2 + n_2 \cos\theta_1} . \tag{4}$$

Using the co-ordinate system in Figure A2, the waves transmitted by the antenna may be analysed into two components, whose electric field vectors are $E_\theta(r,\theta,\phi)$ and $E_\phi(r,\theta,\phi)$. At the dielectric interface these components are, respectively, vertically and horizontally polarized. If the field components transmitted by the antenna in the absence of an interface in the direction (r,θ,ϕ) are denoted as $E_{i\theta}(r,\theta,\phi)$ and $E_{i\phi}(r,\theta,\phi)$, then the following expressions hold:

$$E_\theta(r,\theta_1,\phi) = E_{i\theta}(r,\theta_1,\phi)\left(1 + \frac{n_1 \cos\theta_2 - n_2 \cos\theta_1}{n_1 \cos\theta_2 + n_2 \cos\theta_1}\right), \tag{5}$$

$$E_\phi(r,\theta_1,\phi) = E_{i\phi}(r,\theta_1,\phi)\left(1 + \frac{n_1 \cos\theta_1 - n_2 \cos\theta_2}{n_1 \cos\theta_1 + n_2 \cos\theta_2}\right). \tag{6}$$

Rewriting these in terms of θ_1 only, and writing θ_1 as θ now,

$$E_\theta(r,\theta,\phi) = E_{i\theta}(r,\theta,\phi)\,\frac{2\, n_1 \sqrt{1 - \left(\frac{n_1}{n_2}\right)^2 \sin^2\theta}}{n_2 \cos\theta + n_1 \sqrt{1 - \left(\frac{n_1}{n_2}\right)^2 \sin^2\theta}} , \tag{7}$$

$$E_\phi(r,\theta,\phi) = E_{i\phi}(r,\theta,\phi)\,\frac{2\, n_1 \cos\theta}{n_1 \cos\theta + n_2 \sqrt{1 - \left(\frac{n_1}{n_2}\right)^2 \sin^2\theta}} . \tag{8}$$

This reduces the problem of finding the antenna pattern of an antenna lying on a dielectric interface to one of finding the antenna pattern of the same antenna

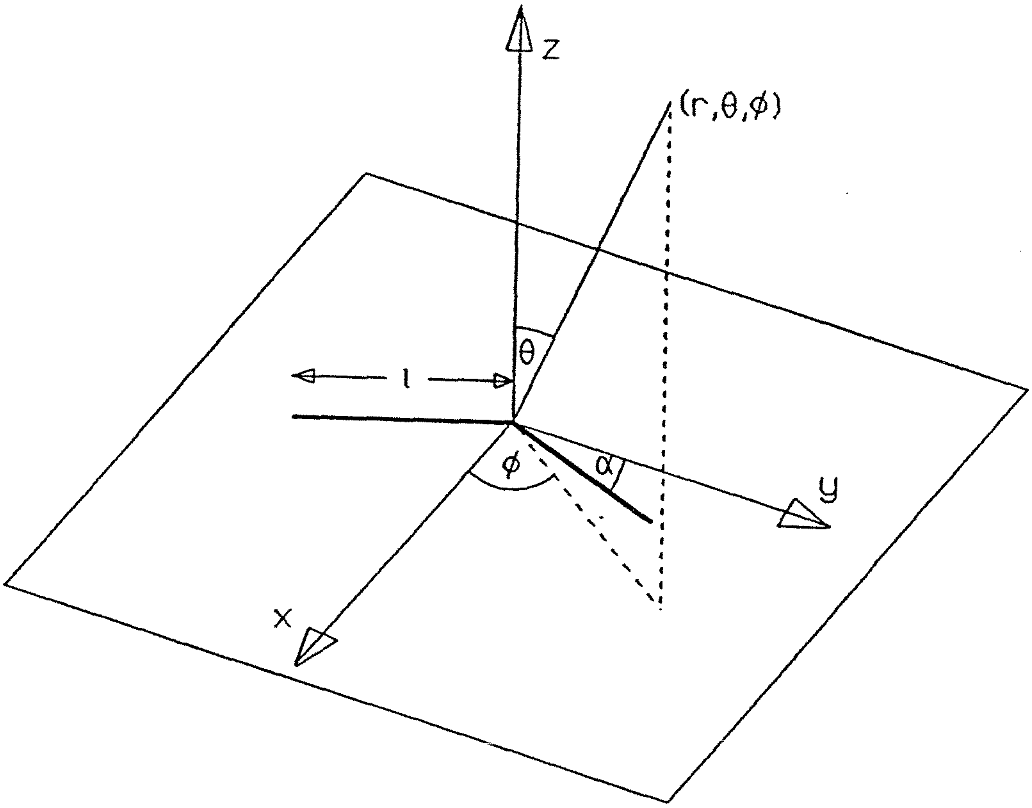

Figure A2 Co-ordinate System for the Antenna Pattern Computations *with the same current distribution* in the absence of the interface (i.e., in dielectric n_1 only).

Up to this point we have not considered the effect of the interface on the near fields. The interface changes the current distribution on the antenna as a result of this interaction. For a thin wire antenna the current is distributed on the antenna as it would be if the antenna were embedded in a medium whose dielectric constant were between the values actually present on either side of the interface. This means that, although the problem has now been reduced to one in a single dielectric medium, it involves a current distribution which might not naturally exist in that medium. This means that deriving the pattern of an antenna on an interface from the measured pattern of one in a single medium is not possible in general, unless there is some way to force an appropriate current-distribution on the test antenna.

A3. Computation of $E_{i\theta}(\theta,\phi)$ and $E_{i\phi}(\theta,\phi)$ for a V-Antenna

The antenna pattern in the absence of an interface is computed using the magnetic vector potential function **A** [5], where

$$\mathrm{A(x,y,z,t)} = \frac{\mathrm{e}^{j(\omega t - kr)}\mu_o}{4\,\pi\,\mathrm{r}} \int_V \mathrm{J}(\xi,\eta)\,\mathrm{e}^{jkL}\,\mathrm{dV}\,, \tag{9}$$

in which

$$L = \xi\,\sin\theta\,\cos\phi + \eta\,\sin\theta\,\sin\phi\,, \tag{10}$$

where the (ξ,η) plane is the plane in which the antenna lies.

The magnetic vector potential **A** is the product of a spherical wave with the directional weighting function

$$\mathbf{a}(\theta,\phi) = \int_V \mathbf{J}(\xi,\eta)\, e^{jkL}\, d\xi\, d\eta\ . \tag{11}$$

Then:

$$\mathbf{E} = (c^2/j\omega)\ \nabla \times \nabla \times \mathbf{A}\ , \tag{12}$$

$$\mathbf{B} = \nabla \times \mathbf{A}\ . \tag{13}$$

Performing these operations, the result is that the radiated fields are:

$$\mathbf{E} = -j\omega \mathbf{A}_T\ , \tag{14}$$

$$\mathbf{H} = \left(\frac{1}{\eta}\right) \mathbf{1_r} \times \mathbf{E}\ , \tag{15}$$

and the average power density at the point (r,θ,ϕ) is given by:

$$P(r,\theta,\phi) = \frac{1}{2}\left(\frac{k_1{}^2\, \eta_1}{(4\ \pi\ r)^2}\right)\left(\ |\ a_\theta(\theta,\phi)\ |^2 + |\ a_\phi(\theta,\phi)\ |^2\ \right). \tag{16}$$

The V-antenna is in two parts, which may be parameterized as follows:

Part 1 Parameter q : $-\ell < q < 0$

$$\left.\begin{aligned} &I_\xi(q) = -\ I_o \sin\alpha\ \sin[k_a\ (\ell + q)\ ] \\ &I_\eta(q) = I_o \cos\alpha\ \sin[k_a\ (\ell + q)\ ] \\ &\text{Phase Parameter } L = q\ \sin\theta\ \sin(\phi - \alpha)\ ; \end{aligned}\right\} \tag{17}$$

Part 2 Parameter q: $0 < q < \ell$

$$\left.\begin{array}{l} I_\xi(q) = I_o \sin\alpha \sin[k_a (\ell - q)] \\ I_\eta(q) = I_o \cos\alpha \sin[k_a (\ell - q)] \\ \text{Phase Parameter } L = q \sin\theta \sin(\phi+\alpha) . \end{array}\right\} \quad (18)$$

Notice that the current distribution in each part is sinusoidal, with wavelength $\lambda_a = \frac{2\pi}{k_a}$. This wavelength depends on the presence of the interface, although the rest of the calculation does not take the existence of the interface into account at all (remember, this calculation is to find the antenna pattern in the absence of the interface). The determination of the constant k_a is not actually necessary for the mathematics, although obviously it must be determined before the resulting antenna pattern can be computed. Kominami et al. [4] have determined that, for infinitesimal dipole thickness, k_a is given by:

$$k_a = \sqrt{\frac{k_1^2 + k_2^2}{2}} , \tag{19}$$

where k_1 and k_2 are the wavenumbers in the two dielectrics.

The component $a_{i\theta}(\theta, \phi)$ is given by [5]

$$\begin{aligned} a_{i\theta}(\theta,\phi) = {} & I_o \cos\theta \int_{-\ell}^{0} \sin[k_a(\ell + q)] \sin(\phi - \alpha)\, e^{\,j\,k\,q \sin\theta \sin(\phi\text{-}\alpha)}\, dq , \\ & + I_o \cos\theta \int_{0}^{\ell} \sin[k_a(\ell - q)] \sin(\phi+\alpha)\, e^{j\,k\,q \sin\theta \sin(\phi+\alpha)}\, dq . \end{aligned} \tag{20}$$

In order to evaluate this integral, it is useful to know that

$$\int e^{ax} \sin(bx + c)\, dx = \frac{e^{ax}}{a^2 + b^2} [\, a \sin(bx + c) - b \cos(bx + c)\,] \,. \tag{21}$$

The full result is:

$$\begin{aligned} a_{i\theta}(\theta,\phi) &= \cos\theta \sin(\phi-\alpha) \frac{k_a[\cos\{k\ell \sin\theta \sin(\phi-\alpha)\} - \cos(k_a\ell)]}{{k_a}^2 - k^2 \sin^2\theta \sin^2(\phi-\alpha)} \\ &+ \cos\theta \sin(\phi+\alpha) \frac{k_a[\cos\{k\ell \sin\theta \sin(\phi+\alpha)\} - \cos(k_a\ell)]}{{k_a}^2 - k^2 \sin^2\theta \sin^2(\phi+\alpha)} \\ &+ j \cos\theta \sin(\phi-\alpha) \frac{k \sin\theta \sin(\phi-\alpha) \sin(k_a\ell) - k_a \sin\{k\ell \sin\theta \sin(\phi-\alpha)\}}{{k_a}^2 - k^2 \sin^2\theta \sin^2(\phi-\alpha)} \\ &+ j \cos\theta \sin(\phi+\alpha) \frac{-k \sin\theta \sin(\phi+\alpha) \sin(k_a\ell) + k_a \sin\{k\ell \sin\theta \sin(\phi+\alpha)\}}{{k_a}^2 - k^2 \sin^2\theta \sin^2(\phi+\alpha)} \,. \end{aligned} \tag{22}$$

The ϕ-component comes from the integral

$$\begin{aligned} a_{i\phi}(\theta,\phi) &= \int_{-\ell}^{0} \sin[k_a(\ell+q)] \cos(\phi-\alpha)\, e^{j\, k\, q \sin\theta \sin(\phi-\alpha)}\, dq \\ &+ \int_{0}^{\ell} \sin[k_a(\ell-q)] \cos(\phi+\alpha)\, e^{j\, k\, q \sin\theta \sin(\phi+\alpha)}\, dq \,. \end{aligned} \tag{23}$$

The closed-form solution of this integral is:

$$a_{i\phi}(\theta,\phi) = \cos(\phi-\alpha) \frac{k_a[\cos\{k\ell \sin\theta \sin(\phi-\alpha)\} - \cos(k_a\ell)]}{{k_a}^2 - k^2 \sin^2\theta \sin^2(\phi-\alpha)}$$

$$+ \cos(\phi+\alpha)\,\frac{k_a[\cos\{k\ell\,\sin\theta\,\sin(\phi+\alpha)\} - \cos(k_a\ell)]}{k_a{}^2 - k^2\,\sin^2\theta\,\sin^2(\phi+\alpha)}$$

$$+\, j\,\cos(\phi-\alpha)\,\frac{k\,\sin\theta\,\sin(\phi-\alpha)\,\sin(k_a\ell) - k_a\,\sin\{k\ell\,\sin\theta\,\sin(\phi-\alpha)\}}{k_a{}^2 - k^2\,\sin^2\theta\,\sin^2(\phi-\alpha)}$$

$$+\, j\,\cos(\phi+\alpha)\,\frac{-k\,\sin\theta\,\sin(\phi+\alpha)\,\sin(k_a\ell) + k_a\,\sin\{k\ell\,\sin\theta\,\sin(\phi+\alpha)\}}{k_a{}^2 - k^2\,\sin^2\theta\,\sin^2(\phi+\alpha)}\,. \tag{24}$$

The complete result for power density at a point (r,θ,ϕ) in dielectric n_1 for the V-antenna, when the effect of the interface on each of the field components is included, is:

$$P(r,\theta,\phi) = \frac{I_o{}^2}{2}\left(\frac{k_1{}^2\,\eta_1}{(4\,\pi\,r)^2}\right)\left(|\,a_{i\theta}(\theta,\phi)\,|^2\,\frac{4\,n_1{}^2\left(1 - \left(\frac{n_1}{n_2}\right)^2\sin^2\theta\right)}{\left|\,n_2\cos\theta + n_1\sqrt{1 - \left(\frac{n_1}{n_2}\right)^2\sin^2\theta}\,\right|^2}\right.$$

$$\left. +\,|\,a_{i\phi}(\theta,\phi)\,|^2\,\frac{4\,n_1{}^2\cos^2\theta}{\left|\,n_1\cos\theta + n_2\sqrt{1 - \left(\frac{n_1}{n_2}\right)^2\sin^2\theta}\,\right|^2}\right), \tag{25}$$

where $a_{i\theta}(\theta,\phi)$ and $a_{i\phi}(\theta,\phi)$ are given in equations (22) and (24) respectively.

A4. Special Case: Dipole in Free Space

As a "sanity-check" on these results, we can compare the above with some known results in special cases, the simplest of which is the straight dipole in free space. In this situation, the conditions applied to the above result are:

$$\left.\begin{aligned} \alpha &= 0 \\ k_1 &= k_a = k \\ n_1 &= n_2\,. \end{aligned}\right\} \tag{26}$$

Note that whenever α=0 the expression for radiated power simplifies considerably, as the imaginary terms cancel, and the real terms become equal to each other in pairs.

Then the result becomes:

$$P(r,\theta,\phi) = \frac{I_o^2\, n_1}{8\,\pi^2\, r^2}\sqrt{\frac{\mu_o}{\epsilon_o}}\;\frac{[\cos(k\ell\,\sin\theta\,\sin\phi)\text{ - }\cos(k\ell)]^2}{\{1\text{ - }\sin^2\theta\,\sin^2\phi\}^2}\left(\cos^2\theta\,\sin^2\phi + \cos^2\phi\right). \tag{27}$$

This is indeed the expression for the antenna pattern of a dipole in free space. The total length of the dipole is 2ℓ.

A5. Special Case: V-Antenna in Free Space

Here the conditions are:

$$\left.\begin{aligned} k_1 &= k_a = k \\ n_1 &= n_2\,. \end{aligned}\right\} \tag{28}$$

The equations become a little simpler, but not much. Figure A3 shows the E-plane power pattern (i.e., in the plane of the antenna) for a V-antenna whose arms are each one wavelength long, and where the angle between the arms is 110°. This example is given by Carter et al. [6]. If the arms are made 8 wavelengths long, and the angle between them is decreased to 35°, we get a very directional pattern. The forward half of the E-plane pattern is shown in Figure A4. Note that the pattern is exactly the same in the other direction. This pattern can also be compared with [6].

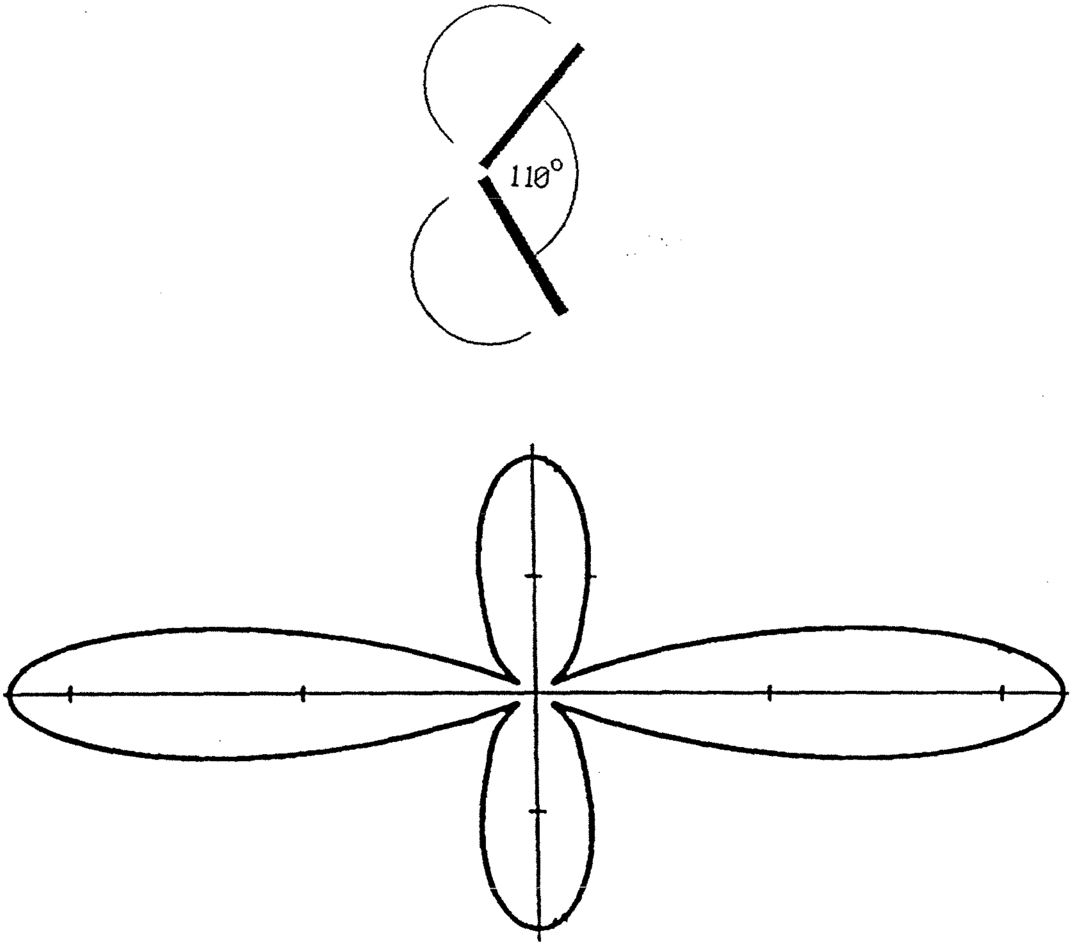

Figure A3 Antenna pattern of a V-antenna whose arms are each one wavelength long. The V-angle is 110°. The pattern shown is in the plane of the V (the E-plane).

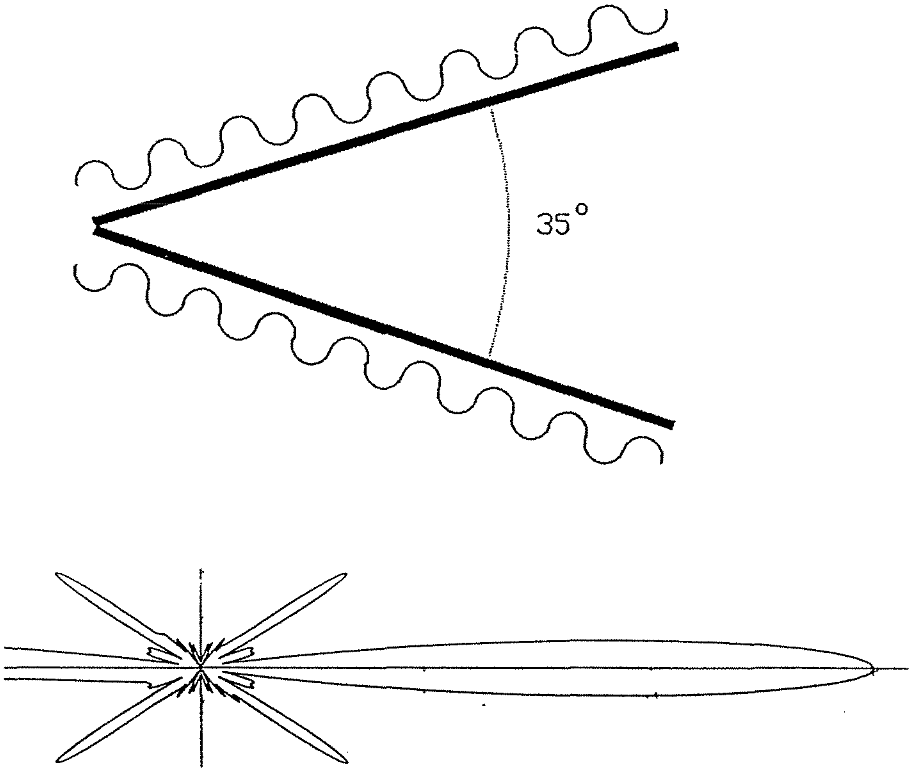

Figure A4 Antenna pattern of a V-antenna whose arms are each eight (8) wavelengths long. The V-angle is 35°. The pattern shown is in the plane of the V (the E-plane).

A6. Special Case: Infinitesimal Dipole on a Dielectric Half-Space

This time the conditions are:

$$\left.\begin{aligned} \alpha &= 0 \\ k_1 &= k \\ n_1 &= n \\ n_2 &= 1 \\ \ell &\rightarrow 0\,. \end{aligned}\right\} \quad (29)$$

Now the expression for radiated power becomes:

$$P(r,\theta,\phi) = \lim_{\ell\to 0} \frac{I_o^2\, k^2\, n^3}{2\,\pi^2\, r^2} \sqrt{\frac{\mu_o}{\epsilon_o}} \cos^2\theta \, \frac{\left(\cos(k\ell \sin\theta \sin\phi) - \cos(k_a\ell)\right)^2}{k_a^2 \left(1 - \left(\frac{k}{k_a}\right)^2 \sin^2\theta \sin^2\phi\right)^2}$$

$$\times \left(\frac{|1 - n^2 \sin^2\theta| \quad \sin^2\phi}{|\cos\theta + n\sqrt{1 - n^2 \sin^2\theta}\,|^2} + \frac{\cos^2\phi}{|\,n \cos\theta + \sqrt{1 - n^2 \sin^2\theta}\,|^2} \right). \quad (30)$$

Expanding the cosine terms which involve ℓ as power series,

$$P(r,\theta,\phi) = \lim_{\ell\to 0} \frac{I_o^2\, k^2\, k_a^2\, n^3\, \ell^4}{8\,\pi^2\, r^2} \sqrt{\frac{\mu_o}{\epsilon_o}} \cos^2\theta \left(\frac{|1 - n^2 \sin^2\theta|}{|\cos\theta + n\sqrt{1 - n^2 \sin^2\theta}\,|^2} \sin^2\phi \right.$$

$$\left. + \frac{\cos^2\phi}{|\,n \cos\theta + \sqrt{1 - n^2 \sin^2\theta}\,|^2} \right). \quad (31)$$

The input current to the dipole is $I_o \sin(k_a\ell)$, which becomes $I = I_o\, k_a\ell$ as

$\ell \to 0$, so

$$P(r,\theta,\phi) = \frac{I^2\, k^2\, n^3\, \ell^2}{8\, \pi^2\, r^2} \sqrt{\frac{\mu_o}{\epsilon_o}} \cos^2\theta \left(\frac{|1 - n^2 \sin^2\theta|}{|\cos\theta + n\sqrt{1 - n^2 \sin^2\theta}\,|^2} \sin^2\phi \right.$$
$$\left. + \frac{\cos^2\phi}{|\, n \cos\theta + \sqrt{1 - n^2 \sin^2\theta}\,|^2} \right). \qquad (32)$$

This expression is in a somewhat different form to that derived by Engheta et al. [2], but with the appropriate changes of co-ordinates it is algebraically identical to that result.

A7. V-Antenna on a Dielectric Half-Space

The most general case, the V-antenna on a dielectric half-space, requires the full set of equations (22), (24), and (25). For antennas whose arm-lengths are smaller than one-half interface wavelength long, bending the antenna into a V does not do anything very interesting. Figures A5 and A6, for example, show the H-plane patterns (i.e., in the plane, normal to the interface, which bisects the V) of a straight two-half-waves-in-phase dipole and a 140° two-half-waves-in-phase V, respectively, on a substrate of ϵ=28. There is very little difference between the two. On the other hand, if the arm-lengths are increased to one interface wavelength, there is no power transmitted in the H-plane by a straight dipole, but if the antenna is bent to form a 100° V, its H-plane pattern is as shown in Figure A7.

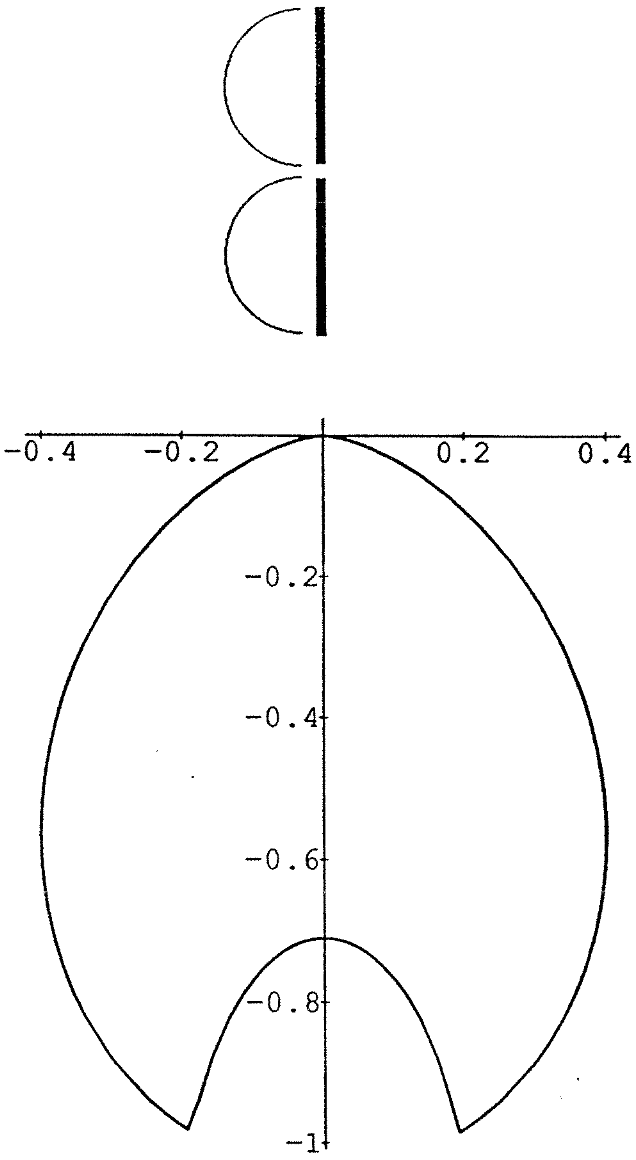

Figure A5 Antenna pattern of a two-half-waves-in-phase dipole on the surface of a dielectric, $\epsilon = 28$. The pattern shown is in the dielectric, in the plane normal to the dipole (the H-plane).

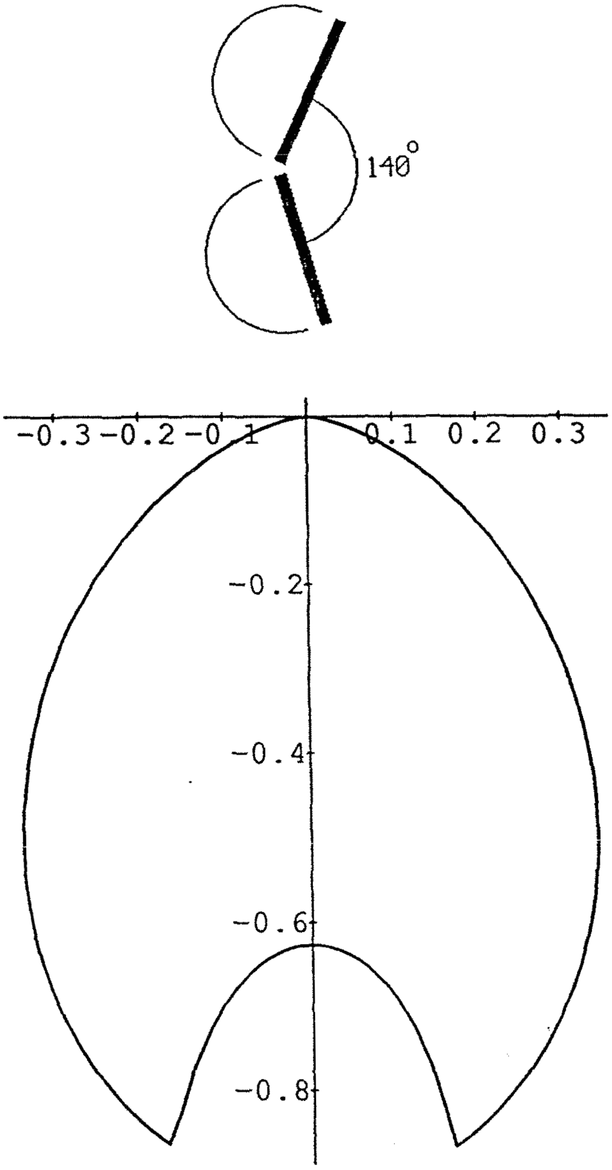

Figure A6 Antenna pattern of a V antenna on the surface of a dielectric, ϵ -28. Each arm of the V is one half-surface-wavelength long. The V angle is 140°. The pattern shown is in the dielectric, in the plane which bisects the V.

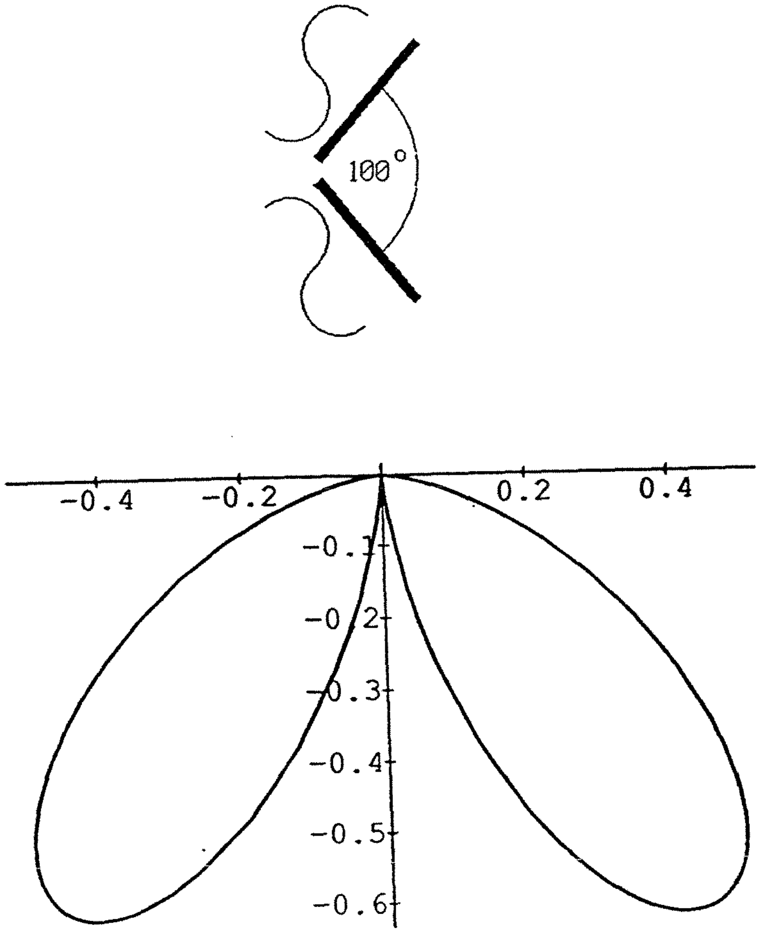

Figure A7 Antenna pattern of a V antenna on the surface of a dielectric, $\epsilon = 28$. Each arm of the V is one surface-wavelength long. The V angle is 100°. The pattern shown is in the dielectric, in the plane which bisects the V.

A8. Conclusion

I have shown a practical method of computing the complete far-zone fields and radiated power pattern of an arbitrarily-shaped wire antenna on the interface between two dielectric half-spaces, assuming known (e.g., sinusoidal) current distribution on the wire. Physical insight into the mechanisms involved in the antenna pattern is the basis of the method. By way of illustration, the antenna pattern of an interfacial V-antenna of arbitrary length and angle is computed, compared with known results in special cases, and used to show the behavior of some interfacial V-antennas.

References

[1] C. R. Brewitt-Taylor, D. J. Gunton and H. D. Rees, "Planar Antennas on a Dielectric Surface," Electron. Lett. Vol. 17, No. 20, 1st October 1981

[2] N. Engheta, C.H. Papas and C. Elachi, "Radiation Patterns of Interfacial Dipole Antennas," Radio Science, Vol. 17, No. 6, pp. 1557-1566, November-December 1982

[3] G. S. Smith, "Directive Properties of Antennas for Transmission into a Material Half-Space," IEEE Trans. Ant. & Prop., Vol. AP-32, No. 3, March 1984

[4] M. Kominami, D. M. Pozar and D. H. Schaubert, "Dipole and Slot Elements and Arrays on Semi-Infinite Substrates," IEEE Trans. Ant. & Prop., Vol. AP-33, No. 6, June 1985

[5] R. S. Elliott, Antenna Theory and Design, Ch. 1, Prentice-Hall, Inc., 1981

[6] P.S. Carter, C.W. Hansell, and N.E. Lindenblad, "Development of Directive Transmitting Antennas by R.C.A. Communications Inc.," Proc. IRE, Vol. 19, pp. 1773 - 1842, October 1931

Appendix B

Optimum Power Distribution in Traveling-Wave Electro-Optic Modulators

B1. Abstract

Traveling wave modulators suffer from phase-velocity mismatch and transmission-line attenuation. Where high modulation sensitivity is required at a specific frequency, it may be optimal to split the modulator into a number of shorter segments, each driven with a fraction of the available modulation signal power. I show how to determine the optimum configuration in the cases of: a modulator which suffers from neither problem; a modulator whose segment lengths are fixed by some constraint; a lossy modulator; and in the case of a phase-velocity-mismatched modulator. In addition I examine the bandwidth implications of the various approaches.

B2. Introduction

Traveling-wave electro-optic modulators are usually based on electro-optic phase modulators. The light propagates through a crystal whose refractive index depends on the modulating electric field strength. The output phase of the optical signal is thus controlled by the modulating field. At low frequencies the phase deviation produced varies linearly with the interaction length and with the applied electric field. If an amplitude modulator is required the modulated beam is interfered with an unmodulated beam, converting phase modulation to amplitude modulation.

At high modulation frequencies there are two common problems with these modulators. First, the phase-velocity of the modulating signal along the electrode may differ appreciably from the phase-velocity of the optical signal traveling along the optical waveguide, causing the two to fall out of step within the interaction length. The optical phase change then reflects a time-averaged version of the modulating signal. The second problem is that the attenuation of the transmission line used to guide the modulating signal increases at higher frequencies, so that the modulating signal dies away after a short distance, limiting the effective interaction length.

In either case it may be possible to build a modulator which meets all required specifications at some design frequency except the sensitivity requirement. One could consider using a number of such modulator segments cascaded to increase the output signal. This would mean dividing the available modulation signal power between the modulator segments. I examine some cases where this is an advantage, and note where it is not.

B3. How to Split a Traveling-Wave Modulator

When splitting a Mach-Zehnder amplitude modulator into shorter segments, one can split the optical beam into two paths, then pass each of the paths through a number of short phase-modulator segments, then recombine the beams-paths after the final phase-shifter. Alternatively one can split the modulator by making a number of complete amplitude modulators, each with the shorter interaction length. This latter approach, however, introduces very severe distortion, which is hardly desireable. Therefore we will only need to consider the former approach. This means that it is only necessary to determine the optimum splitting of phase modulators. If an amplitude modulator is required, one builds two phase modulators. The optical beam is split between the phase modulators, which are driven in opposite phases, and the output beams are recombined. The net output is an amplitude-modulated signal. The theory presented here is not appropriate for $\Delta\beta$ coupler amplitude modulators, which cannot be treated in this way.

B4. The Definitions

Referring to Figure B1, the **modulator** consists of N **modulator segments.** The fraction of the total modulation signal power delivered to the kth segment is P_k. The **phase contribution** of the kth modulating segment may be written as

$$\phi_k(P_k) = a_k \, P_k^{1/2} \,, \tag{1}$$

where a_k depends on the details of the modulator segment.

B5. Ideal Modulator Segments

An ideal modulator segment is one which is not affected by phase-velocity mismatch or attenuation. The kth such segment makes a phase contribution

$$\phi_k(L_k,P_k) = Q \, P_k^{1/2} \, L_k \,, \tag{2}$$

where
P_k is the modulation signal power driving the segment,
L_k is the interaction length of the segment,
Q is a constant, with the same value for all segments.

The modulator is to be constructed of a number N of these modulator segments.

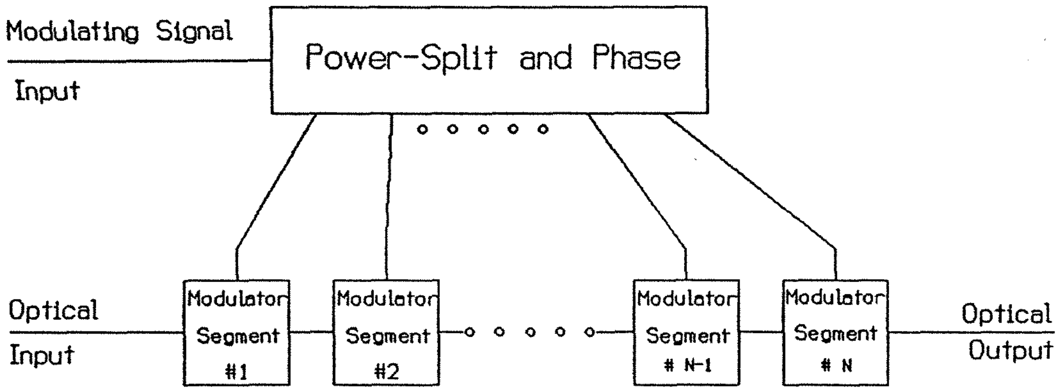

Figure B1 Splitting a Modulator
- Definitions

The total interaction length of this modulator is L, and the total modulation signal power available is P. Then the total phase change produced by the entire modulator is ϕ, where

$$\phi = \sum_k \mathrm{Q}\, \mathrm{P}_k^{1/2}\, \mathrm{L}_k \,, \tag{3}$$

$$\mathrm{L} = \sum_k \mathrm{L}_k \,, \tag{4}$$

$$\mathrm{P} = \sum_k \mathrm{P}_k \,. \tag{5}$$

The goal is to maximize ϕ for given values of L and P. Consider the Nth and (N-1)th modulator segments. Suppose their combined length is L_c and their combined power is P_c. Their combined phase contribution is ϕ_c. Then

$$\mathrm{L}_{N-1} = \mathrm{L}_c - \mathrm{L}_N \,, \tag{6}$$

$$\mathrm{P}_{N-1} = \mathrm{P}_c - \mathrm{P}_N \,, \tag{7}$$

$$\phi_c = \mathrm{Q}\, [\, (\mathrm{P}_c - \mathrm{P}_N)^{1/2}(\mathrm{L}_c - \mathrm{L}_N) + \mathrm{P}_N^{1/2}\, \mathrm{L}_N \,] \,. \tag{8}$$

The maximum of this function occurs at two endpoints, where

either $$\mathrm{P}_N = \mathrm{P}_c \quad \mathrm{L}_N = \mathrm{L}_c \,, \tag{9}$$

or $$\mathrm{P}_N = 0 \quad \mathrm{L}_N = 0 \,. \tag{10}$$

So the best thing to do is to use just one long modulator segment (driven with all the power) in place of the two original segments. The modulator now has a total of (N-1) modulator segments. This procedure can be repeated inductively to show that the global optimum is a single modulator segment with length L, driven with all the available modulation signal P. This gives the result that

$$\phi = \mathrm{Q\,L}\sqrt{\mathrm{P}}\ . \tag{11}$$

Clearly, for maximum phase deviation both L and P should be made as large as possible, but increasing L is more effective than increasing P.

B6. Length-Limited Modulator Segments

If modulator segments are restricted to have a length less than some maximum value, the optimum configuration changes. For example, phase-velocity mismatch means that there will be an optimum length for each modulator segment, so that if the length of a modulator segment is increased beyond a certain value the phase contribution actually begins to decrease. Suppose a modulator is to be constructed using modulator segments, each of which has this optimum length L_o. Then

$$\phi = \sum_{k=1}^{N} \mathrm{Q\,L}_o\,\mathrm{P}_k^{\ 1/2}, \tag{12}$$

where

$$\mathrm{P} = \sum_{k=1}^{N} \mathrm{P}_k\ . \tag{13}$$

The maximization now amounts to finding the maximum of

$$\sum_{k=1}^{N} \mathrm{P}_k^{\ 1/2}, \tag{14}$$

which occurs when $$P_k = P/N. \tag{15}$$

So now the optimum occurs when the power is distributed equally between the modulator segments. Its value is

$$\phi = Q\, L_o \sqrt{P}\, \sqrt{N} = Q \sqrt{L_o\, L\, P}\ . \tag{16}$$

Note that the total interaction length L is now $L = NL_o$. It is obvious from this that N should be made as large as possible. So, when there is an optimum length for a single modulator segment but they can be combined to make a better modulator, the best approach is to use as many modulator segments as possible and to split the power equally between them. The improvement thus obtained varies as $\sqrt{N}$, which means that the improvement varies as $\sqrt{L}$. This dependence on L is not as good as the result for the ideal modulator segments.

B7. Loss-Limited Modulator Segments

Transmission-line loss may be the effect which limits the useful length of the modulator. The attenuation of the modulating signal in the transmission line makes each additional unit of transmission-line length less effective. Nevertheless, there is no optimum line length. It should still be made as long as possible.

However, it may be more effective to split this length L equally between N modulating segments. This would also involve splitting the available modulation drive power, of course.

If the electric field attenuation on the transmission line is α, then the phase contribution from the kth modulator segment is

$$\phi_k = \mathrm{Q} \left(\frac{\mathrm{P}}{\mathrm{N}}\right)^{1/2} \int_0^{L/N} \mathrm{e}^{-\alpha x}\, \mathrm{dx}\ , \tag{17}$$

$$= \mathrm{Q} \left(\frac{\mathrm{P}}{\mathrm{N}}\right)^{1/2} \frac{1}{\alpha} \left[\, 1 - \mathrm{e}^{-\alpha L/N} \right] . \tag{18}$$

The total phase contribution is then

$$\phi = \mathrm{N}\, \phi_k = \frac{\mathrm{Q}\sqrt{\mathrm{P}}\sqrt{\mathrm{N}}}{\alpha} \left[\, 1 - \mathrm{e}^{-\alpha L/N} \right] . \tag{19}$$

Observe that the correct number of sections to use is N when

$$\sqrt{\mathrm{N\text{-}1}} \left[\, 1 - \mathrm{e}^{-\alpha L/(N-1)} \right] \le \sqrt{\mathrm{N}} \left[\, 1 - \mathrm{e}^{-\alpha L/N} \right] \le \sqrt{\mathrm{N+1}} \left[\, 1 - \mathrm{e}^{-\alpha L/(N+1)} \right] . \tag{20}$$

So the number of sections to use is implicitly defined as a function of (α L). The optimum values are listed in Table 7.1.

As a rule of thumb based on the results in the table, the modulator should be split so that the loss in the transmission line of a single modulator segment does not exceed 12 dB approximately.

αL (nepers)	αL (dB)	N
0 - 1.76	0 - 15.3	1
1.76 - 3.07	15.3 - 26.6	2
3.07 - 4.34	26.6 - 37.6	3
4.34 - 5.6	37.6 - 48.6	4
5.6 - 6.9	48.6 - 60.0	5
6.9 - 8.2	60.0 - 71.2	6
8.2 - 9.4	71.2 - 80.6	7

Table 7.1 : Optimum number of modulator segments when segments are lossy and total length is limited.

Figure B2 illustrates how the normalized total phase contribution varies with αL, with the number of modulation segments N as a parameter. For clarity in the illustration, the curve for a particular value of N is plotted only when it is superior to the curve for (N-1). For large values of αL the performance improves as $\sqrt{N}$ until N approaches the optimum value.

B8. Optimum Lengths - Velocity Mismatch Case

In the case of phase-velocity mismatch there is an optimum length for each modulating segment. If the modulating segment is made too long its phase contribution begins to decrease. If each modulating segment is designed for this optimum length then the result derived in section 6 applies. However this is not quite the optimum use of the available power and length. The frequency response which results from phase-velocity mismatch will be discussed in section

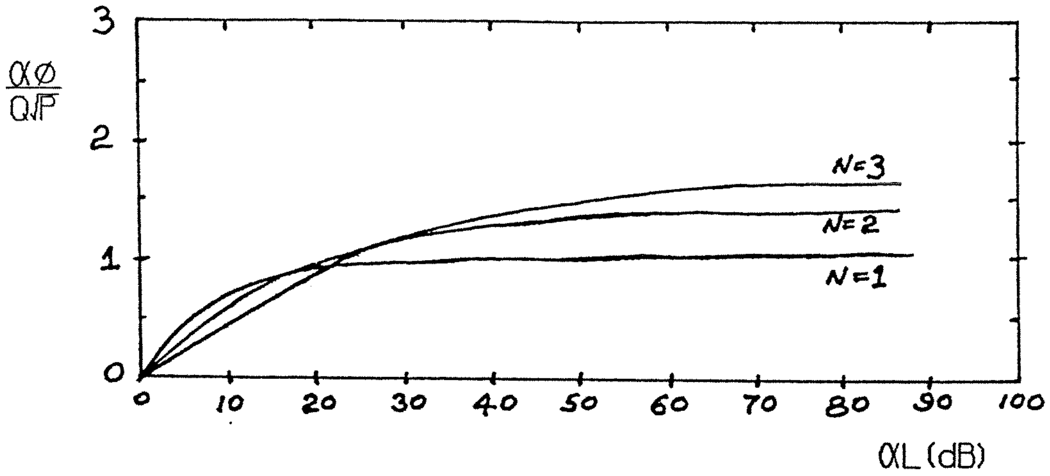

Figure B2

Normalized Phase Modulation as a Function of αL, with N as a Parameter. (Curve for each N is Plotted only when it is Greater than that for N-1, for Clarity.)

B9. It is:

$$R_N(f) = \frac{\sqrt{N}}{f} \sin\left(\frac{\pi f L (n_m - n_o)}{N c}\right). \tag{21}$$

The condition for the optimum number of modulator segments to be N is that

$$\frac{\sqrt{N-1}}{f} \sin\left(\frac{\pi f L (n_m - n_o)}{(N-1) c}\right) \leq \frac{\sqrt{N}}{f} \sin\left(\frac{\pi f L (n_m - n_o)}{N c}\right)$$

$$\leq \frac{\sqrt{N+1}}{f} \sin\left(\frac{\pi f L (n_m - n_o)}{(N+1) c}\right). \tag{22}$$

The optimum length for a single modulator segment occurs when

$$\sin\left(\frac{\pi f L (n_m - n_o)}{c}\right) \text{ is a maximum,} \tag{23}$$

i.e., when

$$L = \frac{c}{2 f (n_m - n_o)}, \tag{24}$$

that is,

$$\frac{\pi f L (n_m - n_o)}{c} = \frac{\pi}{2} = 1.5708 . \tag{25}$$

This is obtained by using N=1 in expression (22). If I define a normalized length $\mathcal{L}$,

$$\mathcal{L} = \frac{\pi f L (n_m - n_o)}{c}, \tag{26}$$

then I can make up a table showing the values of $\mathcal{L}$ at which the optimal number of segments changes.

$N \rightarrow (N+1)$	$\mathcal{L}$ (whole length)	$\mathcal{L}/N$(per segment)
$1 \rightarrow 2$	1.57	1.57
$2 \rightarrow 3$	2.83	1.41
$3 \rightarrow 4$	4.0	1.33
$4 \rightarrow 5$	5.20	1.30
$5 \rightarrow 6$	6.35	1.27
$10 \rightarrow 11$	12.23	1.22
$100 \rightarrow 101$	118	1.18
$1000 \rightarrow 1001$	1167	1.17

Table 8.1: Optimum Normalized Segment Lengths for a Phase-Velocity-Mismatched Modulator.

Table 8.1 shows that when a large number of these modulator segments is used the optimum length for each one is a little less than that for a single segment. This is because as the modulator segment approaches the single-segment optimum length the last part of its length is making a very small contribution to the phase. This length would be used more efficiently in a new modulator segment.

To give an example of the design procedure one might use, assume that the specification is for a minimum phase-shift of ϕ_{min} with a maximum available modulation signal power of P_{max} at a center-frequency f_o. As a first approximation to $\mathcal{L}/N$, one would choose $\mathcal{L}/N=1.57$. This would give the value of L_o used in the theory in section B6, viz. $L_o = \left(\mathcal{L}/N\right) c/\left(\pi\ f_o\ (n_m\text{-}n_o)\right)$. Given this information we can use the theory of section B6 to determine N, the number of segments of this length required to meet the sensitivity requirement. Having obtained a first estimate of N in this way, one can refer to Table 8.1 to find a better approximation to $\mathcal{L}/N$, which in turn is used to re-estimate L_o and N. This procedure should give a final result on the second iteration, or the third at most.

B9. Frequency Response Effects - Velocity Mismatch Result

Previously I stated that there might be an optimum modulator segment length. I gave the example of a modulator segment with phase-velocity mismatch. However, in this case the optimum length only applies at a single frequency. The optimum length would decrease with increasing frequency. Consequently when the modulator is constructed from a number of shorter segments its frequency response changes. Figure B3 shows the frequency responses of four modulators. In one case the whole interaction length is used in one modulator segment, driven with all the power. The frequency response of this modulator is proportional to

$$R(f) = \frac{1}{f} \sin\left(\frac{\pi\, f\, L\, (n_m - n_o)}{c} \right), \tag{27}$$

where n_m is the modulation refractive index,

n_o is the optical refractive index,

c is the velocity of light.

If the modulator is broken into N parts then the frequency response becomes

$$R_N(f) = \frac{\sqrt{N}}{f} \sin\left(\frac{\pi\, f\, L\, (n_m - n_o)}{N\, c} \right). \tag{28}$$

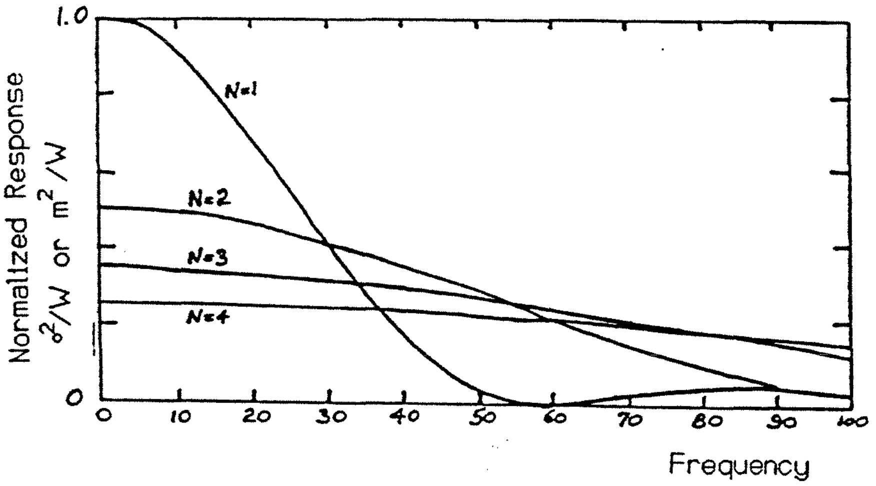

Figure B3

Frequency Response of a Velocity-Mismatch-Limited Modulator, whose (Arbitrarily Chosen) Length is Split into 1,2,3, or 4 Sections, Fed in Parallel

Figure B3 also includes plots of the response for N=2, N=3 and N=4.

B 10. Frequency Effects - Loss Limited Result

The loss-limited result showed how to determine how many modulator segments to use when the attenuation over the length of the transmission line was known. In general, however, the line attenuation is a function of frequency. Hence the result derived above is valid only at one particular frequency. Again, using a number of short modulator segments instead of a single, long modulator segment changes the frequency response. Since attenuation generally rises with frequency, at low frequencies the number of modulator segments will be too big, so that better performance would have been obtained with fewer segments. At high frequencies the number of segments will be too small, so that better performance would be obtained with more segments. Of course as attenuation rises the performance gets worse no matter how many segments are used. As an example, let me assume that the attenuation varies as

$$\alpha = \alpha_o(1 + \sqrt{\mathrm{f}/\mathrm{f}_c}) , \tag{29}$$

an expression which expresses simple conductor skin effect, and substitute this into expression (19) for total modulation. Figure B4 illustrates the result. As the number of modulation segments increases, the low-frequency responsivity decreases but the rolloff due to increasing attenuation at higher frequencies is slower.

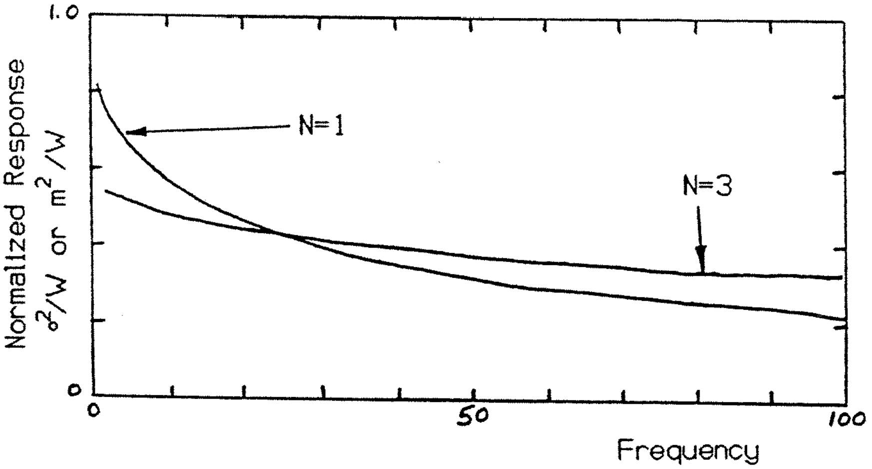

Figure B4

Frequency Response of a Loss-Limited Modulator, whose (Arbitrarily Chosen) Length is Driven as one Section, or Split into 3 Sections, Fed in Parallel

B 11. Other Configurations

The above analyses by no means exhaust the possible configurations which could be used. For example the problem of phase-velocity mismatch can be addressed by using a number of short modulator segments which are fed in series instead of in parallel. For example, Alferness et al. [1] have demonstrated a phase-reversal structure which ensures that the phase error resulting from phase-velocity mismatch never exceeds 90^o. A number of short modulator sections are connected together in series. Each section is long enough to produce a 180^o phase-drift of the modulation signal, and the sections are then connected together with crossovers to provide a 180^o phase-correction between sections. This limits the phase error to 90^o. Schaffner [2] has demonstrated a related concept which also limits the maximum phase error at a center frequency. At the design center-frequency, an M-section modulator of this type acts like a single modulator segment with no phase-velocity mismatch. As M increases, the length of this single modulator increases, and the limit on M occurs when the modulation signal attenuation over this length becomes severe. Thus, at the center frequency, a modulator of this type acts like a loss-limited modulator. Essentially the entire modulator can now be seen as a single loss-limited super-modulator-segment, since it has no phase-velocity mismatch (at least over some frequency range). This being the case, it may be optimal to use more than one of these super-modulator-segments, driven in parallel. The limits on what is possible tend to depend on the details of the splitting and phasing of the modulation signal, factors which are not considered here.

B 12. Conclusion

Traveling wave modulators suffer from phase-velocity mismatch and transmission-line attenuation. Where high modulation sensitivity is required at a specific frequency, it may be optimal to split the modulator into a number of shorter segments, each driven with a fraction of the available modulation signal power. I have shown how to determine the optimum configuration in the case of a modulator which suffers from neither problem, in the case of a modulator whose segment lengths are fixed by some constraint, in the case of a lossy modulator and in the case of a phase-velocity-mismatched modulator. In addition I have examined the bandwidth implications of the various approaches.

Appendix C

Fabrication of the Electro-Optic Modulators

C1. Introduction

The electro-optic modulators described in this thesis were fabricated at Hughes Research Laboratories. The electrode patterns for the modulators were designed at Caltech to match available Hughes optical waveguide masks. Electrode masks generated from these designs by a commercial mask-maker were then sent to James H. Schaffner at Hughes, where the rest of the fabrication work was done. Dr. Schaffner has provided details of the fabrication procedure outlined below.

C2. Optical Waveguide Fabrication

The $LiNbO_3$ substrate was cleaned completely before beginning waveguide fabrication to remove oil, dirt and other contamination. A photoresist (AZ 1370) was spun onto the substrate and again checked for contamination. A dark-field contact mask which would define the optical waveguides was aligned with the desired optical axis (the crystal y-axis usually) and brought into contact with the photoresist-covered surface of the substrate. The width of the stripe in the mask which defined the waveguide was 6-8 μm for 1.3 μm light, 4 μm for 0.633 μm light. The photoresist was then exposed for 6 seconds at 20 mW/cm^2 - other lamp output powers required different exposure times, of course. The Hughes personnel checked the exposure times with dummy pieces from time to time. The substrate was then developed and rinsed thoroughly.

Once the optical waveguides had been defined in the photoresist, the whole surface of the substrate was covered in 750 Å of titanium by an E-beam deposition system. This was followed by a lift-off process which removed the Ti from all of the substrate except where the optical waveguides had been defined. The substrate was then placed in a furnace which had a flowing O_2 environment. Extra pieces of $LiNbO_3$ were positioned near the O_2 input. For x-cut $LiNbO_3$ the temperature was taken from room temperature to 1000° C over a period of 3 hours, then left at 1000° C for 10 hours before being cooled gradually to room temperature over another 3 hours. In the case of z-cut material the warm-up and cool-down times were the same, but the temperature was kept steady at 1000° C for only 7.5 hours. The high temperature caused the Ti to diffuse into the $LiNbO_3$, producing the optical waveguide. After this procedure the substrate was inspected for black spots, which would indicate that the Ti had not fully diffused into the substrate.

C3. Mask Design and Production

The electrode masks were designed at Caltech and manufactured by Align-Rite Corp. The mask design began with information from James Schaffner about the dimensions of the optical waveguides available at Hughes Research Labs. He was able to provide the mask design information in .DXF format, which is produced by AutoCAD^R. We were using EasyCAD^R software, which could not read this format, but had a utility program which converted the file to EasyCAD^R's .FCD format. It was then possible to design the mask, using EasyCAD^R, as a separate layer overlaid on the optical waveguide mask. Once this had been done the waveguide mask layer was deleted from the design file. Since EasyCAD^R stored the design file in .FCD format, we again used the utility to convert the file to AutoCAD^R's .DXF format. We sent a disk with the .DXF file on it to Dr. Schaffner, who had a second utility which could convert from the .DXF format to a Calma format, which was then stored on a computer tape rather than a disk. Dr. Schaffner then sent the tape to Align-Rite Corporation, which made a final format conversion to MEBES format in order to produce the mask. It seems almost miraculous that a file could survive this many conversions without error, but there was never a problem with any of our designs. Once the mask had been made it was sent to Hughes Research Labs. for the electrode fabrication.

C4. Buffer Layer and Electrode Deposition

Once the optical waveguides had been fabricated, the next step was to deposit a SiO_2 buffer layer. This ensured that the optical fields would be well-separated from the metal electrodes, as the electrodes would cause unacceptable optical losses. The SiO_2 thickness was 1500 Å. After this layer had been deposited it was annealed for 1 hour at 400° C in an O_2 environment, taking 1 additional hour to reach that temperature and another 3 hours to cool off afterwards.

Next a layer of photoresist was again spun onto the substrate. The (dark-field) electrode mask was aligned with the optical waveguides on the substrate, and the photoresist again exposed and developed. A layer of Ti, 300 Å thick, was evaporated onto the substrate, followed by 2 μm of Au. A liftoff process then removed all of the Ti/Au except where the electrodes had been defined by the mask. This completed the fabrication of the electrodes.

C5. Polishing the Substrate

The final step in preparing the modulator was to polish the ends of the substrate so that the ends of the optical waveguides would be as smooth as possible. This is not an easy thing to do, because the optical waveguides lie just beneath the surface of the substrate. While it is easy to polish most of the endface, it is difficult to avoid chipping at the edge (Figure C1). In order to overcome this, additional pieces of $LiNbO_3$ were placed over the ends of the modulator and glued in place under pressure (Figure C2). The idea behind this procedure was to "bury" the optical waveguide in $LiNbO_3$ so that it would be in the middle of the endface during polishing, rather than near the edge, and so the end of the optical waveguide could be polished to a very smooth finish. This worked to some extent, although not perfectly, as it is difficult to get the pieces of $LiNbO_3$ sufficiently close together to prevent chip-formation.

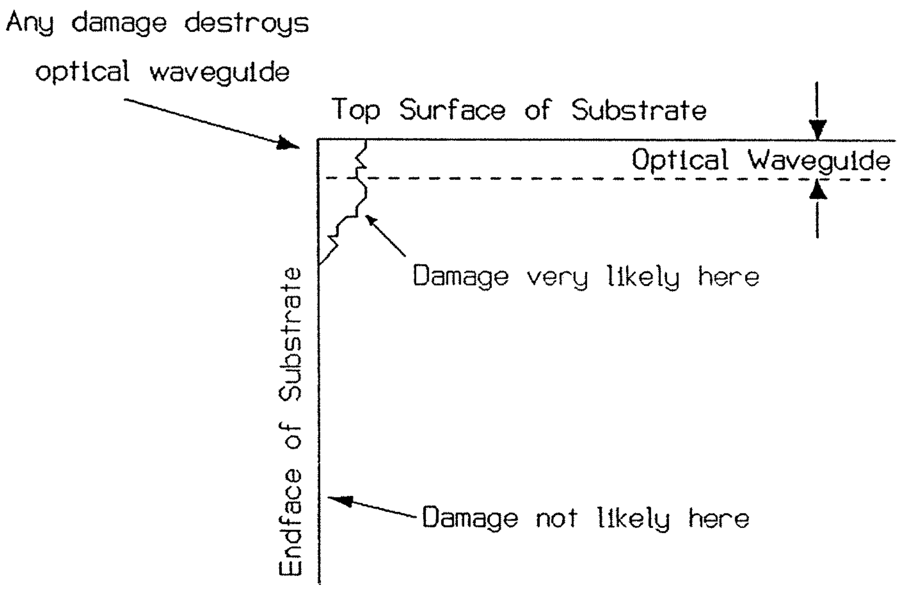

Figure C1 Effect of Substrate Chipping During Polishing

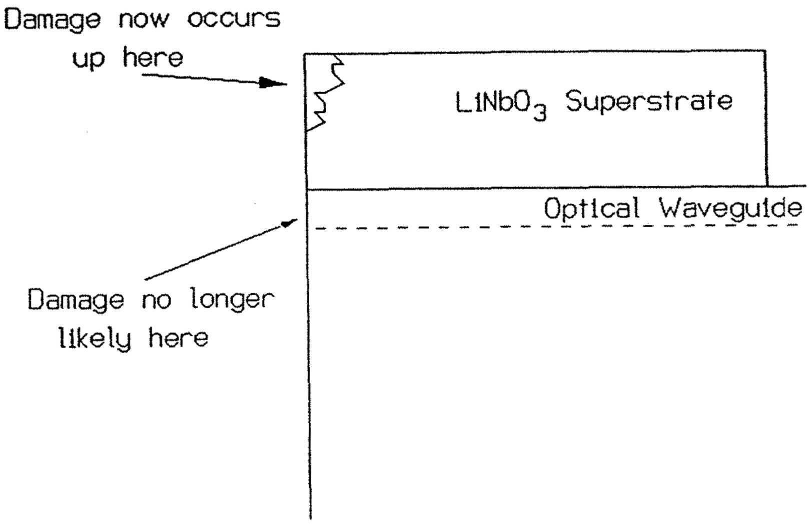

Figure C2 Method Used to Prevent Chipping During Polishing

Appendix D

Frequency Content of Mixed Phase-Amplitude Modulation

D1. Introduction

When measuring the performance of our electro-optic modulators we used a scanning Fabry-Perot Interferometer to find the optical sideband amplitude produced by the modulation. From this we worked back to calculate the amount of modulation produced. Of course, this requires knowledge of how the optical sideband amplitude is related to the modulation. We are ultimately interested in the amplitude modulation of the output of a photodiode detector, which is sensitive to amplitude modulation but not phase modulation of the optical signal. However, depending on the bias-point, the modulation produced may be mixed amplitude and phase modulation. We need to know what kind of sideband amplitude to expect when both phase and amplitude modulation are present, and how these affect the electrical output of the detector.

D2. Optical Transfer Function of the Modulator

The modulator can be characterized by its optical transfer-function. This is simply its S-parameter for the transfer of optical power from the optical input port to the optical output port. This S-parameter is a complex quantity, and is a function of the control voltage (signal voltage plus bias voltage).

The effect of the S-parameter is that if $S=Ae^{j\phi}$, then the modulator converts an optical input E_o $\mathrm{Cos}(\omega_o t)$ into an optical output E_oA $\mathrm{Cos}(\omega_o t + \phi)$.

D3. Frequency-Content Analysis for Mixed Modulation

I define:

$$\mathrm{A(V)} = |\ \mathrm{S(V)}\ | \ , \tag{1}$$

$$\phi(\mathrm{V}) = \angle\ \mathrm{S(V)} \ , \tag{2}$$

then perform a Taylor expansion about the point $\mathrm{V}=\mathrm{V}_o$ to only two terms (i.e., a small-signal Taylor expansion):

$$\mathrm{A}(\mathrm{V}_o + \Delta\mathrm{V}) = \mathrm{A}(\mathrm{V}_o) + \Delta\mathrm{V}\ \frac{\mathrm{dA(V)}}{\mathrm{dV}}\Big|_{\mathrm{V}\,=\,\mathrm{V}_o} , \tag{3}$$

representing small-signal amplitude modulation

$$\phi(\mathrm{V}_o + \Delta\mathrm{V}) = \phi(\mathrm{V}_o) + \Delta\mathrm{V}\ \frac{\mathrm{d}\phi(\mathrm{V})}{\mathrm{dV}}\Big|_{\mathrm{V}\,=\,\mathrm{V}_o} , \tag{4}$$

representing small-signal phase modulation. Now define the modulating signal as follows:

$$\Delta\mathrm{V} = \mathrm{V}_s\ \mathrm{Cos}(\omega_m \mathrm{t}) \ , \tag{5}$$

and define the following quantities:

$$\mathrm{m}_a = \mathrm{V}_s\ \frac{\mathrm{dA(V)}}{\mathrm{dV}}\Big|_{\mathrm{V}\,=\,\mathrm{V}_o} , \tag{6}$$

$$\mathrm{m}_p = \mathrm{V}_s\ \frac{\mathrm{d}\phi(\mathrm{V})}{\mathrm{dV}}\Big|_{\mathrm{V}=\mathrm{V}_o} , \tag{7}$$

$$A = A(V_o) \,, \tag{8}$$

$$\phi = \phi(V_o) \,. \tag{9}$$

Using equations (1) - (9) we find that an input

$$E_{in} = E_o \,\mathrm{Cos}(\omega_o t + \phi_o) \,, \tag{10}$$

where we choose ϕ_o = -ϕ without loss of generality, is converted to an output

$$E_{out} = E_o(A + m_a \,\mathrm{Cos}\, \omega_m t\,)\, \mathrm{Cos}(\, \omega_o t + m_p \,\mathrm{Cos}\, \omega_m t\,) \,. \tag{11}$$

I will expand Cos(ω_ot + m_p Cos ω_mt) at this point:

$$\mathrm{Cos}(\, \omega_o t + m_p \,\mathrm{Cos}\, \omega_m t\,) = \mathrm{Cos}\, \omega_o t \,\mathrm{Cos}(m_p \mathrm{Cos}\, \omega_m t) - \mathrm{Sin}\, \omega_o t \,\mathrm{Sin}(m_p \mathrm{Cos}\, \omega_m t) \tag{11a}$$

Since we are using small-signal Taylor expansions, they are only valid if m_a and m_p are $\ll 1$, so expand this in first-order terms only:

$$= \mathrm{Cos}\, \omega_o t - m_p \mathrm{Cos}\, \omega_m t \,\mathrm{Sin}\, \omega_o t \,, \tag{11b}$$

$$= \mathrm{Cos}\, \omega_o t - \frac{m_p}{2}\Big(\mathrm{Sin}(\omega_o - \omega_m)t + \mathrm{Sin}(\omega_o + \omega_m)t \Big) . \tag{11c}$$

Thus:

$$\frac{\mathrm{E}_{out}}{\mathrm{E}_o} = \mathrm{A}\ \mathrm{Cos}\ \omega_o \mathrm{t} - \frac{\mathrm{A}\ \mathrm{m}_p}{2}\Big(\mathrm{Sin}(\omega_o - \omega_m)\mathrm{t} + \mathrm{Sin}(\omega_o + \omega_m)\mathrm{t} \Big)$$

$$+ \mathrm{m}_a\ \mathrm{Cos}\ \omega_m \mathrm{t}\ \mathrm{Cos}\ \omega_o \mathrm{t} - \frac{\mathrm{m}_a \mathrm{m}_p}{2}\ \mathrm{Cos}\ \omega_m \mathrm{t} \Big(\mathrm{Sin}(\omega_o - \omega_m)\mathrm{t} + \mathrm{Sin}(\omega_o + \omega_m)\mathrm{t} \Big). \tag{12}$$

Again, m_a and m_p are both very small, so their product will be neglected.

$$\frac{\mathrm{E}_{out}}{\mathrm{E}_o} = \mathrm{A} \Big(\mathrm{Cos}\ \omega_o \mathrm{t} - \frac{\mathrm{m}_p}{2}\ \mathrm{Sin}(\omega_o - \omega_m)\mathrm{t} - \frac{\mathrm{m}_p}{2}\ \mathrm{Sin}(\omega_o + \omega_m)\mathrm{t} \Big)$$

$$+ \frac{\mathrm{m}_a}{2}\ \mathrm{Cos}(\omega_o - \omega_m)\mathrm{t} + \frac{\mathrm{m}_a}{2}\ \mathrm{Cos}(\omega_o + \omega_m)\mathrm{t}\ . \tag{13}$$

Hence we have the result:

$$\text{Normalized Power at } \omega_o = \mathrm{A}^2\ , \tag{14}$$

$$\text{Normalized Power at } \omega_o - \omega_m = \left(\frac{\mathrm{A}\ \mathrm{m}_p}{2}\right)^2 + \left(\frac{\mathrm{m}_a}{2}\right)^2, \tag{15}$$

$$\text{Normalized Power at } \omega_o + \omega_m = \left(\frac{\mathrm{A}\ \mathrm{m}_p}{2}\right)^2 + \left(\frac{\mathrm{m}_a}{2}\right)^2, \tag{16}$$

where we recall that

$$\mathrm{A} = |\ \mathrm{S}(\mathrm{V}_o)\ |\ ,$$

$$\mathrm{m}_a = \mathrm{V}_s \frac{\mathrm{d}|\ \mathrm{S}(\mathrm{V})\ |}{\mathrm{dV}}\Big|_{\mathrm{V}=\mathrm{V}_o}\ ,$$

$$\mathrm{m}_p = \mathrm{V}_s \frac{\mathrm{d}\angle\ \mathrm{S}(\mathrm{V})}{\mathrm{dV}}\Big|_{\mathrm{V}=\mathrm{V}_o}\ .$$

D4. Analysis Performed for a Mach-Zehnder Amplitude Modulator

A Mach-Zehnder amplitude modulator splits the beam into two paths, phase modulates the paths separately, then recombines the beams. In general the amount of phase modulation in the two paths may not be equal, so that the output is of the form:

$$E_{out} = \frac{1}{2}\Big(\mathrm{Cos}(\omega_o t - PV) + \mathrm{Cos}(\omega_o t + QV)\Big)\,, \tag{17}$$

where P and Q relate the phase modulation in each path to the applied voltage. Adding these two terms together we get:

$$\mid S(V) \mid = \sqrt{\frac{1 + \mathrm{Cos}\big((P + Q)V\big)}{2}}\;, \tag{18}$$

$$\angle\, S(V) = -\tan^{-1}\left(\frac{\mathrm{Sin}\ PV - \mathrm{Sin}\ QV}{\mathrm{Cos}\ PV + \mathrm{Cos}\ QV}\right), \tag{19}$$

where the expressions are valid only over the range

$$-\pi \;\leq\; (P+Q)V \;\leq\; \pi\;. \tag{20}$$

D4.1 Balanced Mach-Zehnder Amplitude Modulator

In a balanced Mach-Zehnder, P=Q. Then

$$\mid S(V) \mid = \mathrm{Cos}\ PV\;, \tag{21}$$

and

$$\angle\, S(V) = 0\;. \tag{22}$$

Then we have

$$A = \mathrm{Cos}\ PV_o\ , \tag{23}$$

$$m_a = -PV_s\ \mathrm{Sin}\ PV_o\ , \tag{24}$$

$$m_p = 0\ , \tag{25}$$

i.e., the modulation is purely amplitude modulation; there is no phase modulation.

$$\text{Normalized Carrier Power} = \mathrm{Cos}^2\ PV_o\ , \tag{26}$$

$$\text{Normalized Sideband Power} = \left(\frac{P\ V_s}{2}\right)^2 \mathrm{Sin}^2\ PV_o\ , \tag{27}$$

$$\text{Sideband/Carrier Ratio} = \left(\frac{P\ V_s}{2}\ \mathrm{Tan}\ PV_o\right)^2 . \tag{28}$$

Note that one has to be very careful when looking at these results. The modulator would be used in a system where the output comes from a photodiode, or other power-detector. These are essentially square-law devices. The frequency component at ω_m at the detector output comes from the multiplication of the optical components at ω_o and $\omega_o \pm \omega_m$ in the squaring process in the detector. Hence when the optical sideband/carrier ratio is a maximum (actually, infinite) the resulting electrical output has no frequency components at ω_m.

We can go ahead and compute the output in the electrical domain by taking equation (13) and squaring it, discarding any terms in m_a^2, m_p^2 or $m_a m_p$, then retaining only the remaining terms which involve DC or ω_m , to get

$$\text{Normalized output Voltage} = \frac{A^2}{2} + A m_a \operatorname{Cos} \omega_m t \ , \tag{29}$$

i.e.,

$$V_{out} = \frac{A^2}{2}\left(1 + \frac{2\ m_a}{A} \operatorname{Cos} \omega_m t\right) , \tag{30}$$

which gives the electrical modulation index m as

$$m = \frac{2\ m_a}{A} \ , \tag{31}$$

while the electrical power at ω_m is given by

$$\text{Normalized Power} = (A m_a)^2 \ , \tag{32}$$

and, substituting for m_a and A for the balanced Mach-Zehnder,

$$\text{Normalized Power} = \frac{1}{4}\ (PV_s \operatorname{Sin} 2PV_o)^2 \ . \tag{33}$$

The maximum power is delivered when $PV_o = \pi/4$, at which point the optical S/C ratio turns out to be

$$(S/C)_{operating\ point} = \left(\frac{PV_s}{2}\right)^2 , \tag{34}$$

while the modulation index m is then

$$m = 2\ PV_s\ . \tag{35}$$

Note that the quantity $\frac{\pi}{2P}$ is often specified for Mach-Zehnder modulators, when it is known as V_π.

D4.2 Single-Sided Mach-Zehnder Amplitude Modulator

In this case, Q=0. Then

$$\mid S(V) \mid = \text{Cos}\ \frac{PV}{2}\ , \tag{36}$$

$$\angle\ S(V) = -\ \tan^{-1}\ \frac{\text{Sin PV}}{\text{Cos PV} + 1}\ , \tag{37}$$

where now the expression for $\angle$ S(V) looks unpleasant. It isn't, in fact. A right triangle whose opposite side has length Sin PV and whose adjacent side has length Cos PV + 1 has hypotenuse $\sqrt{2 + 2\ \text{Cos PV}}$. The angle specified by these three lengths has a cosine equal to $\frac{1}{\sqrt{2}}\sqrt{1 + \text{Cos PV}} = \text{Cos}\ \frac{PV}{2}$. Hence we can simplify (37) as:

$$\angle\ S(V) = \frac{-\ PV}{2}\ , \tag{37a}$$

again valid only for $-\pi \leq PV \leq \pi$. Then we have

$$A = \text{Cos}\ \frac{PV_o}{2}\ , \tag{38}$$

$$m_a = -\ \frac{PV_s}{2}\ \text{Sin}\ \frac{PV_o}{2}\ , \tag{39}$$

$$\mathrm{m}_p = \frac{-\,\mathrm{PV}_s}{2}\,. \tag{40}$$

These give the results:

$$\text{Normalized Carrier Power} = \mathrm{Cos}^2\,\frac{\mathrm{PV}_o}{2}\,, \tag{41}$$

$$\begin{aligned}\text{Normalized Sideband Power} &= \left(\frac{\mathrm{PV}_s}{4}\right)^2\left(\mathrm{Cos}^2\,\frac{\mathrm{PV}_o}{2} + \mathrm{Sin}^2\,\frac{\mathrm{PV}_o}{2}\right),\\ &= \left(\frac{\mathrm{PV}_s}{4}\right)^2. \end{aligned} \tag{42}$$

This is an interesting result. The sideband power is independent of the bias-point V_o. This makes the single-sided modulator rather more convenient when trying to measure performance with a Fabry-Perot interferometer. However, in spite of initial appearances it is not the most attractive option for optical frequency-shifting by optical sideband generation, even though there is no need to worry about the bias-point. This is because a phase-modulator would be four times more efficient at converting optical power to the sidebands, and its sidebands are also bias-point independent.

We can again ask what happens at the electrical output of a detector in a normal application. We find that the appropriate procedure is to square (13) exactly as before, leading to exactly the same results as (30) - (32). Note that m_p does not appear in (30), which is appropriate because the detector is insensitive to phase modulation. We can again compute the electrical output power at frequency ω_m :

$$\text{Normalized Power} = \frac{1}{16}(\mathrm{PV}_s \ \mathrm{Sin}\ \mathrm{PV}_o)^2 \ . \tag{43}$$

The maximum value of this occurs at $\mathrm{PV}_o = \pi/2$, which shows that for this modulator $\mathrm{V}_\pi = \pi/\mathrm{P}$. At this maximum point, the operating point, the optical S/C is given by:

$$(\mathrm{S/C})_{operating\ point} = \frac{1}{8}\ (\ \mathrm{PV}_s)^2 \ . \tag{44}$$

When making measurements with a Fabry-Perot interferometer we can set the bias so that the optical S/C has its minimum value. This occurs when the bias maximizes the optical carrier power. At its maximum, this power-level (and hence the S/C) is not sensitive to the bias, so small bias-point errors are acceptable. That would not be true at the bias-point which would be used in actual operation of the modulator with a photodiode. We find

$$(\mathrm{S/C})_{min} = \left(\frac{\mathrm{PV}_s}{4}\right)^2 . \tag{45}$$

From (31), (38) and (39) we have

$$\mathrm{m}_{operating\ point} = \mathrm{PV}_s \ , \tag{46}$$

and so from (45) we get the result

$$\mathrm{m}_{operating\ point} = 4\sqrt{(\mathrm{S/C})_{min}} \ . \tag{47}$$

D5. Analysis of a $\Delta\beta$ Coupler-Modulator

The $\Delta\beta$ coupler-modulator has two output ports instead of one, and the transfer-functions between the input port and these output ports are different. In fact, the S-parameters for such a modulator are:

$$S_{21}(V) = \mathrm{Cos}\left(\theta\sqrt{1+3\,V^2}\,\right) + j\sqrt{3}\,\frac{V}{\sqrt{1+3\,V^2}}\,\mathrm{Sin}\left(\theta\sqrt{1+3\,V^2}\,\right), \tag{48}$$

$$S_{31}(V) = -j\,\frac{\mathrm{Sin}\left(\theta\sqrt{1+3\,V^2}\,\right)}{\sqrt{1+3\,V^2}}\,. \tag{49}$$

Where $\theta=\kappa L$, and V is normalized so that for $\kappa L=\pi/2$, the switching voltage is V=1. Then, taking S_{21} (for the Through arm) first,

$$|\,S_{21}(V)\,| = \sqrt{1 - \frac{\mathrm{Sin}^2\left(\theta\sqrt{1+3\,V^2}\,\right)}{1+3\,V^2}}\;, \tag{50}$$

$$\angle\, S_{21}(V) = \mathrm{Tan}^{-1}\left\{\frac{\sqrt{3}\,V}{\sqrt{1+3\,V^2}}\,\mathrm{Tan}\left(\,\theta\sqrt{1+3\,V^2}\,\right)\right\}. \tag{51}$$

It is a straightforward matter to write out m_a and m_p, and hence find the power in the carrier and sidebands, but the expressions are complicated and not very informative. Unlike the Mach-Zehnder, there is no simple separation of phase and amplitude modulation. In general when the amplitude modulation is non-zero, there is phase-modulation at the same time. However there may be non-zero phase modulation when the amplitude modulation is zero.

If we now take the expression for S_{31} (for the Cross arm), we have

$$| \mathrm{S}_{31}(\mathrm{V})| = \frac{\mathrm{Sin}\left(\theta\sqrt{1+3\,\mathrm{V}^2}\right)}{\sqrt{1+3\,\mathrm{V}^2}}\,, \tag{52}$$

$$\angle\,\mathrm{S}_{31}(\mathrm{V}) = 0\,. \tag{53}$$

There is no phase-modulation of the Cross-arm output at all! The value of m_a is the same as for the Through arm, so the amplitude of the sidebands present in the output of the Through arm will be greater than or equal to the amplitude of the sidebands present in the output of the Cross arm at all times.

Appendix E

Analysis of the Linearized Modulators

E1. Introduction

In the course of studying the issue of linearizing the $\Delta\beta$ electro-optic modulator, I needed some way to specify linearity. As a first approximation I computed the derivatives of the candidate transfer-functions numerically and tried to set the derivatives to zero simultaneously by adjusting the free parameters. However, systems engineers do not usually use specifications on the derivatives. A common way to specify linearity is to state the dynamic range of a system. Since Dr. Bridges was interested in this issue also, he developed software which analyses an optical link using an external modulator and computes the two-tone dynamic range of the link (defined below). By inserting the transfer-function of the modulator under consideration into this software it was possible to compare the performance of the various modulators.

E2. Two-Tone Dynamic Range

The two-tone dynamic range of a link is defined for a link which has two input signals (two tones) with the same amplitude but different frequencies, and is defined as the ratio of two powers. The first (lower) power is the input signal power (for each tone) at which each output tone power becomes equal to the system noise level. The second (higher) power is the lowest input signal power at which there is a spurious output signal at the system noise level. The ratio of the higher power to the lower is the two-tone dynamic range. The reason for using two tones (f_1 and f_2) is that the third-order nonlinearity in the link will produce tones at $2f_1 \pm f_2$ and at $2f_2 \pm f_1$, and the two difference frequencies (i.e., $2f_1 - f_2$ and $2f_2 - f_1$) lie near the original frequencies so that they may be impossible to filter out even if the link bandwidth is narrow. It is possible to define a narrowband dynamic range which takes this third-order intermodulation (actually odd-order intermodulation in general) into account but ignores even-order products because the even-order products can be filtered out in a narrowband system. We have not used this modified definition of dynamic range, however.

E3. Computation of Dynamic Range

The computation is based on finding the output signal amplitudes from the link at the frequencies of interest when there is a two-tone input, and determining when these are equal to the noise-level.

The output signal is the product of the modulator transfer function and the link gain (assumed linear). The link gain is given by

$$G_\ell = P_L \, L_M \, L_F \, \eta_D \, , \tag{1}$$

where

P_L is the laser power,
L_M is the modulator optical loss,
L_F is the fiber & connector loss,
η_D is the detector responsivity.

The input power to the modulator is related to modulator drive voltage by the modulator impedance:

$$V_s = \sqrt{2\ Z_M\ P_s}\ , \tag{2}$$

where Z_M is the modulator input resistance,

P_s is the signal power per tone.

The input signal is then $V_s\left(\cos(2\ \pi\ f_1) + \cos(2\ \pi\ f_2)\right)$, and the modulator transfer-function operates on this to produce an output function $F(t,P_s)$. This output function, multiplied by the link gain, produces the output signal current $I(t,P_s)$. This has a DC (bias) value due to the DC bias-voltage applied to the modulator, and the DC value of $I(t, P_s)$ is denoted I_{DC}. The RF component of $I(t, P_s)$ is then denoted $I_{RF}(t, P_s)$, where

$$I_{RF}(t, P_s) = I(t, P_s)\ -\ I_{DC}\ . \tag{3}$$

The signal component at f_1 can be extracted by performing a one-tone Fourier transform (i.e., the Fourier transform where the frequency is specifically entered as a value in the transform kernel). Hence, the signal component at f_1 in the output current is found as

$$S_{f_1}(P_s) = \frac{2}{T} \int_0^T I_{RF}(t,P_s)\ e^{j\ 2\ \pi\ f_1 t}\ dt\ , \tag{4}$$

where the period of integration, T, is chosen as

$$T = \frac{1}{|\ f_2\ -\ f_1|}\ , \tag{5}$$

which, in turn, requires that f_2/f_1 should be rational.

Of course, the output component at the other input frequency, f_2 , should be the same. In the same way, one can compute the output component at every other frequency of interest. In this case, the other frequencies of interest are the harmonic product $2f_1$ and the intermodulation product $2f_1 - f_2$. These can be found by substituting the appropriate frequency in place of f_1 in equation (4).

One caveat is necessary about the choice of frequencies f_1 and f_2 . They will, in general, produce output frequencies at $m\ f_1 + n\ f_2$, where m and n are integers which may be positive or negative. Some of these frequencies will coincide. For example, if f_1=1.0 and f_2=1.4 are chosen, then

$$10\ f_1 - 6\ f_2 = 1.6 = 3\ f_1 - f_2\ . \tag{6}$$

This is true only because of the specific example chosen, and so cannot be considered a "real" intermodulation product. It is desireable to avoid this kind of problem by choosing f_1 and f_2 so that only large values of m and n produce this kind of overlap.

We do not have enough information yet to compute the dynamic range, because we need to know the noise-level. The total noise in the receiver diode is

$$N_{tot} = N_T + N_L + N_S + kT\ , \tag{7}$$

where
$$N_T = G_{s/s}\, kT \tag{8}$$

gives the thermal noise from the link input, and $G_{s/s}$ is the small-signal gain computed from the output signal power at very low input power levels;

$$N_L = (\mathrm{RIN})\, I_{DC}{}^2\, R_D \tag{9}$$

gives the noise due to the laser, where (RIN) is the laser residual intensity noise, I_{DC} is the detector DC current (as determined earlier), and R_D is the load resistance connected across the detector; and

$$N_S = 2\, e\, I_{DC}\, R_D \tag{10}$$

gives the shot-noise.

To compute the dynamic range, the output signal components must be converted to power, so that they can be compared to the noise power. For example, the signal power at f_1 is computed as

$$P_{f_1}(P_s) = \left(S_{f_1}(P_s)\right)^2 R_D/2\ , \tag{11}$$

and so on for the other frequency components. The dynamic range is then determined by finding three power-levels, P_{s_1}, P_{s_e} and P_{s_o}. These are defined implicitly by the following three equations:

$$P_{s_1} :\ P_{f_1}(P_{s_1}) = N_{tot}\ , \tag{12}$$

$$P_{s_e} : P_{2\,f_1}(P_{s_e}) = N_{tot} , \tag{13}$$

$$P_{s_o} : \; P_{2\,f_1 - f_2}(P_{s_o}) = N_{tot} . \tag{14}$$

The dynamic range is now defined as

$$R_{DYN} = \min[\, (P_{s_o}/P_{s_1}) \, , \, (P_{s_e}/P_{s_1})] \, . \tag{15}$$

E4. Conclusion

The plots in Chapter 7 were generated by a MathCAD^R program which performed the computations shown above. I modified Dr. Bridges' version for the chapter, but only in order to use a different method of generating the modulator transfer-function. The computation of the dynamic range used the same procedure.